Composition-Structure-Property Relationship in Cs-based Halide Perovskites using Electronic Structure Calculations

A Thesis
Presented in Partial Fulfillment of the Requirements for the
Degree of Master of Science
with a
Major in Materials Science and Engineering
in the
College of Graduate Studies
University of Idaho
by
Anirban Naskar

Major Professor: Samrat Choudhury, Ph.D.
Committee Members: Krishnan Raja, Ph.D.; Indrajit Charit, Ph.D.
Department Administrator: Eric Aston, Ph.D.

August 2019

Authorization to Submit Thesis

This thesis of Anirban Naskar, submitted for the degree of Master of Science with a Major in Material Science and Engineering and titled "Composition-Structure-Property Relationship in Cs-based Halide Perovskites using Electronic Structure Calculations" has been reviewed in final form. Permission, as indicated by the signatures and dates below, is now granted to submit final copies to the College of Graduate Studies for approval.

Major Professor: ____ Date: ____________
Samrat Choudhury, Ph.D.

Committee Members: ____ Date: ____________
Krishnan Raja, Ph.D.

____ Date: ____________
Indrajit Charit, Ph.D.

Department
Administrator: ____ Date: ____________
Eric Aston, Ph.D.

Abstract

The last three decades have witnessed significant progress in electronic materials due to the constant discovery of new materials for various applications. ABX_3 (A = Cs; B = Ca, Sr, Ba; X =I, Br, Cl, or F) *s*-block halide perovskites are widely considered as a scintillator material and a replacement of lead-based solar device due to their excellent electronic properties. The performance of the device is linked to the atomic and electronic structure of the halide perovskites. Using *ab-initio* calculations, we studied the effect of chemical composition, atomic structure on the electronic properties (bandgap) of *s*-block halide perovskite for both bulk and surfaces. We found that the bulk and the surface bandgaps of the perovskites are closely related to the intrinsic properties such as atomic or ionic size, electronegativity, bond-dissociation energy of B and X. The bandgap changes on the surfaces compare to the bulk are explained in terms of the structural changes such as bond-distance and bond-angle. Defects are produced inevitably during the synthesis of these compounds and largely depends on the synthesis condition. It has been reported that the point defects such as antisite defects are detrimental to carrier transport as they create localized electronic (deep trap) defects on the band gap. Using *ab-initio* calculations, we also investigated the impact of antisite defect, X_B on the electronic properties of ABX_3 (A = Cs; B = Ca, Sr, or Ba; X =I, Br, Cl, or F) bulk perovskites. Our results reveal that the formation of defect state in the band gap due antisite defect, X_B strongly depends on the composition and the crystal structure. We observed that, for a fixed composition of A and B the electronic defect forms at a higher energy level on the bandgap for bigger halogen atom compared to the halogen atom of smaller size. Further, the antisite defect creates localized states at two different locations in the band-gap for the orthorhombic structure. Whereas, for the same composition with the cubic crystal structure, the antisite defect creates a localized electronic state only at one location. Finally, we linked the location of these electronic defect states in the band gap to the intrinsic property of the constituent elements such as bond-dissociation energy and the atomic size, which can be a useful tool to understand and predict the position of localized electronic states produced by the point defects.

Acknowledgement

I would like to acknowledge my Advisor Prof. Samrat Choudhury for accepting me as his graduate student. I would also like to thank Dr. Rabi Khanal for teaching me the VASP software which I have used for my calculations. I am very grateful to Idaho National Lab (INL). The entire research was carried out using the computing resources at the High Performance Computing Center at the Idaho National Laboratory Additionally, I would like to acknowledge department of Chemical and Materials engineering for funding my graduate study, and all my committee members for their contribution towards the completion of master's degree in Material Science and Engineering.

Dedication

I would like to thank my parents (Aparna Naskar and Biswanath Naskar) and my wife Farheen Anjum for their support during my hard time. Additionally, I want to thank Dr. Rabi Khanal for motivating me during this time phase. Furthermore, I want to thank my brother Sourav Naskar and my friends Dr. Sayan Sarkar and Tariq Al. Tobi for helping me in all aspects of my life.

Table of Contents

List of Tables

List of Figures

Chapter 1: Introduction

1.1 Solar cell

The rapid growth of the world's population coupled with increasing consumption of non-renewable energy sources (fossil fuels) increases the demand for clean and renewable energy sources such as solar, wind, tidal, and geothermal energy. Out of all the renewable sources of energy, solar energy is most abundantly available and a better solution to other environmental concerns, namely global warming, greenhouse gases, etc. produced by fossil fuel. Starting from 1954 (discovery of first practical solar cell [1,2]) till present day an increasing and continuing efforts to produce electricity from the solar energy is observed. A solar cell absorbs the photons or solar energy and produces carriers (electrons or holes), and the collection of photo-generated carriers produce an electrical current. The performance of a solar cell is measured by the power conversion efficiency (PCE) and defined as the ratio of power output to the power absorbed-

$$PCE = \frac{P_{out}}{P_{in}} = \mathrm{FF}\ \frac{J_{SC}\ V_{OC}}{P_{in}}$$

FF is the fill factor; P is the incident solar power, J is the current density and the subscripts sc, and oc stands for short-circuit, and open circuit, respectively. The PCE of a solar cell directly depends on the intrinsic properties of the absorber materials (typically a semiconductor). One of the major determining property of absorber material is the bandgap which can be found from the band structure of the material. A typical band structure is consisting of the conduction band and the valance band. The energy difference between the valance band maximum (VBM) and the conduction band minimum (CBM) is known as the band gap. To produce electricity, the electrons must jump from VBM to CBM. A band gap is the most important property in determining the ability of the material to absorb the visible spectrum (wavelength of 380 to 740 nm [3]). The PCE of the solar cell and the bandgap of the absorbing material is closely connected by the Shockley-Queisser limit plot (Fig 1.1).

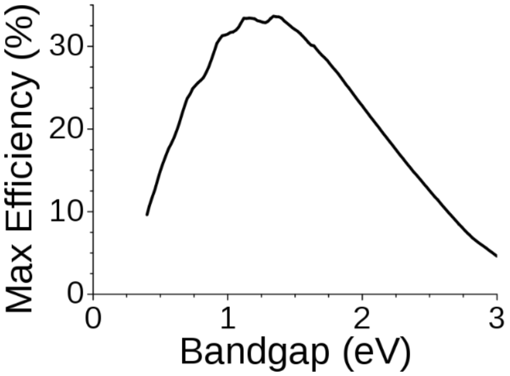

Figure 1.1 The Shockley-Queisser limit for the efficiency of a solar cell.[4]

It shows at the 1.1 eV bandgap the maximum theoretical PCE can be achieved is 30%. Usually, a bandgap in the range of 1.1-1.56 eV is most suitable for the solar cell application [5]. Again, the J_{sc}, FF and V_{oc} terms in the *PCE* is directly linked with the bandgap of a semiconductor material [6]. So, optimum *PCE* for a solar cell can be achieved by tuning the bandgap. Another important property of a suitable absorber material is mobility and the diffusion length of the photogenerated electrons or hole. As the charged carrier produced by the photon, it is important to transport them to the collectors without recombination. So, the high mobility and diffusion length of electron and holes are desired to produce more current. Other than these two, an absorber material should have a high defect tolerance. Defects are produced in the material during the synthesis. Doped atom, point defects (vacancy, interstitials, and antisite), grain boundary, etc. are the most commonly observed defects in the material. Defects produce an additional electronic state on the bandgap. Depending on the position of the electronic states, they can create a harmful effect. The states which are 0.02-0.03 eV higher than the VBM and lower than CBM considered as a shallow level defect and considered as harmless. But the defect states formed at the middle of the bandgap (trap) can act as an electron-hole recombination center. Recombination of electron and hole reduced overall PCE of the solar cell. So, a material with high defect tolerance is highly desired for the application of a solar cell. Overall, understanding the details of the band structure and band gap is critical in improving the performance of the solar cell. Based on the light absorbing materials, solar cells can be classified into three generations [7]. The first-generation solar cells are based on single and multi-crystalline silicon [8]. Although first-generation solar cells produce high efficiency, the production cost of these solar cells is very high. To make solar cells more cost-effective, the second-generation solar cells were developed based on materials such as copper indium galenium selenide (CIGS) and cadmium telluride (CdTe) [9]. Despite being more cost-effective, the second-generation solar cells lack in performance compared to the first-generation, which has further motivated researchers towards the development of the third-generation solar cell. The third-generation solar cell is mainly based on organic, inorganic halide-based perovskite materials. Halide-based perovskites own excellent electrical properties such as long diffusion length of the electron [10,11], high open-circuit voltage [12], high absorption coefficient [13], high defect tolerance [14], etc. and that makes it a perfect fit for the absorber material for the solar cell. The first halide-based perovskite $CH_3NH_3PbI_3$ (Methyl ammonium lead iodide or $MAPbI_3$) solar cell is fabricated in 2009 by Kojima et al. with a PCE of 3.8% [15]. Over the last decade, the efficiency of the halide-based perovskite solar increased from 3.8% to 23.7% due to the extensive research in this field [16]. The improved efficiency is obtained by improving the solar cell architecture [17,18], introducing new electron and hole transporting layer [19,20], eliminating the formation of trap state on the bandgap [21,22], tuning the band gap using mixed composition [23,24], etc. For example, the out of the top six power conversion efficiency certified by NREL, five of them are based on perovskite with a mixed composition ($FA_{0.85}MA_{0.15}PbI_{2.55}Br_{0.4}$) [11]. It is very clear that the composition or the chemistry of these individuals plays a decisive role in achieving a higher PCE. So, the understanding of the structure and the chemical interplay between the elements in halide-based perovskite is essential and discussed in the next section.

1.2 Halide-Perovskite structures:

Halide perovskite structures are generally characterized by the chemical formula ABX_3, where A is a monovalent cation, B is a divalent cation (usually a metal), and X is a monovalent anion [25,26]. For metal-halide based perovskite system, which is used widely as a solar cell application, the A cation (MA, or $CH_3NH_3^+$, FA, or $CH_3(NH_2)_2^+$ and Cs) is a relatively larger compared to the B or X. The B and X sites are occupied by a divalent metal (Pb^{2+}, Sn^{2+}, Ge^{2+}, Ca^{2+} or Sr^{2+}) and a halide (I^-, Br^- etc.). Figure 4 represents a typical halide perovskite structure ($MAPbI_3$), where B (Pb) with neighboring six halides (I) forms a $[BX_6]^{4-}$ octahedra and A (MA^+) cation sits in the void between two corner-sharing octahedra.

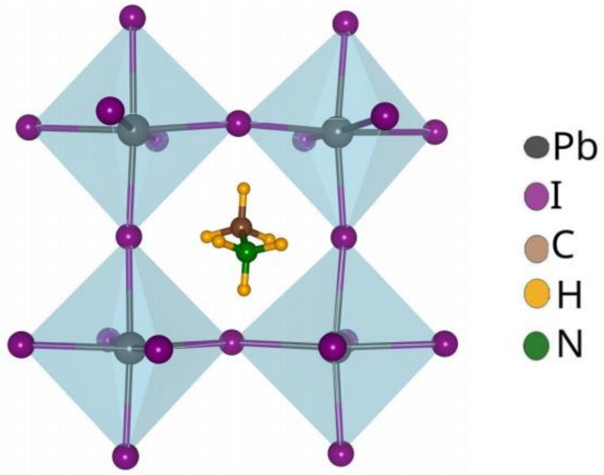

Figure 1.2. $MAPbI_3$ structure with the octahedral network as a representative of ABX_3 perovskite.

To form a perovskite structure, the tolerance factor should be in between 0.8 and 1.1[26-30]. At high temperature, the cubic phase of the perovskite structure is observed. With the decrease in temperature, the lower symmetry phases such as tetragonal, orthorhombic, monoclinic, etc. are formed. The reduced symmetry with a decrease in temperature is closely related to the octahedral tilting compared to the no tilt octahedra in ideal cubic structure [27]. Again, the structural change directly affects the electronic structure of a perovskite material and hence the optoelectronic properties. It is usually observed that the most symmetrical cubic phase shows the smallest bandgap and the superior conductivity compared to other low symmetry phases. For example, in $CsPbI_3$, the transition from the cubic phase to the orthorhombic phase at the temperature 634K increased the bandgap from 1.76 eV (cubic) to 2.78 eV (orthorhombic) [31,32]. The lower symmetry phase has different bond-distances and bond-angles between the metal and halide which affect the position of the VBM and CBM and hence different bandgaps are observed in different phases.

As mentioned earlier that due to outstanding electrical properties the halide-based perovskites are widely used in a solar cell. Apart from its photovoltaic application, the halide perovskite materials are considered for a broad range of electronic material applications such as light-emitting diodes (LEDs) [33,34], lasers [35], gas sensors [36], Li-ion batteries [37], etc. The excellent properties of perovskite compounds are closely connected with their band structure. The VBM and CBM in halide perovskites are formed due to the overlap between the bonding or antibonding orbitals of the constituent atoms. So, for ABX_3 type perovskite, the nature of VBM and CBM will change for different chemistry of A, B or X. Based on the B metal composition we can classify the perovskites as p-block perovskites (B= Pb, Sn or Ge) and *s*-block perovskites (B= Ca, Sr or Ba). The *p*-block perovskites are polar covalent, whereas, the *s*-block perovskites are ionic in nature. The covalent and ionic nature of this compound correlated with the electronegativity of the B metal which is discussed later in detail. Therefore, the VBM and CBM will be different for these two classes of perovskite. It has been reported several times for the *p*-block perovskites the A atom doesn't have any major contribution to the VBM and CBM [38,39]. The valance band is mainly composed of the antibonding states of B-*s* and X-*p* orbitals [40]. For example, Fedrico et al. found that in $MAPbI_3$, the VBM is formed by antibonding states of Pb-6*s* and I-5*p* orbital [41]. Murtaza et al. also reported the same interaction between Pb and X at the VBM for all $CsPbX_3$ (X= Cl, Br, I) compositions [42]. On the hand, several researchers have reported the presence of non-bonding B-*p*, and X-p orbitals at the CBM for the same series of *p*-block perovskites. [41,42] The nature of both VBM and CBM for *s*-block perovskites are less studied compared to the *p*-block perovskite. Kang et al. reported for $CsCaI_3$ the I 5*p* and Ca 3*d* orbitals are a major contributor at the VBM and CBM, respectively [43]. Figure 6. represents the band structure of $CsPbI_3$ (*p*-block) and $CsCaBr_3$ (*s*-block).

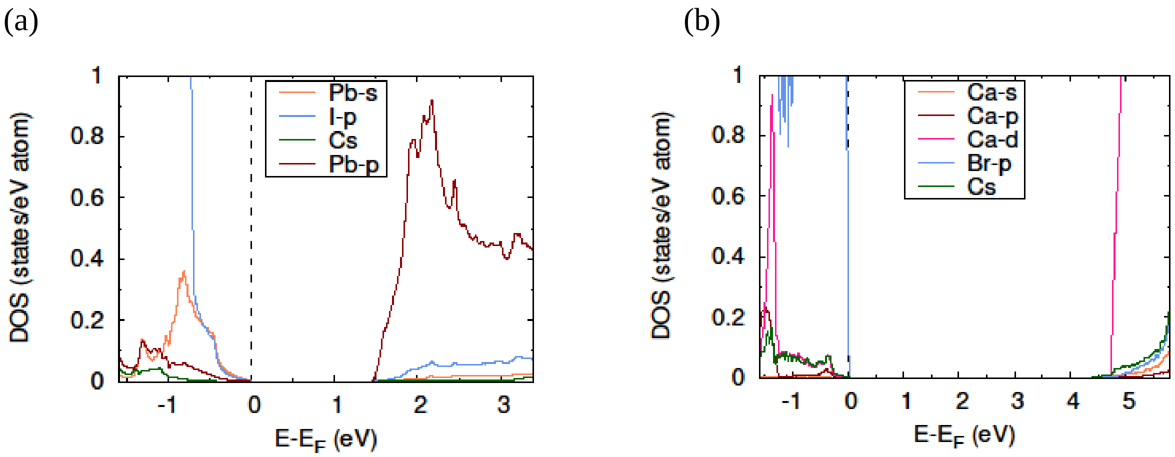

Figure 1.3 The partial density of states (DOS) of cubic (a) $CsPbI_3$ and (b) $CsCaBr_3$

It is clear from the above discussion that based on the crystal structure and composition or chemistry of the perovskites, the band structure changes. Therefore, it is necessary to look in more detail how these factors affect the band structure. A detail study on the effect of crystal structure and the chemical composition on the band structure is discussed in the next section.

1.3 Chemistry-Electronic property relationship of perovskite compound (ABX_3)

In the metal halide perovskites, the chemical bonding between the metal (B) and the halogen (X) atoms plays an important role in determining the electronic structure or the bandgap. It has been widely observed the intrinsic properties of the metal and halogen such as atomic radius, electronegativity difference between metal and halogen, etc. are linked with the bandgap of the perovskite. Also, factors as crystal structure, distortion of the [BX_6], etc. have a significant influence on the electronic property of the perovskite compounds.

1.3.1. Electronegativity difference:

Electronegativity of an element is defined as the ability to attract negative charge cloud. Electronegativity (E.N) difference between two atom dictates the nature of the chemical bond between two atoms. E.N difference between two atoms equals to or higher than 1.7 in the Pauling scale [44] is considered as ionic, whereas, 0.5-1.6 is polar covalent, and less than 0.4 is covalent [45]. The bond between a metal B and the halogen X for *s*-block perovskite is ionic, and for *p*-block, it is polar-covalent or covalent. For instance, the bond between Pb and I in $CsPbI_3$ or $MAPbI_3$ is covalent due to the E.N difference of 0.33 and in $CsCaI_3$ the bond between Ca and I is ionic because of the high E.N of 1.7 between Ca and I. It has been reported that higher E.N difference between the metal and the halogen is responsible for wider bandgap while smaller difference produces lower bandgap [46-48]. In an ionic bond, the electronic charge cloud is less dispersed along with the bond, and it is localized near the nuclei, which results in shorter bond-length between the metal and halide and a wide bandgap. Hence for a fixed metal, the bandgap can be altered by changing the halogen composition as the electronegativity difference between B-X bond changes from F, Cl, Br to I. The calculated and experimental bandgaps of MAPbX$_3$ (X= Cl, Br and I) are listed below, and it is quite evident that changing the E.N difference by varying halogen composition change the bandgap for these compounds. Substituting I with Br and Cl shifts the VBM at a lower energy level causing the larger bandgaps in MAPbBr$_3$ and MAPbCl$_3$ [49]. The energy of the VBM (position on the bandgap) mainly depends on the energy of the *p*-orbitals of halogen atom.

Substituting I with Br and Cl shifts the VBM at a lower energy level causing the larger bandgaps in MAPbBr$_3$ and MAPbCl$_3$ [49]. The energy of the VBM (position on the bandgap) mainly depends on the energy of the *p*-orbitals of halogen atom.

Table 1.1 Represents the DFT-calculated and experimental bandgap for cubic MAPbX$_3$ (X= Cl, Br and I)

System	E.N difference (Pauling scale)	Calculated (eV)	Experimental (eV)
MAPbCl$_3$	0.83	1.54[49]	1.55[50]
MAPbBr$_3$	0.63	1.95[49]	2.00[51]
MAPbI$_3$	0.33	2.42[49]	2.88[52]

From I (5*p*) to Br (4*p*) to Cl (3*p*) the energy of the *p*-orbital decreases and hence the position of the VBM shifted to a lower energy level. Similarly, for a fixed halogen atom composition the bandgap will change with the varying metal atom. The variation in the bandgap with respect to the electronegativity of the metals is shown below for a series of $MABI_3$ perovskite compounds, where B is the metal atom (Figure 1.4). The higher electronegativity of metal atom decreases the E.N difference between B and I, which results in lowering the bandgap.

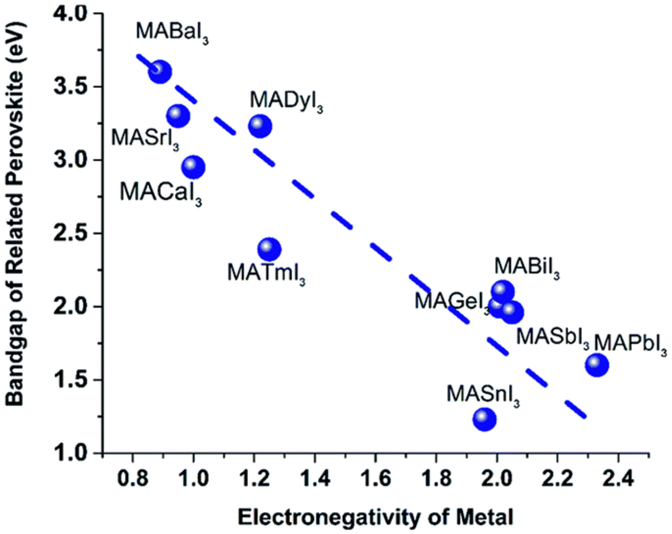

Figure 1.4 Dependence of $MABI_3$ bandgap on the electronegativity of B atom [53].

1.3.2 Effect of atomic size

Besides playing a key role in predicting the formability or the stability of a perovskite structure, atomic size of A, B and X have pronounced impact on the energy of valance and conduction band, especially on the VBM and CBM. In Pb, Sn-based halide perovskite the major contribution of VBM comes from the n*s* orbital of Pb or Sn and n*p* orbitals of the halogen atom. Whereas, the CBM consist of n*p* orbital of Pb or Sn [41,42]. Atomic size is strongly correlated with the energy of an orbital, and hence, the position of the VBM and CBM shows dependency on the atomic size. The effect of atomic size and electronegativity on the electronic structure of halide perovskites can be well understood from the behavior of mix-halide or mix-cation perovskite compound. Several studies, for example [54-56] have reported an improved power conversion efficiency, low hysteresis, and high defect tolerance by using a mix-halide or mix-cation perovskite composition. The partial substitution of Cl and Br atom in the tetragonal $MAPbI_3$ increase the band gap from 1.54 eV to 1.64 eV in $MAPbI_2Br$ and 1.75 eV in $MAPbI_2Cl$ [49]. The smaller size and higher electronegative Cl and Br compared to I, affect the VBM (consist of *p*-orbital of halide and 6*s*-orbital of Pb), and hence we observe the increase in the bandgap. Similarly, a tuned band gap and improved efficiency have been reported by using a varying composition of FA and MA cation in $MA_xFA_{1-x}PbI_3$ [57]. Although the A cation doesn't contribute to the VBM or CBM, it is observed that the size of A cation influences the bandgap or other optical property by distorting the $[BX_6]$ octahedra [58,59].

1.4 Crystal Structure-Electronic property relationship of perovskite compound (ABX_3)

The organic-inorganic Pb, Sn halide-based perovskites, which are widely studied as a solar cell material is mainly found in three temperature-dependent crystal structure or phase. For instance, all $MAPbX_3$ show a high-temperature cubic phase (α) followed by a tetragonal phase (β) at the intermediate temperature and an orthorhombic phase (γ) at the low temperature [60]. Apart from these three phases, a non-perovskite δ phase exists in some ABX_3 perovskites, such as $CsPbI_3$ and $CsSnI_3$ [61,62]. Figure 4. Represents different crystal structure of $MAPbI_3$. In cubic structure, the $[BX_6]$ octahedra oriented such a way that all the B-X-B bond angles are 180^0, whereas, the tetragonal and orthorhombic phase have tilted octahedra with B-X-B bond angle less than 180^0. A vast number of studies have found that a distortion of the $[BX_6]$ octahedra or a reduction of B-X-B bond angle from the affect the bandgap [63-65]. It is seen that with increasing distortion or the reduced symmetry, the band gap increases. Xiao and co-workers reported that for $CsPbI_3$, as the Pb-I-Pb bond angle (180^0) in cubic case reduces to 136.4^0 for a distorted structure (tilted $[BX_6]^{4-}$ polyhedral), the band gap increases to 1.66 eV from 1.48 eV [66]. The huge deviation ($\sim30^0$) of Pb-I-Pb bond angle shifted the VBM at the lower energy and increase the bandgap in the distorted structure. For Sn and Pb based halide perovskite, the energy of valance band maximum (VBM) depends on the antibonding interaction between ns-orbital of Sn (5*s*), Pb (6*s*) and n*p* orbitals of the halogen atom [63-66]. The deviation of the Sn-I-Sn and Pb-I-Pb bond angles from the bond angle (180^0) in the ideal cubic structure causes a reduction in the antibonding interaction between Sn, Pb, and the halogen atom. The reduced interaction between these orbitals lower the energy of the VBM and hence, an increase in the bandgap [66].

1.5 Defect studies on perovskite compounds (bulk)

Crystal defects are inevitably produced during the synthesis of perovskite compounds. Especially the solution processed third generation perovskite solar cells has shown presence of higher concentration of point defect compared to the single crystal based solar cell. For example, a single crystal of $MAPbI_3$ shows lower point defect density (10^{10} -10^{11} cm^{-3}) compared to the solution processed $MAPbI_3$ (10^{16} -10^{17} cm^{-3}) [67-69]. The point defects such as cation or halide vacancy, interstitial and antisite defects are most commonly found in perovskite compounds. Whereas, other defects such as Schottky and Frenkel defect pairs and higher dimensional defect (grain boundary, dislocation etc.) can also be observed in perovskites. Figure 1.5 shows the different kind of defects that can be formed during the synthesis of halide perovskites.

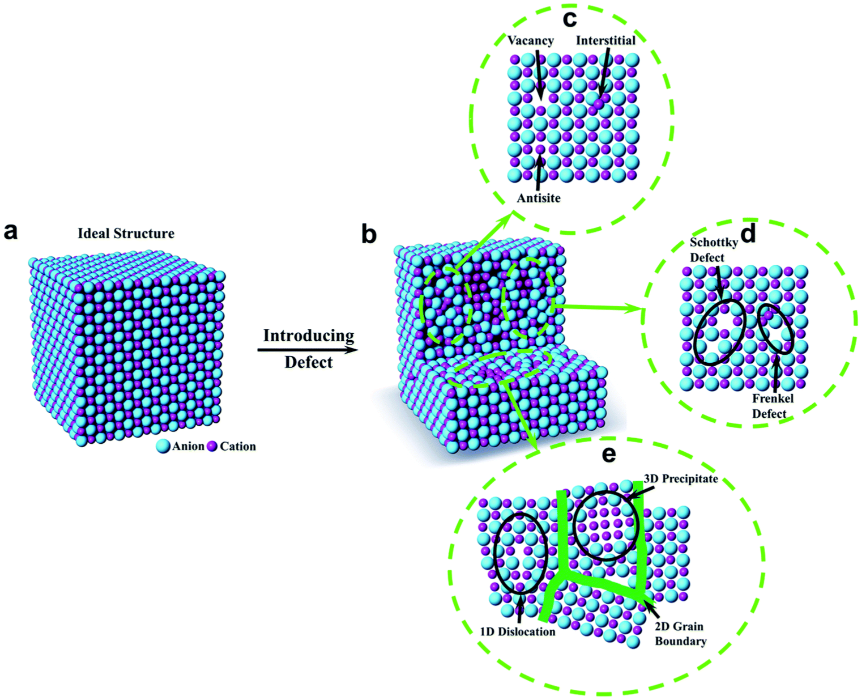

Figure 1.5 (a) Ideal bulk structure without defect and (b) with defect. (c), (d) and (e) represents the common point defects, defect pair and higher dimensional defects respectively.[70]

Concentration of the point defects in halide perovskite depends on the formation energy of the defect. Theoretically, the formation energy of a point defect can be calculated by the following equation $E^f[X^q] = E_{tot}[X^q] - E_{tot}[bulk] - \sum_i n_i\mu_i + qE_F + E_{corr}$

Where $E^f[X^q]$ is the formation of a defect at the charge state q. $E_{tot}[X^q]$ and $E_{tot}[bulk]$ are the total energy of the supercell with and without the defect. μ_i is the chemical potential of the individual species. The n_i term indicate the number of atoms added or removed from the super-cell to create the defect. Finally, the E_{corr} is the correction term accounts for the finite k-point sampling or the electrostatic or elastic interaction between the supercells. Also, the defect charge transition level can be calculated by the equation

$$\epsilon\left(\frac{q}{q'}\right) = [E(X,q) - E(X,q') + (q-q')(E_{VBM} + \Delta V)]/(q-q')$$

Where $\epsilon\left(\frac{q}{q'}\right)$ corresponds to the charge transition level for defect X.

The performance of a perovskite solar cell was found to have a direct dependency on the concentration of these point defect. The point defects with high concentration such as cation and halide vacancy do not form a trap state on the middle of the band gap, whereas, the antisite defect, which is formed at the high halide concentration, produce mid-gap localized states (trap). The trap state act as a recombination center for the minority charge carriers (electron and hole). Recombination at the trap state reduce the lifetime of electron and holes and lowers the open circuit voltage. So, the understanding of the defect properties for these compounds is very crucial. Hence, a remarkable progress on the study of defect properties of halide perovskite compounds has been observed in the last decade [71-75]. Basically, a vast amount of work can be found where researchers theoretically calculate and report the formation energy and the location of all the possible point defects on the bandgap at different chemical potential range. A good example of such defect study on the pseudo cubic structure of $MAPbI_3$ where Yin et al., studied all possible point defects namely vacancies (V_{MA}, V_{Pb}, V_I), interstitials (MA_i, Pb_i, I_i) antisite defects (MA_{Pb}, Pb_{MA}, MA_I, Pb_I, I_{MA}, I_{Pb}) at different chemical potential condition. The position of the defects as well as their transition levels on the band-gap are shown below [73].

The defects with low formation energy (higher concentration) such as V_{Pb}, V_I etc. produce shallow level (with respect to the band edges) defect (not harmful) whereas, defects with high formation energy (Pb_I, I_{Pb} etc.) form harmful deep trap state. It should be noted that the (0/1-), (1-/2-) etc. represent the transition from one charged state to another. So, the (0/1-) represents the transition from charge neutral state to -1 charged state.

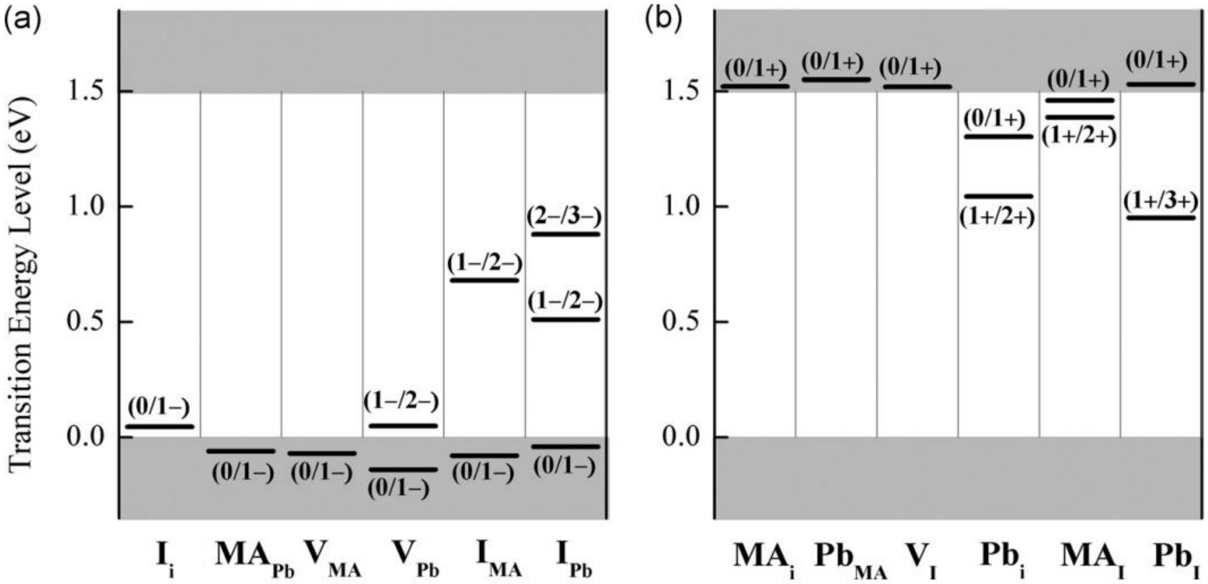

Figure 1.6 The position and the transition level of all point defects (a) acceptor type (b) donor type. The energy levels are measured with respect to the Fermi energy. The VBM is set on zero energy level [73].

The origin and the transition level of a defect state are closely related to the chemistry and crystal structure of the material. Du performed similar defect studies on tetragonal $MAPbI_3$ [73]. In this study, they have shown the I_{MA} antisite defect (MA replaced by I) for the (0/1-) transition level produce a deep trap level, whereas, in cubic $MAPbI_3$ the same I_{MA} defect creates shallow level defect for the same transition. The origin of the deep trap in tetragonal $MAPbI_3$ is due to the I-trimer formation. The distortion at the defect site due to the formation of I-trimer pushes up the energy level to the middle of the band gap. Besides crystal structure, the defect properties can also be tuned by changing the chemical composition. While comparing the defect level and defect density between $MAPbI_3$ and the mixed halide perovskite $MAPbI_{3-x}Cl_x$, Jiang et al. found that the defect level of these two perovskites is almost same, but the defect density of $MAPbI_{3-x}Cl_x$ is almost half of $MAPbI_3$ [75]. Du et al. in their theoretical study pointed out that the formation of iodine interstitial in $MAPbI_{3-x}Cl_x$ subdued due to the presence of the Cl atom [74]. They have also suggested that the Cl_i^- (Cl interstitial defect) in $MAPbI_{3-x}Cl_x$ creates a shallow acceptor level which doesn’t act as an effective recombination center. Whereas, in $MAPbI_3$, the iodine interstitial defect forms a deep level (trap). Substituting I atom with the Cl in $MAPbI_2Cl$ causes the decrease of the Pb-I(Cl) bond distance and the smaller lattice constants than $MAPbI_3$. The smaller lattice constant of $MAPbI_2Cl$ suppress the I_i or iodine interstitial. [74]

1.6 Surface property

Although the bulk properties of light absorbing material (perovskite) are important factors determining the superior performance of the perovskite-based solar cell, the surface properties of these materials are also crucial to understand the power conversion efficiency (PCE) of a solar cell. Typically, in all perovskite-based solar cell architecture, the photo absorber perovskite surface is interfaced with carrier transfer layer such as- electron transport layer (ETL) such as PCBM [76], TiO_2 [77] etc. and hole transport layer (HTL) such as organic part of Spiro-OMeTAD , PEDOT: PSS [78]. The selection of ETL and HTL material and the surface properties of perovskite controls the efficiency of charge separation in solar cells [79-81] and hence, the surface property directly affect the performance of the solar cell. Also, the surface termination dependent defect properties influence the overall device performance [82]. Surfaces can be polar or non-polar. In a polar surface the polar instability occurs due to the presence of a dipole moment perpendicular to the surface. The polar instability can be compensated by adding foreign species externally to the surface, partially filling the electronic states or by changing the surface composition [83,84]. All these compensation mechanisms can be responsible for the creation of surface defects. So, working with a charge neutral surface is highly advisable. For the tetragonal structure (110) and (001) planes are considered as charge neutral surface, similarly for cubic crystal structure the charge neutral surface (001) is widely studied [85-86]. Figure 1.7 shows a representative model of (001) surface of $MASnI_3$ for both MAI and SnI_2 termination.

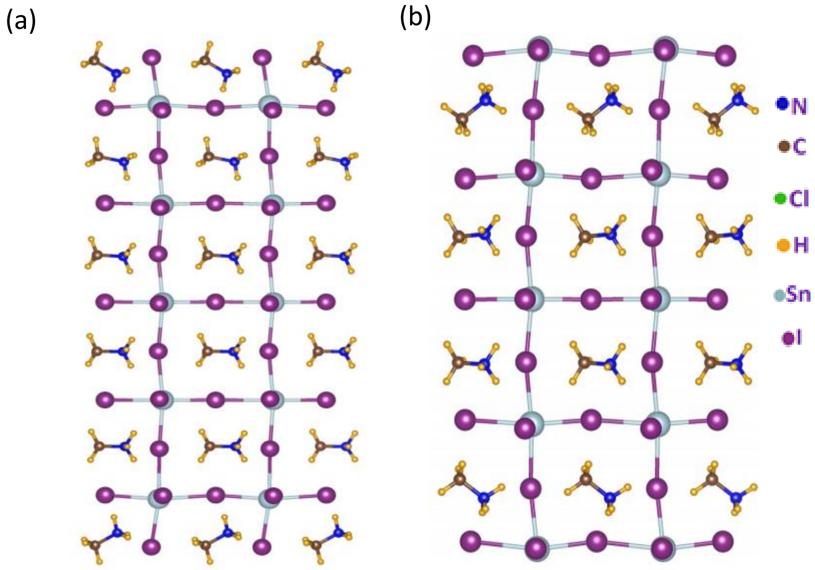

Figure 1.7 (a) MAI and (b) SnI_2 termination of tetragonal $MASnI_3$.

Haruyama and coworkers first studied the termination dependent structural stability and electronic property of tetragonal $MAPbI_3$ surfaces [88]. In this work, they have considered (110), (001), (100) and (101) surfaces of tetragonal $MAPbI_3$ with all type of PbIx polyhedral termination. They found that (110) and (001) surface with both vacant (absence of few PbI_2 units from the PbI_2-rich flat terminations) and PbI_2-rich flat terminations (All PbI_2 units are present) shows similar electronic structure of bulk $MAPbI_3$, and they do not form any mid gap state (trap). The absence of the trap state facilitates the long minority carrier diffusion length, which is essential for better device performance. Further, the shallow level surface state in (110) and (001) flat termination surface helps in transferring the holes efficiently.

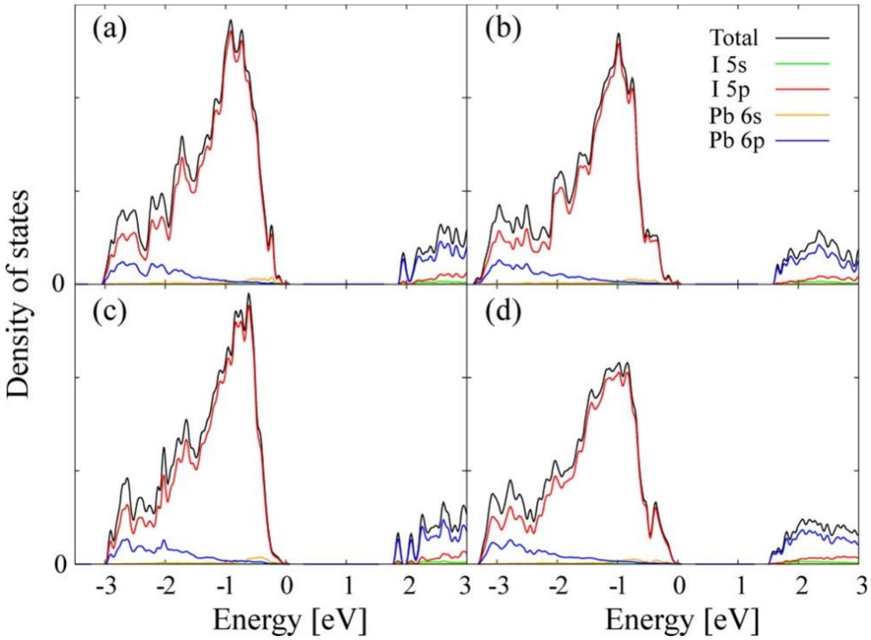

Figure 1.8 Partial density of state (PDOS) of the $MAPbI_3$ surfaces for (a) (110) vacant, (b) (110) flat, (c) (001) vacant, (d) (001) flat terminations [88].

As mentioned earlier the Pb, Sn-based compounds are extensively studied in past one decade. However, the understanding of the *s*-block perovskite compounds is still in nascent stage. All the major studies on Pb, Sn-based studies focuses on increasing performance of the device by tuning the bandgap. Bandgap of a perovskite material depends on the position of VBM and CBM on the band structure, which is further reliant on the atomic orbital interactions. So, a profound knowledge of the chemistry of the individual atoms of a perovskite structure is very essential to understand to predict the bandgap of any perovskite compounds. In this work, we establish a link between the chemistry of the individual atoms to the bandgap for a series of *s*-block compounds. Based on the chemical composition of induvial atoms, we not only developed the understanding of the electronic structure of these *s*-block perovskites, but also linked the bandgap of these compounds to the intrinsic properties such as bond-dissociation energy, atomic or ionic size and electronegativity of the individual atoms. With the help of these intrinsic properties, one can successfully predict the band gap of a perovskite compound. Further, we explained the effect of antisite defect on bulk perovskites. Also, the position of the defect state on the bandgap depends on the chemical composition and the crystal structure of the perovskites. This work also aims linking the intrinsic properties of the induvial components to the defect state formed. Hence, based on these intrinsic properties one can tune the bandgap and the position of the defects.

Chapter 2: Methodology

Density functional theory (DFT) is the most widely used theory for the electronic structure calculations to predict the ground state properties of the material [89,90]. DFT predicts a large variety of ground state properties such as ionization energies, molecular structure, atomization energy, etc. In DFT, the energies of the orbitals are obtained by solving the time-independent many-electron Schrödinger equation [91,92] by considering the electron density. The total energy of a many electrons system is given by the equation-

$$\hat{H} = -\frac{1}{2}\sum_{i}^{N} \nabla_{i}^{2} + \sum_{i}^{N} \sum_{j\neq i}^{N} \frac{1}{r_{ij}} - \sum_{i}^{N} \sum_{A}^{M} \frac{Z_A}{r_{iA}} \tag{2.1}$$

The $\hat{H}$ is the sum of three terms; the first term is the kinetic energy; the second term is the energy due to the coulombic interaction between electrons and, the last term is the interaction with the external potential. The solution of the equation (2.1) is not straightforward. To solve the energy from the above equation, Kohn and Sham introduced the concept of electron density. They considered the electron density to find the ground state energy of a many-electron system. The Kohn-Sham equation [89] is the modification of the SchrÖdinger equation and written as-

$$\left[-\frac{1}{2}\nabla^{2} + v_{eff}(r)\right]\psi_i = \varepsilon_i \psi_i \tag{2.2}$$

And the electron density $n(r) = \sum_i |\psi_i\,(r)|^2$ (2.3)

$v_{eff}(r)$ is the effective potential, which is the sum of external potential (v_{ext}), Hartee or, coulombic potential (v_H), and the exchange correlation potential (v_{XC}). The exchange correlation term includes all the interactions in the many-electron system. One of the major drawbacks of DFT is to find the exact functionals for the exchange correlation function for the complex systems. Local density approximation (LDA) [93] and the generalized gradient approximation

(GGA) [94] are the most commonly known exchange correlation function. In the first approximation, the total energy term only considers the local energy density of the electron interactions. Whereas in GGA, an additional term representing the electron density gradient is considered for total energy calculation. It has been reported that the accuracy of calculation is improved with the GGA over the LDA [95,96].

For our DFT calculation, we used the Vienna *ab initio* Simulation Package (VASP) [97-100]. We considered GGA with Perdew-Buke-Ernzerhof (PBE) [101,102] functionals to calculate the ground state energy of our bulk systems (with and without defect) and as well as for the surface. VASP performed a self-consistent run, which is an iterative method to get the ground state energy during structural relaxation. A schematic of the self-consistent run [103] is presented in the Figure 2.1. In this self-consistent run, an initial value of the electron density assumed to calculate the $v_{eff}(r)$ from the Kohn-Sham equation and calculate the total energy of the system. The numerical iterations continue until the energy and force criteria for convergence are fulfilled.

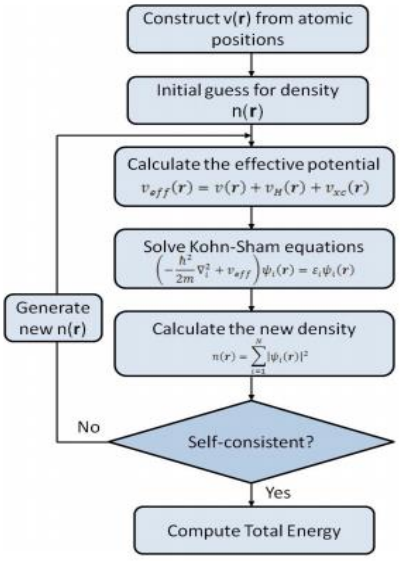

Figure 2.1 Schematic of a self-consistent run.[103]

2.1 Computational details for the bulk and bulk with defects

We performed all the electronic structure calculations of bulk ABX_3 (A=Cs, B= Ca, Sr, Ba and X= F, Cl, Br, I) without and with defect structures using the Vienna *ab Initio* Simulation Package (VASP) [97-100]. The Perdew, Burke, and Ernzerhof (PBE) [101,102] generalized gradient approximation (GGA) was considered for these first principle calculations. We did not consider the effect of spin-orbit coupling for our calculation due to the absence of the spin-orbit effect for the *s*-block metals. The cutoff energy for the plane wave basis was set as 400 eV. We allowed the system to change ionic positions, cell volume, and cell shape during structure relaxation. We let the structure to relax till the force on each atom is 0.01 eV/Å (force convergence criteria). We considered two different crystal symmetry, namely Cubic and Orthorhombic for all the perovskite compositions. In the cubic system, we used 3 × 3 × 3 supercells with 135 atoms and for the orthorhombic system 2 × 2 × 1 supercells with 80 atoms were used. The supercell is consisting of several unit cells. Antisite defect (X_B) was created inside the supercell by removing one B metal and replacing with one X halogen atom. To simplify the calculations with the supercell and supercell with antisite defect, we used the concept of irreducible Brillouin zone (IBZ) [107] which have the same property as the supercell. The IBZ can be characterized by discrete K-points, and all the required ground state properties can be obtained by the combination of IBZ and K-points [108]. We considered the tetrahedron method [109] for Brillouin-zone characterization. For structural relaxation in the bulk (with and without defect) cubic case, we used a 3 × 3 × 3 k-points whereas for the orthorhombic structures 2 × 2 × 3 k-points were used. The electronic structure can be calculated in terms of the density of states (DOS), which is defined as the number of electronic states present per unit energy range. An 8 × 8 × 8 and 8 × 8 × 12 г-centered k-point grid is used for the density of states (DOS) calculation for cubic and orthorhombic structures, respectively. The charge densities and crystal structures are visualized by VESTA software [104-106]. The LOBSTER [110] software is used to extract the bonding information between the atoms. From the self-consistent run in VASP, we found the solution of the wave function ψ_i and the eigenvalues ψ_i (band energies). LOBSTER determines the overlap matrix (S) and a transfer matrix (T) with the help of a local auxiliary basis, and from the S and T, it calculates the Crystal Orbital Overlap Population (COOP) and Crystal Orbital Hamilton population (COHP). COOP and COHP are the indicators of the bonding/antibonding interactions between atoms. For example, the negative value of the COOP means the antibonding interaction between atoms, whereas the positive COOP signifies the positive overlap between atomic orbitals and hence it is considered as the bonding interaction.

2.2 Computational details for surface calculations

Similar to the bulk calculations, the structural relaxation of the (001) surfaces is performed by the VASP considering the PBE-GGA functional. For our calculations, we have considered two different terminations – AX and BX_2 with eleven layers of thickness in each (fig. 2.2). A vacuum of more than 40Å is applied between slabs to nullify the effect of interaction between the slab and its periodic image. All the slab models of surfaces are optimized without changing the volume and shape of the cell, unlike the bulk structures. The position of the ions or atoms is optimized until the force on each ion or atom become 0.01 eV/Å. Also, a $4 \times 4 \times 1$ Γ-centered k-point grid is used for the relaxation of the surfaces. The effective atomic charges of all surface atoms are calculated using the principle of Bader charge analysis [25] and Chargemol [150] software. Unlike the bulk calculation here, we consider the dipole correction [111] to eliminate any additional electrostatic interactions between layers.

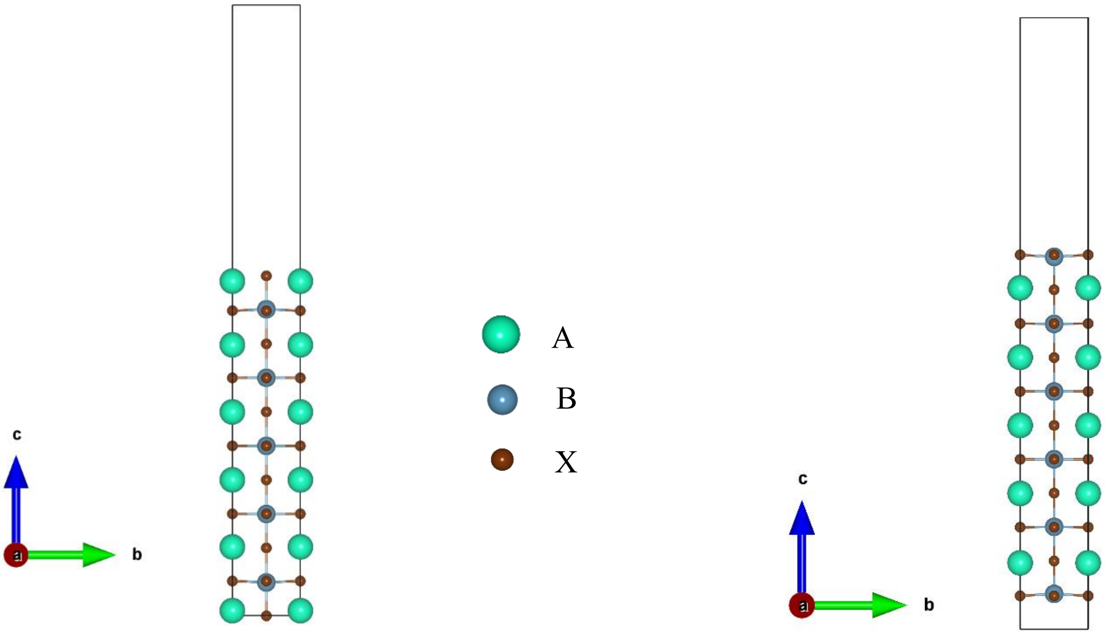

Fig 2.2 The slab model for (001) surface of (a) AX and (b) BX_2 termination.

Chapter 3: Composition and structure dependent impact of antisite defect (X_B) on the electronic structure of all-inorganic $CsBX_3$ (B= Ca, Sr, Ba and X=F, Cl, Br, I) perovskites

3.1 Introduction

In the chapter 1, we have discussed the excellent electronic properties and application of common Pb-based halide perovskites. Despite of showing excellent photovoltaic or electronic properties, lead based perovskite compounds are often criticized for its negative environmental impact due to the lead toxicity [113,114]. So, the focus shifted more towards the replacement of Pb^{2+} ion with other bivalent cation in the periodic table to achieve similar optoelectronic property. Several computational and experimental studies suggested *s*-block elements (Mg, Ca and Sr) can be used as a replacement of lead in these perovskite compounds [115,116]. A representative of *s*-block perovskite, $ASrI_3$ (A=Cs, MA) have large band-gaps and higher effective mass for holes and electrons compared to $APbI_3$ (A=Cs, MA) type compounds. But $ASrI_3$ shows higher value of optical absorption coefficient at the range of 200-300 nm and hence has a greater optical absorption at the ultraviolet range compared to $APbI_3$ [115]. Although there is a very limited application of these *s*-block based halide perovskite compounds as a photovoltaic device, they have shown potential for scintillator device applications [117-119]. In recent years, there has been growing interest in the use of doped inorganic s-block halide perovskite single crystal as a scintillator device as an x-ray and gamma-ray detector [120]. The photovoltaic or scintillation properties of a compound strongly depend on its crystallographic structure. The crystallographic structure also has a significant dependency on the synthesis condition of the crystal as we discussed in detail in the first chapter. Further, crystal defects are unavoidably produced during the synthesis of any crystalline material which affects their performance in device applications. For instance, the high concentration of point defects such as vacancies or antisites evoke harmful phenomena, such as high hysteresis of current-voltage curves [121,122] and large dielectric constant [122,123] which have a negative impact on the photovoltaic performance. A considerable progress in the understanding of point defects and their impact on electronic properties for *p*-block (Pb, Sn and Ge) based perovskite have been achieved in the recent years [124-129]. The most commonly observed point defects are- cation and anion vacancies, interstitials, and antisite defect. It has been reported that the defects with the low formation energy such as cation and anion vacancies produce shallow levels in most of the Pb, Sn based perovskite compounds [124,130]. On the other hand, the interstitials and antisite defects are mainly responsible for producing deep levels in the band gap. Deep trap can act as a recombination center of electronic excitons and hence decrease the lifetime of minority carriers [131,132]. Similarly, for the scintillator device, point defects as well as deep levels serve as a scattering and absorbing center is also responsible for the light losses [133]. Hence, the formation of deep trap level in the band gap impairs the performance of photovoltaic and scintillator devices. The performance of these devices can be improved significantly by tuning the position of defect in the band gap. For instance, if we can adjust the position of localized electronic states inside the VBM and CBM or very close to the band edges, the negative impact of the defect on the device performance can be reduced greatly. Hence, the understanding of effect of point defects on the electronic structure as well as their correlation with the composition and crystal symmetry is very essential.

This chapter primarily aims to study the effect of antisite defect, X_B on the electronic property of *s*-block halide perovskite. We further investigate the role of chemical composition and crystal symmetry on the position (with respect to the VBM) of localized electronic state (trap) formed due to the antisite defect. This chapter also discusses how we can tune the position of the localized defect by changing the chemical composition and crystal structure. Also, we have successfully presented a linkage between the intrinsic properties such as bond-dissociation energy, atomic size, covalent and the position of the localized electronic state on the band-gap. The theory discussed here not only give a fundamental understanding of the origin of harmful trap state due to antisite defect, but also give an idea to predict the position of the localized electronic state by reckoning the chemical composition and crystal structure of the compound.

3.2 Result and Discussion

To understand the effect of the antisite defect, X_B on the electronic structure of ABX_3 perovskites, we choose cubic $CsCaBr_3$ for our initial calculation. From our calculation we found the optimized lattice parameter of $CsCaBr_3$ is 5.77 Å, which is in a good agreement with the experimental lattice constant of 5.69 Å [86]. After the structural relaxation, we performed the density of states (DOS) calculation to determine the electronic structure of $CsCaBr_3$ with no defects as well as for the structure with defect. Our calculated band gap for the pristine structure is 4.40 eV (Fig 3.1) which is very close to the experimental band gap value of 4.39 eV [86]. The valance band maximum (VBM) is consist of Br 4*p* states and Ca 3*d* orbitals are the major contributor of the conduction band maximum (CBM), whereas, Cs atom has no significant contribution at VBM or CBM. For the structure with X_B, we have noticed that the antisite defect creates a localized defect within the band gap at the position 0.56 eV (*L*) higher than the VBM as seen in Figure 3.1(b) The *L* represents the relative position of the localized defect with respect to the VBM. This electronic state can act as a trap state for electronic excitons. So, a proper understanding of its origin is essential. From the Figure 3.1(c), we determined that the localized state is originated from the interaction between the defect bromine atom and the six bromine atoms surrounding it with a major contribution from the defect bromine atom (Fig 3.1 (c)). Further, the negative value of crystal orbital overlap population (COOP) in our analysis indicates the presence of an antibonding interaction between 4*p*-4*p* orbitals of antisite Br atom and the surrounding Br atoms (Appendix A A6, figure (a)). From the molecular orbital theory, we know, the energy of antibonding orbitals is higher than the energy of the individual atomic orbital [134]. For this reason, the defect state forms at a higher energy level compared to the VBM. We have also noticed, the bond-length between defect Br atom and the surrounding Br atoms is 2.4 % higher than the initial Ca-Br bond-length. The bigger size of Br atom compared to the Ca atom as well as the repulsion between negative charges of Br atoms caused the increase in the bond-length.

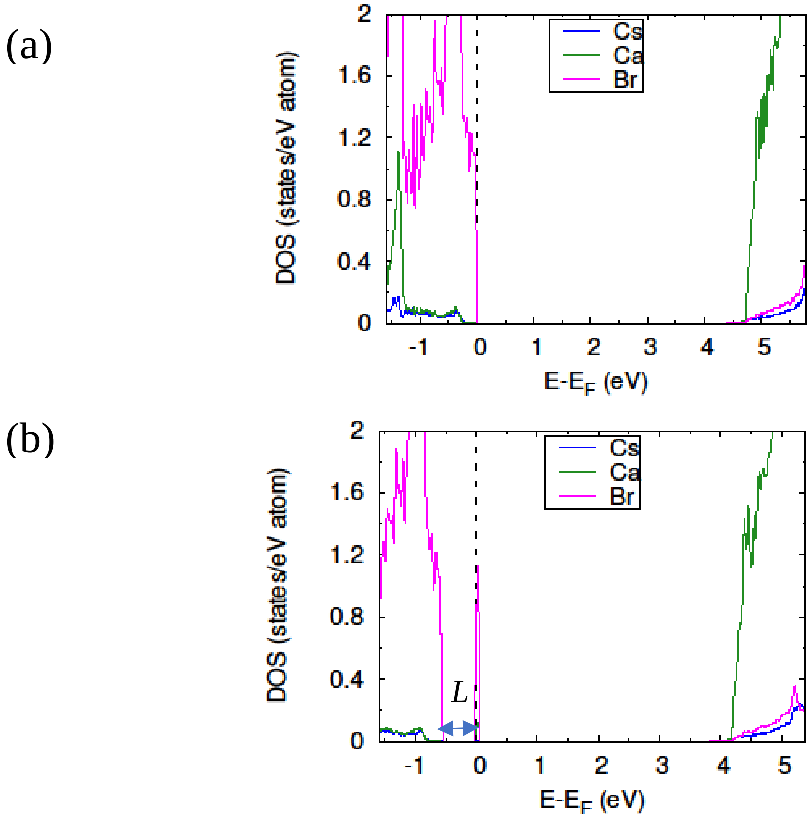

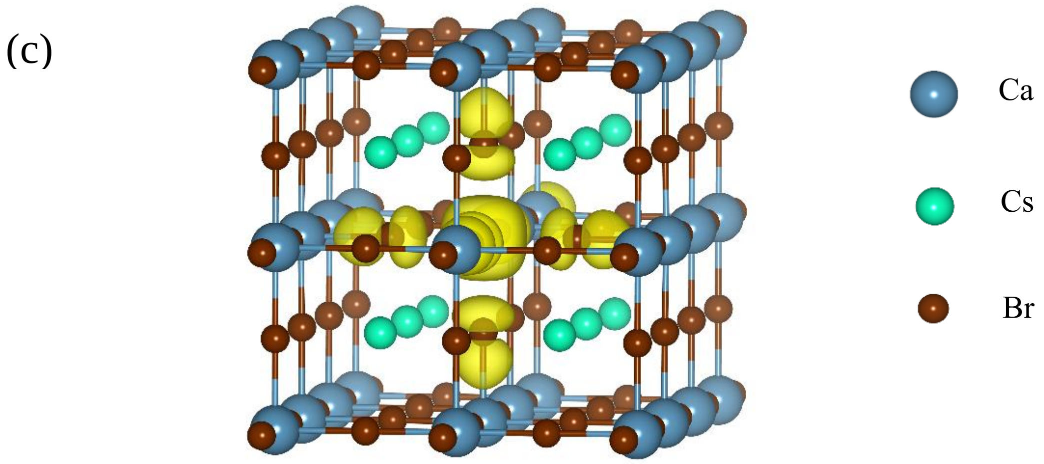

Figure 3.1. The partial DOS of bulk CsCaBr$_3$ (a) without defect and (b) with antisite defect. (c) Electron charge density isosurface plot for the energy range -0.9 to 0.1 eV corresponding with figure (b)

Based on our preliminary observations, we hypothesized that the energy level of the localized defect state created by the antisite defect is strongly depends on the antibonding interactions between the *p*-orbitals of halogen atoms and the size of halogen atom. Hence, the position of the localized defect can be predicted based on the intrinsic properties such as atomic size of X [135,136] and the bond dissociation energy (BDE) of B-X [137,138], which are already known. The value of BDE of a bond tells about the strength of a bond or the quantitative measure of the orbital interactions between molecular orbitals participating in the bond. To test our hypothesis, we included a series of theoretical cubic ABX$_3$ ((A = Cs; B = Ca, Sr, or Ba; X =I, Cl, or F) structures for our calculations [139]. It is important to note that, all the B and X elements we considered for our calculation belongs to the same group in the periodic table. Therefore, the nature of the VBM and CBM is equivalent to the CsCaBr$_3$ structure, i.e., the VBM is consist of X n*p* and CBM is composed of B n*d* orbitals where n is the principal quantum number. Higher the value of n, higher is the energy of the orbital. Based on our hypothesis, we expected for a fixed B metal, with decreasing size of halogen atom from I to F, the position of the localized defect shifts gradually towards the VBM. For example, The $CsCaCl_3$ structure with smaller size of Cl atom (99 pm) and higher BDE of Ca-Cl bond (398 kJ/mol) will produce the localized defect closer to the VBM compared to the $CsCaI_3$ structure with bigger size of I atom (133 pm) and lower BDE of Ca-I (285 kJ/mol) in presence of the antisite defect. Fig. 3.2(a) and (b) shows the calculated relative position of defect states, L as a function of the BDE of B-X bond and the size of X atom. As theorized earlier, for all B (Ca, Sr and Ba) the value of L decreased gradually from I to F making the location of the localized defect state near to the VBM. For all the calculation with fluorine, the defect state integrates with the VBM (shallow defect) and hence, for we consider L as zero. The L is strongly correlated with the BDE of B-X bond and the size of X. Therefore, it is essential to discuss how the intrinsic properties are related to the position of the localized state. Bond dissociation energy is a measure of the strength of a bond. Higher the BDE of B-X means stronger interaction between B and X. The formation of the X_B antisite defect requires the breaking of a B-X bond and replacing of the B atom with a defect X atom. The defect X atom interact with the surrounding X atoms to produce the localized defect state. Stronger bond of B-X bond reduces the interaction of X atoms with the defect X atom and therefore the localized defect state forms at a lower energy level with respect to the VBM. The BDE and bond-length are related directly to each other. Shorter bond has higher BDE. So, to support our argument, we measured the bond-length between antisite defect atom and surrounding halogen atoms and compared with the Ca-X bond-length for the structure with no defect for the $CsCaX_3$ systems. We observed, the bond-length increased is most for $CsCaI_3$ (3.5%) and minimum for $CsCaF_3$ (1.3%) which corresponds to the *L* values for these systems (See table A3, Appendix A A4).

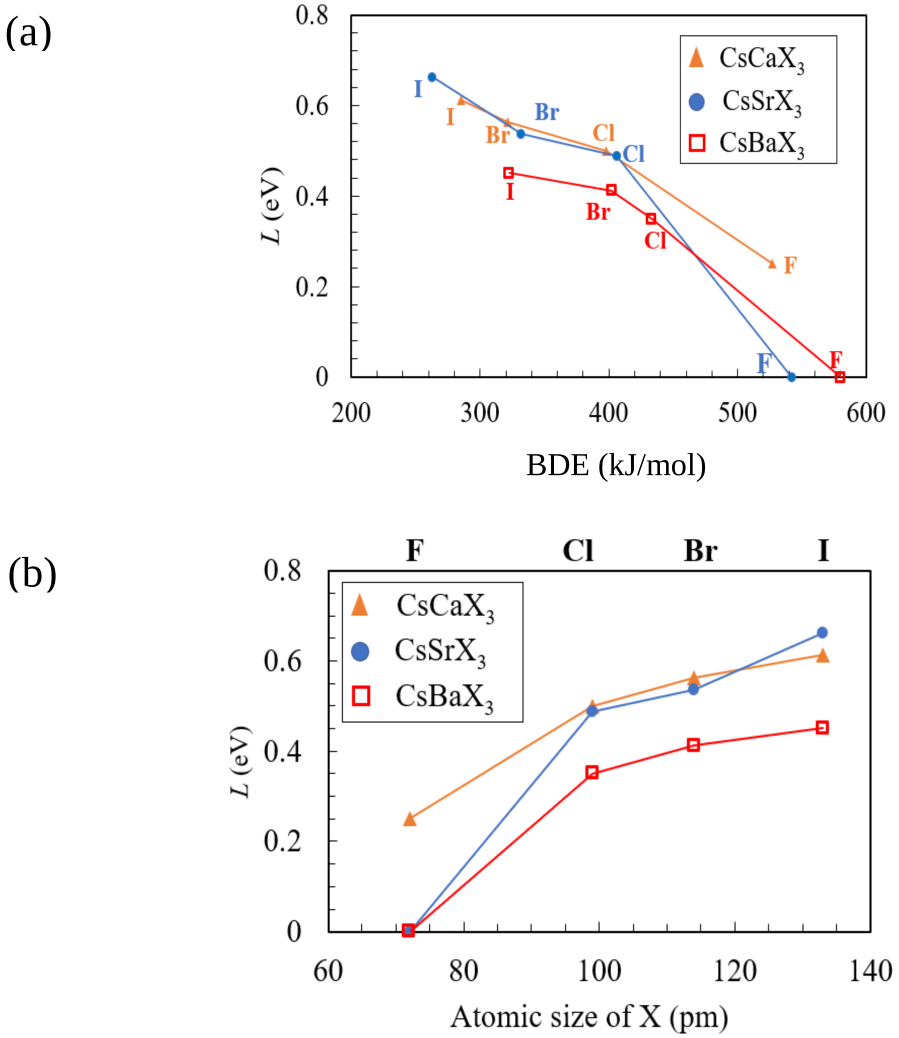

Fig. 3.2 Dependence of cubic $CsBX_3$ (B = Ca, Sr and Ba and X = I, Br, Cl and F) defect position with respect to VBM on (a) BDE of B-X bond and (b) atomic size of X

As discussed before, the localized defect state originated from the n*p*-n*p* antibonding interaction between the halogen atoms, the energy of the interacting *p*-orbitals plays an important role in determining the position of the localized defect state. The energy of outermost *p*-orbitals follows the order F(2*p*) < Cl(3*p*) < Br(4*p*) < I(5*p*). So, the localized state originated from I(5*p*)-

I(5*p*) antibonding interaction in $CsCaI_3$ located at the higher energy level with respect to the VBM compared to the position of the localized defect state in $CsCaCl_3$ due to Cl(3*p*)- Cl(3*p*) interaction. To understand the relation between the energy of the halogen orbitals and the position of the localized defect state, we studied the effect of antisite defect Cl_{Ca} on the electronic structure of $CsCaBr_3$. We found that the Cl_{Ca} creates a localized defect near to the VBM (*L*=0.34) in comparison to the localized defect state forms due to Br_{Ca} (*L*=0.56) (see. figure A24 (c) in the Appendix A). Obviously, the lower energy of Br(4*p*)-Cl(3*p*) antibonding interaction in Cl_{Ca} compared to the Br(4*p*)-Br(4*p*) interaction in Br_{Ca} caused the localized defect to form near to the VBM. Hence, halide perovskites doped with smaller size halogen atom or a mixed-halide perovskite should show less tendency to deep trap formation and therefore a better device performance. To summarize, for the cubic structures, the position of the localized defect state is a function of the BDE of B-X bond and the size of defect X atom. The composition with higher BDE of B-X bond and the lower size of X creates localized defect near VBM and do not form deep trap. Conversely, the compositions with lower BDE and larger atomic size tend to form deep trap state. Also, position of the mid band-gap localized state can be move towards the VBM by doping it with smaller sized halogen atom.

Now, to understand the effect of the crystal symmetry on the electronic structure in the presence of antisite defect we selected the $CsSrI_3$ (a= 4.81 Å, b= 15.78 Å and 12.37 Å) structure with a *Cmcm* (No. 63) space group for our calculation [140]. This orthorhombic structure is different from the ideal cubic structure due to a different arrangement of atoms and the tilted octahedra of [SrI_6] compared to the undistorted octahedral network in a cubic structure. The octahedra consist of one central Sr atom with four equatorial iodine atoms which is in the same plane (equatorial) with the Sr atom and two apical iodine atoms which are located out of the plane concerning Sr (Appendix A A3, figure A23). The (Sr-I-Sr) bond angles are 94.5^0 (equatorial) and 141.8^0 (apical) compared to the 180^0 (Ca-Br-Ca) bond angle in cubic $CsCaBr_3$. Figure 3.3(a) and 3.3(b) represents the electronic DOS of $CsSrI_3$ without and with antisite defect. Our study revealed that unlike the cubic structures, the antisite defect creates localized defect states at two different positions on the band-gap and for the simplicity of discerption they are named as defect-1 and defect-2. The defect-1 lies at the energy level 0.58 eV above the VBM whereas the defect-2 located at relatively higher energy level at 1.6 eV above VBM. The L_1 and L_2 are the measures of the relative position of defect-1 and defect-2, with respect to the VBM. In order to find the origin of both defect-1 and defect-2, we plotted the charge densities at the energy levels where they formed as shown in Figure 3(c) and 3(d). From the isosurface charge density plot it is evident that there are two different kinds of iodine associations which are accountable for formation the defect state.

(a)

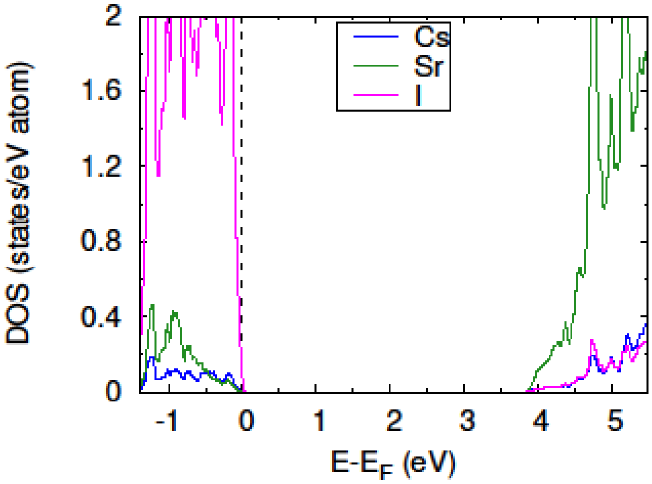

(b)

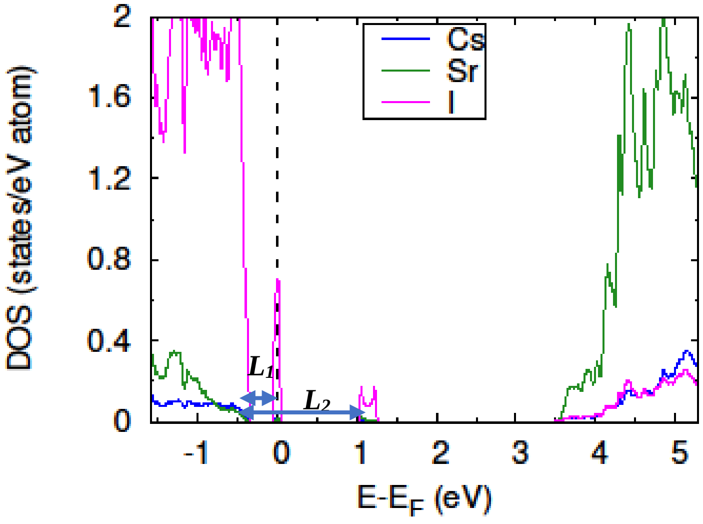

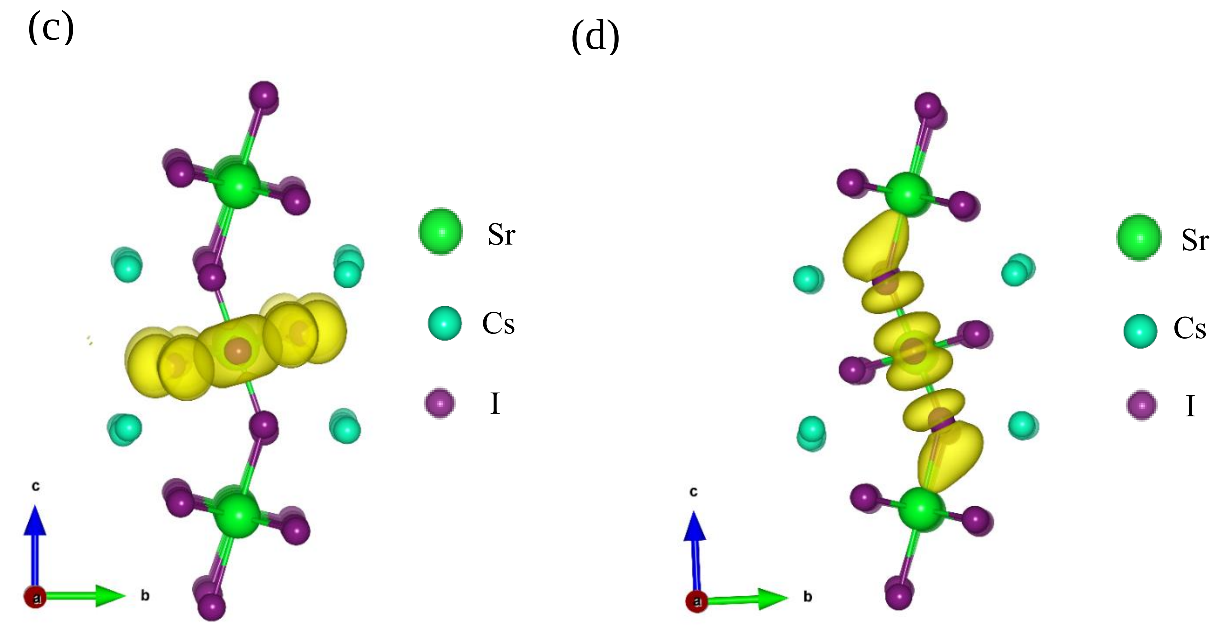

Figure 3.3 The partial DOS of bulk $CsSrI_3$ (a) without defect and (b) with antisite defect. (c) Electron charge density isosurface plot at energy range (c) -0.9 to 0.1 eV (for defect-1) and (d) 1 to 1.2 eV (for defect-2) on the band gap. L_1 and L_2 are the energy gap between the VBM and defect-1 and defect-2, respectively.

Figure 3.4 shows the two different groups of iodine atoms present in the structure with the defect. I1 is the antisite defect. I4, I5, I6, and I7 are bonded with I1 in the equatorial plane and the I2, I3 and I1 are bonded along c-axis (apical). Resemble to the cubic case, the bond-distance between I1 and I4, I5, I6 and I7 (3.81 Å) increased compare to the Sr-I bond-distance (3.33 Å) in the structure with no defect. In contrast, the bond-distance between I1 and I2, I3 (2.94 Å) is lower than the Sr-I bond-distance (3.28 Å) in the pure structure. This observation related to the formation of two different iodine associations correlates well with the previous finding discussing the effect I_{Pb} antisite defect on $MAPbI_3$ (001) surface [134].

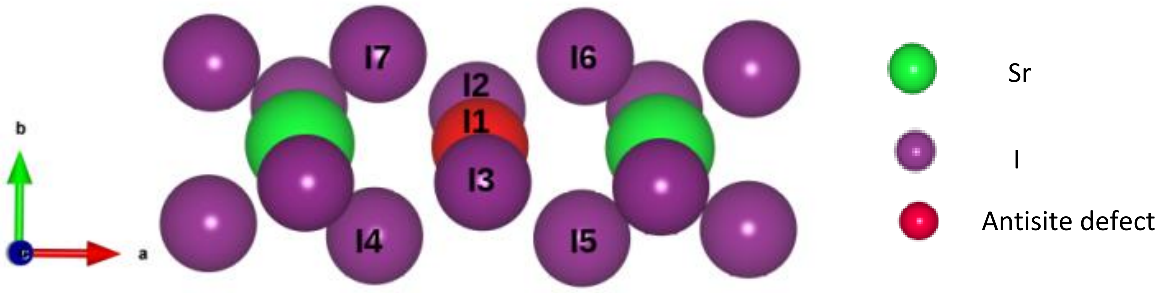

Figure 3.4 Image of the antisite defect and neighboring I atoms within 4 Ȧ. I1 is the antisite defect and I2, I3 aligned in the apical plane I1. I4, I5, I6, I7 and I1 form a group in the equatorial plane.

The Sr-I bond is ionic due to the large electronegativity difference between Sr and I. In presence of the antisite defect I_{Sr} the bond between Sr and I break at the defect site and the negative charge cloud shifts towards the I atom. This I atom with the excess negative charge tend to share charge with the newly introduced I atom by forming covalent bond. To verify the presence of covalency between the iodine atoms, we performed the Bader charge analysis and measured the distance between antisite defect and surrounding I atoms as shown in table 3.1. The Bader charge analysis gives the electronic charges present on individual atoms in a system based on the electron density [141].

Table 3.1. Bader charge and distance analysis of defect Iodine and neighboring I atoms for $CsSrI_3$ bulk with Sr_I defect. I1 is the antisite defect. The average charge on I atoms before introducing defect was -0.776 e.

Iodine (I)	**Charge (e) in the defect-free structure**	**Charge (e) in presence of the defect**	**Percent change in charge (%)**	**Distance from I1 (Å)**
I1		+0.193		
I2	-0.772	-0.394	48.90	2.94
I3	-0.772	-0.394	48.90	2.94
I4	-0.777	-0.660	15.00	3.81
I5	-0.777	-0.660	15.00	3.81
I6	-0.780	-0.660	15.38	3.81
I7	-0.780	-0.660	15.38	3.81

The Bader charge analysis shows the average charge on the iodine atoms in the structure with no defect was -0.776e. In presence of the antisite defect I1, all the iodine atom surround the I1 show a decrease in negative charge, whereas, the charge on I1 is +0.193e. The positive charge on the I1 and the decrease in charge of the surrounding iodine atoms indicates the sharing of charge and hence, the presence of covalency between them. The I2 and I3 atoms show the highest decrement of negative charge (~48%) and the other four iodine atoms which are aligned in the equatorial plane with I1 show ~15% reduction. The different measure of charge sharing, or reduction of negative charge is correlated to the two kind of bond-distances between the I1 and other six iodine atoms. The covalency or sharing of negative charge resulted the shorter bond-length between the I1 and other six I atoms surrounding it. The shorter bond-distance of 2.94 Å between I1, I2 and I3 is very close to the bond-distance between I atoms in I_2 molecule (2.7 Å). Also, the distance between I1 and I4, I5, I6 and I7 (3.81 Å) is comparable to the van der Waals bond-length of I_2 (3.96 Å). The shorter bond-length between the first group of atoms compared to the second group of atoms is due to the higher extent of extent of sharing the negative charge (greater covalency). From the above observation, we named the first group of iodine atoms (I1, I2 and I3) as trimer and the second group (I1, I3, I4, I5 and I6) as pentamer. The defect-1 is originated due to antibonding interaction between iodine pentamer whereas, the antibonding interaction in iodine trimer forms defect-2. Defect-1 forms near the VBM at a lower energy on the band-gap and the defect-2 located at the higher energy level on the band-gap. The different positions of defect-1 and defect-2 can be correlated with the antibonding energy. Also, the antibonding energy is related to bond-distances between the atoms. It has been reported that shorter metal-halide bond favors stronger antibonding interaction. For instance, Sn-Cl in $CsSnCl_3$ has stronger antibonding interaction (energy) compared to Pb-Cl in $CsPbCl_3$ [142]. So, shorter bond-length in the iodine trimer caused the defect-2 to form at the higher level on the band-gap in comparison to the defect-1. From this understanding, it is reasonable to link the covalent bond-distance of halogen molecule to the location of defect states on the band-gap. To test this theory, we consider all the *s*-block orthorohmbic ABX_3 (A=Cs, B= Ca, Sr, Ba and X= F, Cl, Br, I) for our calculation. As the origin of defect-1 is equivalent to the localized defect in the cubic case, we linked L_1 with the BDE of B-X bond and the atomic size of X (Fig 3.5(a) and 3.5(b)). Whereas, in the Fig. 3.5(c) and 3.5(d) we plotted L_2 as a function of BDE of X-X bond and covalent bond-distance of X_2. For defect-1 we observed the same dependency of L_1

on BDE of B-X bond and atomic size of X as we observed before in cubic case for the parameter *L* i.e., compounds with lower BDE of B-X and bigger atomic size corresponds to larger value of L_1. Conversely for defect-2 compounds with higher BDE of X-X or smaller covalent bond-distance of X_2 shows higher value of L_2. For example, $CsSrCl_3$ shows greater value of L_2 (2.21 eV) due to higher BDE of Cl-Cl (436.3 kJ/mol) and smaller covalent bond-distance of Cl_2 (198 pm) compared to the $CsSrI_3$ where the L_2, BDE of I-I and covalent bond-distance of I_2 is 1.40 eV, 152.2 kJ/mol and 266 pm respectively. We were unable to investigate the similar trends for $CsBF_3$ (B= Ca, Sr, Ba) systems because the defect-1 merges with the VBM and measuring the L_2 from the VBM for this case was inappropriate.

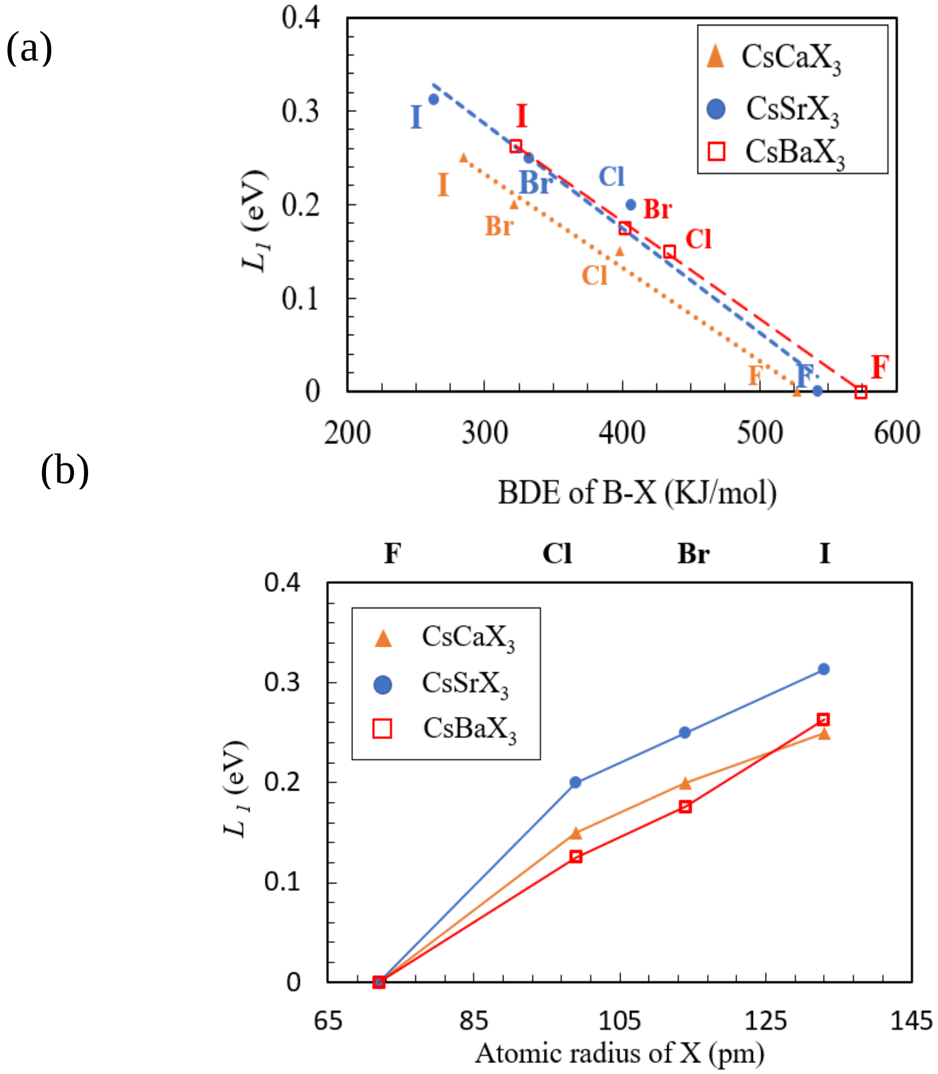

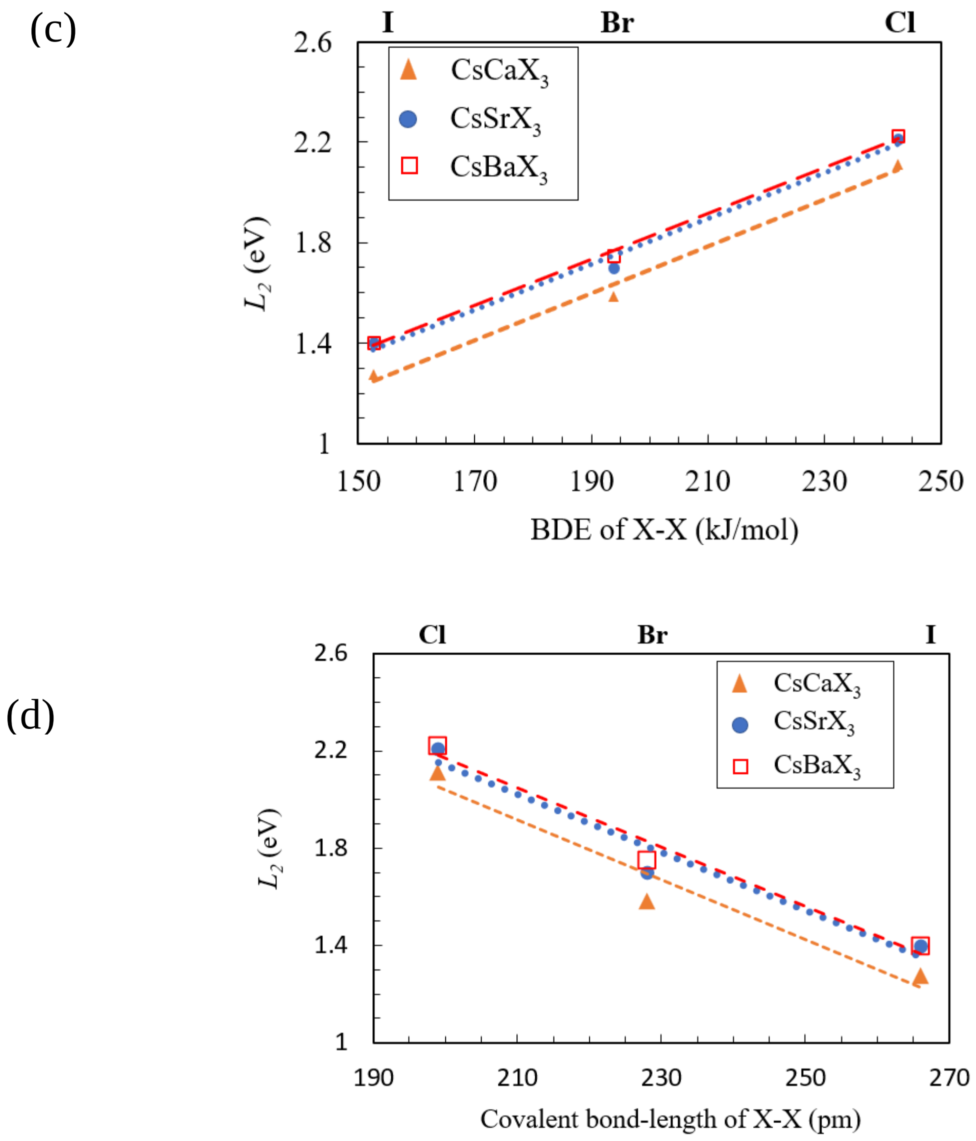

Figure 3.5 Dependence of orthorohmbic $CsBX_3$ (B = Ca, Sr and Ba and X = I, Br, Cl and F) defect-1 position with respect to VBM on (a) BDE of B-X bond and (b) atomic size of X and, defect-2 position on (c) BDE of X-X bond and (d) covalent bond length of X-X.

3.4 Conclusion

From the first principal calculations, we have studied the effect of composition and crystal symmetry on the electronic states form in presence of the antisite defect for all *s*-block halide perovskites. The findings of this study point towards the idea that position of a localized defect state on the band-gap strongly dependent on the composition and the crystal structure of the compounds. Furthermore, we have been able to link the intrinsic properties such as bond-dissociation energy, atomic size, covalent bond-distance etc. with the location of the defect state on the band-gap. So, the proper understanding of the chemical and structural factors influencing the origin of the localized defect provides a powerful tool to tune its position on the band-gap. Defect state forms near the VBM are not harmful as the defect state located at the middle of the band-gap. With the understanding provided in this paper, we can change a harmful trap state to a benign near VBM states. Our study also suggests that lower symmetric orthorohmbic structures, in the presence of antisite defect, produce defects two different position on the energy gap. Whereas, the same composition in the cubic structure shows presence of only one defect state on the band-gap. So, the position of the defect state can be easily altered in cubic structure compared to the orthorohmbic counterpart. Similarly, in presence of the antisite defect the crystal structures with even lower symmetry such as tetragonal and monoclinic can show a similar electronic defect state as the orthorohmbic structure. This is due to the fact in lower symmetry structures the bond-distances between B and X are not equal and the B-X-B bond angles are distorted or smaller compared to the B-X-B bond angle (180^0) in cubic case. So, All the theories we provided here can be used to predict the location of the defect states on the band gap and hence helps to screen materials based on the device application.

Chapter 4: Composition and termination dependent electronic properties of (001) surfaces of all-inorganic $CsBX_3$ (B= Ca, Sr, Ba and X=F, Cl, Br, I) perovskites

4.1 Introduction:

s-block halide perovskite of ABX_3 (A=Cs/MA, B=Ca, Sr and X= F, Cl, Br, I) are important for many electronic material applications. In chapter 3. we have discussed the potential application of the *s*-block perovskites as a replacement of the Pb-based halide solar cell. Especially the same size of Sr (118 pm) with Pb (119 pm) as well as the same +2 oxidation state makes Sr a good replacement of Pb [16, 17]. Although the larger bandgaps of these compounds are discredited for the solar cell application, but Ca, Sr based perovskites are widely studied because of their potential application in the scintillator devices [143-146]. For example, Tm^{2+} doped cubic perovskites $CsCaBr_3$, $CsCaCl_3$ and $CsCaI_3$ shows remarkable light-emitting properties [147]. A vast number of literatures are found discussing the electronic properties of bulk structure but, the understanding of surface electronic properties of these *s*-block compounds is still in the beginning stage. In many devices incorporating a hetero-interface [76-82] with the light absorbing perovskite material improved the performance of the device. The atomic structure of interface depends on the surface atomic structure of the perovksite. Therefore, an understanding of the surface atomic and electronic structure is very crucial.

In their paper Ma et al. [86] briefly explained the effect of surface termination on electronic properties of the $CsCaBr_3$ (001) surfaces. But the effects of chemical composition on the atomic structure surfaces are not discussed. On contrary a fair number of researches are found on the Pb-based perovskite system, particularly on the $MAPbX_3$ surfaces [85, 86, 87]. The *s*-block perovskites are different than the Pb-based or *p*-block perovskite in terms of the nature of bonding between the metal and halogens. So, it is very important to understand the role of chemical bonding on the surface and their impact on the electronic property. This chapter aims to provide a comprehensive understanding of the composition and termination dependent electronic properties of (001) surface of *s*-block based ABX_3 compounds. This chapter discussed about the link between the structural properties of surface, e.g., B-X bond-distance, B-X-B bond angles, etc. with bandgap. Also, we explained that the intrinsic properties of B and X, such as the ionic size, electronegativity difference of B-X, etc. have a dominant effect in determining the surface bandgap as in bulk. Further, the change in the surface bandgap from the bulk is discussed. In a bulk crystal, electrons propagate, and are modelled considering the periodicity of atoms inside the crystals. Surface is a sharp transition from the bulk solid to the vacuum and can be treated as a discontinuity [148]. This discontinuity, and the corresponding weakening potential, leads to the formation surface states. Surface states formed closer to the VBM or CBM are considered as harmless, whereas surface states forming at the middle of a bandgap is detrimental for the device. So, tuning the position of the surface states is paramount.

4.2 Results and discussion:

4.2.1 Bulk properties: structural and electronic

To compare the surface atomic structure and electronic structure with the bulk, we considered the bulk cubic structures of all $CsBX_3$ (B=Ca, Sr and X= F, Cl, Br, I) perovskites, which we have already studied in chapter 3. The initial structural data for all the perovskites is taken from an open resource, the materials project [139]. Similar to other commonly studied perovskite structures such as CsPb(or Sn)I_3 , the $CsBX_3$ structures has a corner sharing octahedra with a B (Ca or Sr) cation bonded with six anions (X). For all $CsBX_3$ perovskites, the B-X bond-distance, as well as the lattice constants, increases from F (133 pm), Cl (181pm), Br (196) to I (220 pm) due to the increasing ionic size. Again, the lattice constant and the B-X bond-distance increase with an increase in the size of the B cation from Ca (100 pm) to Sr (118 pm). It is well established for the perovskite compounds that the electronegativity of B and X [46, 47, 53], size of B or X [53] as well as the structural properties namely bond-distance of B-X bond, B-X-B bond angle etc. can dictate their bandgap [63-65]. Table 4.1 represents the simulated bandgaps for all $CsCaX_3$ and $CsSrX_3$ perovskites. The bandgaps decrease from F to I and the bandgaps of the Ca-compounds are larger compared to Sr.

Table 4.1 Bandgaps (in eV) for all the bulk structure and surfaces.

System	**Bulk**	**CsX**	**BX_2**
$CsCaF_3$	7.34	6.50	5.76
$CsCaCl_3$	5.34	5.22	4.91
$CsCaBr_3$	4.40	4.37	4.17
$CsCaI_3$	3.72	3.42	3.48
$CsSrF_3$	6.24	6.36	5.16
$CsSrCl_3$	4.99	4.94	4.64
$CsSrBr_3$	4.19	4.11	3.98
$CsSrI_3$	3.62	3.1	2.94

The reason behind this observation can be well explained from the understanding of the origin of the VBM and CBM for these compounds. Generally, for all $CsBX_3$, the VBM is comprised of n*p* orbitals of the X atom and the nd orbitals show major contribution at the CBM. Similar to the *p*-block (Pb and Sn-based) perovskites, in *s*-block (Ca and Sr-based) perovskites, the A cation (Cs^+) does not show any major contribution either in VBM or CBM. Pazoki et al. observed the similar nature of the VBM and CBM for the $MACaI_3$ and $MASrI_3$ structures [7]. The positions of the VBM and CBM and the bandgaps are determined by the B-X bond. The intrinsic properties of B and X such as atomic size, electronegativity between B and X etc. plays a key role in determining the nature of B-X bonds (ionic or covalent), bond-length of the B-X bonds. Hence, the intrinsic properties of B and X regulate the position of VBM, CBM and the bandgap value. For a fixed B, the smaller size of X anion lowers the VBM. For instance, F (2*p*) orbitals have the lowest VBM energy, and I (5*p*) has the highest energy among the X atoms. So, the position of the VBM for perovskites with F will be at the lower energy level compared to the I. Whereas, the CBM position will be at the same energy level due to the presence of the same B metal in both the cases. So, the lowered position of the VBM in case of F compared to I give rise to wider bandgap in F than that of I, Table 4.1. Similarly, from I to F the electronegativity (E.N) difference between B and X increases, which also describes the trend of the bandgap from I to F in the Table 4.1. The lower electronegativity difference between B and X makes the compound more covalent and it is observed that compounds with higher covalency show lower bandgap [46-48]. Higher covalency gives rise to the hybrid states which has lower energy compared to non-bonding states. So, the presence of the B-X hybrid states at the CBM lowers the energy level and hence decreases the bandgap. From the discussion it is evident that the effect of B and X atom composition on bandgaps of the *s*-block perovskite can be linked directly with the E.N, ionic size or covalency of B-X bonds. Hence, from here onwards we will correlate the bandgaps with the above-mentioned parameters. Fig 4.1 correlates the bandgaps with the E.N difference between B and X, and with the ionic size of X. It shows the higher electronegativity difference between B and X and smaller size of X anion produce larger bandgaps. The reason behind this observation is already discussed earlier.

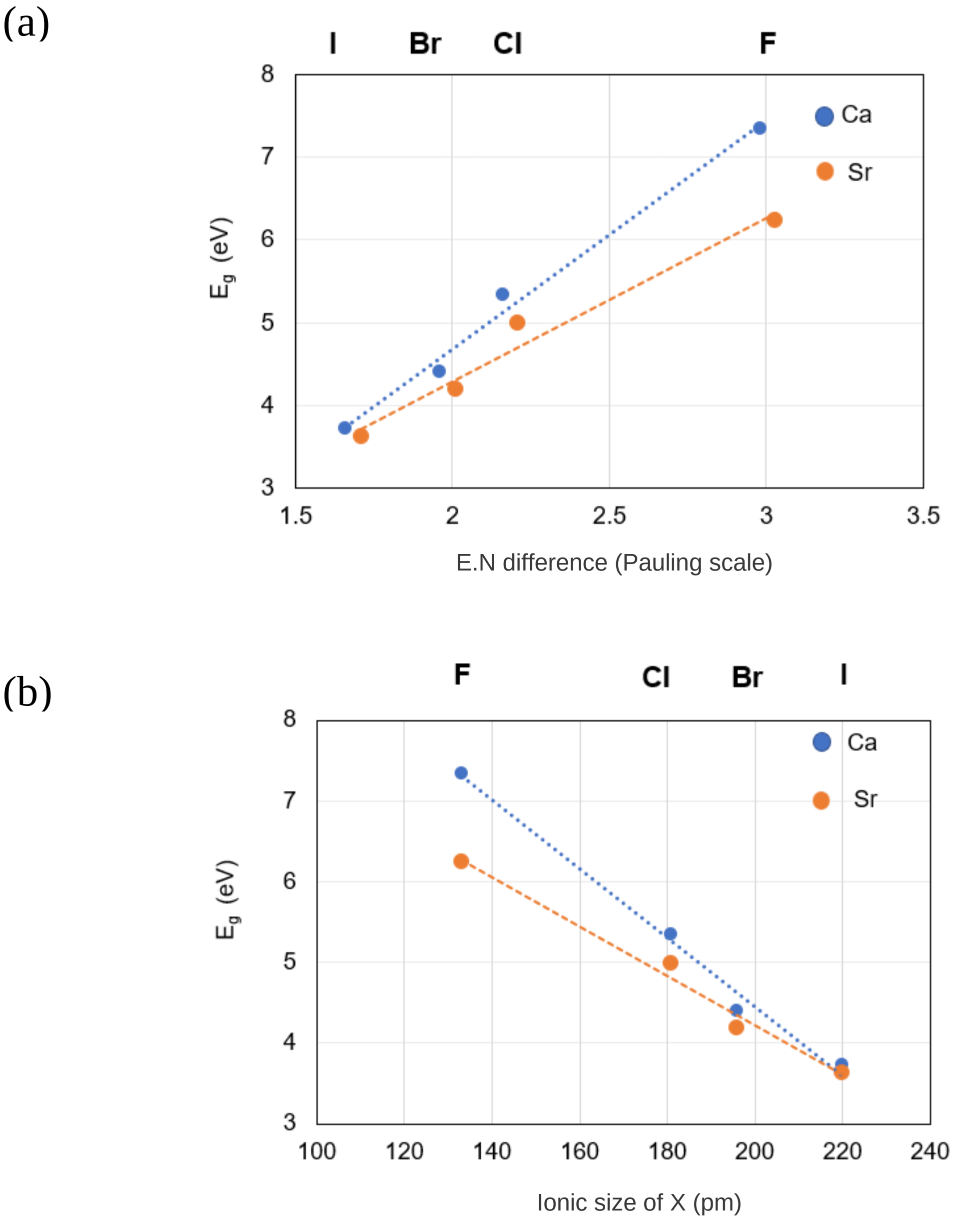

Figure 4.1 Dependence of bandgap on (a) E.N. difference and (b) Ionic size of X for bulk $CsBX_3$ bulk structures.

The covalency of a bond can primarily determine by the E.N difference between atoms taking part in the bond. When set of similar or different elements come close and form crystal orientation of atoms as well as their co-ordination comes into play in the orbital interaction leading to change in the bonding properties. So, here we adapted the concept of Shannon radius to analyze the covalency between B-X bonds. Shannon explained and calculates the size of different ion based on their oxidation states and coordination number [149]. Basically, the Shannon bond distance (D_{Sh}) between any two ions is the sum of their Shannon radii. For example, the Cs-I bond in the $CsCaI_3$ structure has a bond-length of 3.2 Å where Shannon radius for Ca^{2+} and I^- is 1 Å and 2.2 Å respectively. The measured bond-distance between Ca-I is 3.11 Å. The decrease in the bond-distance from the D_{Sh} i.e. ($D_{Sh} – D_{Obs}$) considered as the measure of covalency of the bond [150]. Bonds with higher value of ($D_{Sh} – D_{Obs}$) means the higher covalency of the bond. Although the E.N difference between atoms participating in a bond primarily determines the covalency in the ideal case and also D_{Sh}-D_{Obs} parameter correlates well with the E.N difference [150] the covalency of a bond in real solid deviates from its ideal nature (governs by only E.N difference). Hence, in order to determine the B-X bond dependent bandgaps in these perovskites both D_{Sh}-D_{Obs} and E.N difference between B and X should be considered. For all the $CsBX_3$ composition the difference D_{Sh}-D_{Obs} is maximum for the compounds with I and F. But the Cl and Br show a lower value compared to I and F. For example, the D_{Sh}-D_{Obs} for Ca-I, Ca-Br, Ca-Cl and Ca-F for the $CsCaX_3$ systems are 0.09, 0.08, 0.08 and 0.09 respectively (Fig 4.2). Therefore, the covalency increased is maximum for both Ca-F and Ca-I in $CsCaI_3$ and $CsCaF_3$. The deviation of the Ca-Br and Ca-Cl systems in the Fig. 4.1 (a) due to the lower D_{Sh}-D_{Obs} or the lower covalency of Ca-Br and Ca-Cl bonds in the $CsCaBr_3$ and $CsCaCl_3$ perovskites respectively. The D_{Sh}-D_{Obs} parameter is very useful to compare between bonds where the electronegativity of the atoms is very close. In $CsBX_3$ compounds, from Ca to Sr, the electronegativity of the B changes very little from 1.0 in Ca to 0.95 in Sr in Pauling's scale. Although the change in E.N is not significant, the bandgaps for Sr-compounds are lower than the Ca-compounds, Table 4.1 (e.g. $CsCaBr_3$: 4.4 eV and $CsSrBr_3$: 4.19 eV). This observation can be explained by comparing the D_{Sh}-D_{Obs} for Ca and Sr systems. The D_{Sh}-D_{Obs} parameters for all Sr-X bonds are higher than the Ca-X bonds which shows an enhanced covalency and the lowered bandgap in $CsSrX_3$ compounds compared to $CsCaX_3$. Also, the larger size of Sr (118 pm) compared to Ca (100 pm) eases the sharing of the electrons with X, which results in greater covalency in Sr-X bonds.

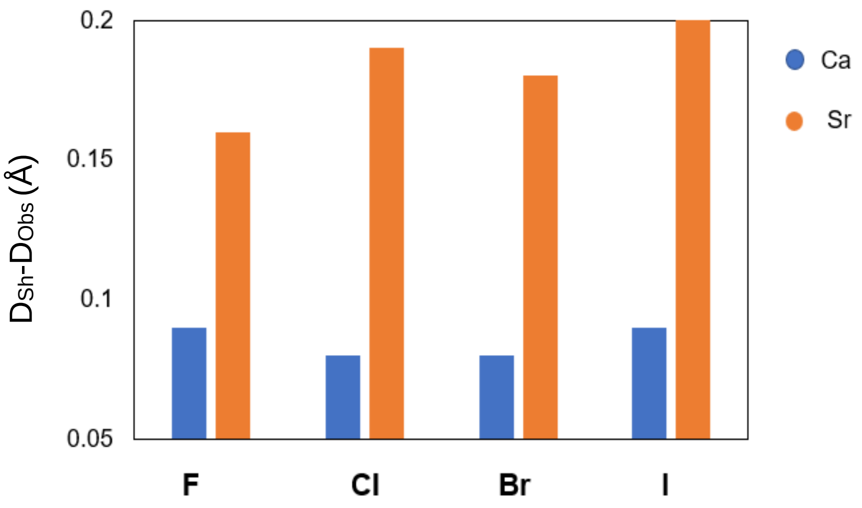

Figure 4.2 D_{Sh}-D_{Obs} for the bulk $CsBX_3$ structures. The Shannon radii for the B and X taken from [149].

4.3.2 Surface models: structural and electronic properties

For our calculations, we considered the two different surface terminations (Fig 4.3). In all CsX terminations, the first layer consists of Cs^+ and X^- and the second layer contains B^{2+} and two X^-. But for the BX_2 terminations, the first layer comprised of B^{2+} and two X, and the second layer has Cs^+ and X^-. The surfaces are different compared to the bulk due to the larger free volume available to the atoms at the surface compared to bulk. Hence, surface atoms undergo surface reconstruction leading to change in the structural (bond angles, bond distances) from their corresponding bulk values. Both the CsX and BX_2 terminations have different structural properties compared to the bulk $CsBX_3$. For example, the bulk structures of $CsBX_3$ have all equal B-X bond distance (symmetric) and 180^0 B-X-B bond angle. The B-X bond-lengths become asymmetric (apical and axial B-X bond-lengths are different), and the B-X-B bond angle decreases from 180^0 in both the terminations.

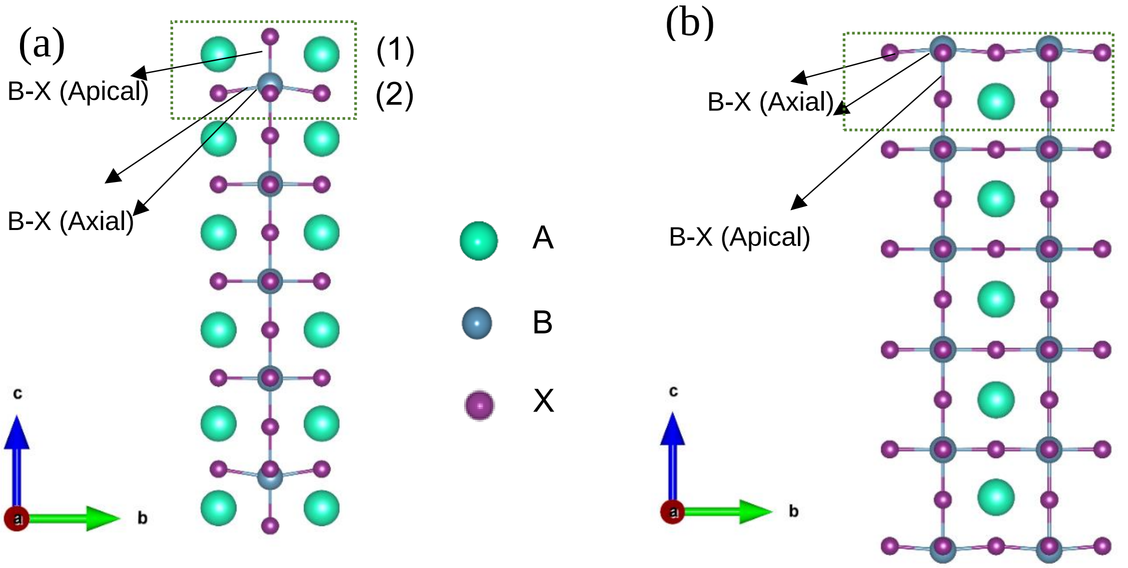

Figure 4.3 The (001) surface with 11 layers thickness for (a) CsX and (b) BX_2 termination. The atoms inside the rectangle in (a) and (b) are considered as the surface atoms for the two terminations. (1) and (2) represent the layer-1 and layer-2 respectively.

The structural changes on the surfaces occur due to the breakage of some B-X bonds on the surface. The bulk periodicity is broken on the top and bottom layers of the surface. The atoms on the topmost layers of surfaces lack the neighboring atom compared to bulk and hence surface atoms suffered greater non-compensated attractions from the inner layer and the top and bottom-most layer relaxed inward. This non-compensated attraction along the *c* direction causes one B-X bond (apical) to become shorter compared to other B-X bonds (axial) and the average B-X bond distance reduced compared to the bulk B-X bond distance. For a fixed B, among all X the average B-X bond distances increase from F to I, same as the bulk. For example, the average B-X (Ca-F) bond length decreases from bulk in the $CsCaF_3$ are 0.44% and 1.33% for CsX and BX_2 terminations, respectively (Table 4.2). Whereas, in $CsCaI_3$ the average Ca-I bond length decreased from the bulk to 2.25% and 2.89% lower values in CsI and CaI_2 terminations respectively. Comparing both the CsX and BX_2 terminations, the change (decrease) of average B-X distance is more in BX_2 termination than the CsX. For instance, average B-X bond distance change from the bulk $CsCaBr_3$ in CsBr terminated surface is 2.08%, and for $CaBr_2$ termination, the change is 3.12% (Table 421). The greater decrease in the average bond-lengths in BX_2 compared to CsX is mainly due to the structural difference between them on the top two layers. The axial B-X bond distances are longer than the apical B-X bond. Also, the apical B-X bond-distances in the BX_2 decreases more from bulk compared to the apical B-X bond-distance in CsX, which explain the greater decrease in B-X average bond-distances in BX_2. The bandgaps of perovskites can be explained by the bond-distances of B-X. Longer B-X bonds produce smaller bandgaps in perovskites. In longer bond the electron charge cloud dispersed throughout the bond and hence sharing of the electrons is favorable. So, longer bond shows more covalency than a shorter bond [53].

Table 4.2 The average B-X bond distance in Å and B-X-B bond angle in degrees for all the surfaces.

System	**Bulk**		**CsX**		**BX_2**	
	B-X	B-X-B	B-X	B-X-B	B-X	B-X-B
$CsCaF_3$	2.24	180	2.23	173.84	2.21	178.80
$CsCaCl_3$	2.73	180	2.67	168.74	2.65	178.96
$CsCaBr_3$	2.88	180	2.82	165.72	2.79	175.30
$CsCaI_3$	3.11	180	3.04	162.24	3.03	171.57
$CsSrF_3$	2.36	180	2.35	169.12	2.32	173.71
$CsSrCl_3$	2.86	180	2.80	163.55	2.78	172.96
$CsSrBr_3$	3.01	180	2.96	159.98	2.94	169.16
$CsSrI_3$	3.23	180	3.18	156.15	3.16	164.68

Although the bond-distance change is not very significant but considering the intrinsic ionic nature of the B-X bond in all *s*-block perovskite, this small change can help to compare the small changes in surface bandgaps from the bulk values in table 4.1. The B-X average bond distance as well as the B-X-B bond angles usually decreases (distortion) from F to I, due to the increasing size of the X (Table 4.2). Higher sized X atoms distort the B-X-B bonds with a higher extent. The only exception is Ca-Cl-Ca bond angle (178.80^0) decrease slightly less compared to the Ca-F-Ca bond angle (178.96^0) in BX_2 termination (Table 4.2). Although the ionic size of Cl (181 pm) is greater compared to F (133 pm), the bond angle changed more in F-system. This can be explained by comparing the axial Ca-F bond-length to the Ca-Cl axial bond. For all CaX_2 termination except CaF_2, the axial Ca-X bond-distance remains the same as the bulk and the apical bond lengths become shorter. But in CaF_2 the Ca-F axial bond length changed from 2.24

Å in bulk to 2.29 Å in CaF_2. This elongated bond-length (axial) in CaF_2 leads to a greater decrease in the bond angle compared to $CaCl_2$.

The bandgaps of the surfaces are closely linked with the intrinsic properties of B and X like the bulk. But the bandgap change from the bulk can be explained in terms of structural change on surfaces with respect to bulk. So, here also we used the same parameter such as E.N difference, size of X and covalency to describe the bandgap variation with B and X. The covalency of B-X bonds on the surfaces not only depends on chemical properties of B and X, but also on the structural properties such as B-X-B bond angle. The bandgaps of the surfaces are closely linked with the intrinsic properties of B and X as observed in the case of bulk. But the bandgap change from the bulk can be explained in terms of structural change on surfaces with respect to bulk. So, here also we used the same parameter such as E.N difference, size of X and covalency to describe the bandgap variation with B and X. The covalency of B-X bonds on the surfaces not only depends on chemical properties of B and X, but also on the structural properties such as B-X-B bond angle.

The bandgaps for all CsX and BX_2 terminations for Ca and Sr systems are narrow compared to the bulk. The Pb-based perovskite systems have also shown a changed bandgap values on the surfaces. For instance, the bandgap 1.6 eV in bulk tetragonal $MAPbI_3$ changes to 1.69 eV in MAI and 1.4 eV in PbI_2 termination respectively [151]. For all the surfaces here has shown an elongated B-X axial bond length and hence a greater covalency in all the surfaces compared to the bulk. The increased covalency in surface structures can be quantified by the same parameter D_{Sh}-D_{Obs}. Fig. 4.4 represents the D_{Sh}-D_{Obs} parameter for all $CsCaX_3$ surfaces compared with bulk. Note that, all the B-X bonds are not equal on the surfaces and for simplicity we considered the average B-X bond distances. The D_{Sh}-D_{Obs} for all the surfaces is greater than the bulk values, which is a definite indication of increased covalency of B-X bonds on the surfaces. Also, the CaX_2 shows a greater D_{Sh}-D_{Obs} than the CsX termination. So, the CaX_2 surface is more covalent compared to the CsX.

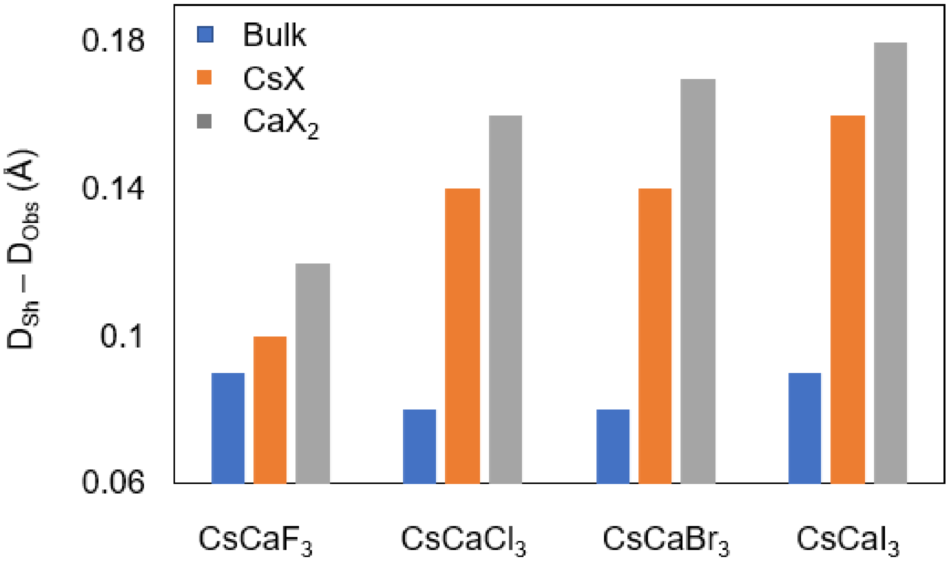

Fig. 4.4 D_{Sh}-D_{Obs} for all $CsCaX_3$ bulk structure and all CsX and CaX_2 surfaces.

As mentioned earlier, the covalency of B-X bond is linked with the bandgap and the greater covalency of the B-X bond results in narrower bandgaps. The table 4.1 also represents the bandgaps for the all the $CsBX_3$ surfaces along with the corresponding bulk bandgap values. All the BX_2 terminations show lower bandgap values compared to the CsX value except CsI-terminated surface in $CsCaI_3$ shows a lower bandgap (3.42 eV) compared to the CaI_2 termination (3.48 eV) which we have explained later in the discussion. The reason for BX_2-terminated surface having a lower band gap can be explained primarily from figure 4.4, which shows the BX_2 surfaces having greater covalency compared to the CsX-terminated surfaces. The greater covalency of the B-X bonds in BX_2 results in lowering the bandgap than the BX_2 surfaces.

The greater covalency of the BX_2 over CsX can also be explained by considering the effective charges on the surface atoms. The effective atomic charge of an atom is the net charge experienced by the valance electrons. The effective atomic charge is less than the actual formal charge due to the various factor such as screening effect of the inner atomic orbitals or the change in bond length or bond angle. Due to the structural changes on the surfaces the atomic charge gets redistributed and as a result of that all the surface atoms show different effective atomic charges. The effective atomic charges of all the CaX_2 and CsX surface atoms are listed in Table 4.3. The formal charge for the Cs atom is +1e whereas for Ca and all X atoms have a formal charge of +2e and -1e respectively. Note that the effective atomic charges of both Ca and X for both the CaX_2 and CsX terminations are much smaller to their formal charges, same as the bulk. The Ca and I atomic charges show a maximum decrease from their formal charges in bulk. The Ca and F shows the minimum decrease. So, the covalency decreases from Ca-I to Ca-F bonds gradually. This changes of atomic charges of Ca-X are more profound in both the CsX and CaX_2 terminated surfaces. In CaX_2 termination, the Ca atoms on the topmost layers gained charge compared to the bulk Ca atoms whereas the X atoms on the CaX_2 surfaces show a greater decrease in the effective atomic charges compared to the bulk. Again, in CsX terminations the Ca (2) in the second layer shows a decrease of charge from the bulk value and but the X atoms on the second layer doesn’t show any significant change from the bulk. All the surface atoms show a greater decrease in the atomic charges (more sharing of charge) compared to the bulk and hence higher covalency of Ca-X bonds on the surfaces. This can also explain the covalency we discussed in terms of D_{Sh}-D_{Obs} (fig 4.4) for all the surfaces and thus the surfaces have lower bandgaps than the bulk structures. Table 4.3 The calculated effective atomic charges (in e) for all the surface atoms in CsX and BX_2

Table 4.3 The calculated effective atomic charges (in e) for all the surface atoms in CsX and BX_2 surfaces.

CsX	**Cs (1)**	**X (1)**	**Ca (2)**	**X (2)**
F	0.85(-0.01)	-0.79 (-0.03)	1.40 (-0.02)	-0.76 (0)
Cl	0.83 (-0.02)	-0.76 (-0.03)	1.31 (-0.04)	-0.73 (0)
Br	0.81 (-0.03)	-0.74 (-0.02)	1.26 (-0.05)	-0.71 (0)
I	0.80 (-0.03)	-0.71 (-0.02)	1.19 (-0.06)	-0.69 (0)
BX_2	**Ca (1)**	**X (1)**	**Cs (2)**	**X (2)**
F	1.48 (+0.06)	-0.76 (0)	0.85 (-0.01)	-0.75 (+0.01)
Cl	1.39 (+0.04)	-0.72 (+0.01)	0.84 (-0.01)	-0.71 (+0.02)
Br	1.34 (+0.03)	-0.71 (+0.01)	0.83 (-0.01)	-0.68 (+0.04)
I	1.26 (+0.01)	-0.68 (+0.02)	0.830 (0)	-0.64 (+0.06)

The numbers in brackets are difference from the bulk values. Bulk charges; $CsCaF_3$(e): Cs = 0.86, Ca=1.42, F= - 0.76, $CsCaCl_3$(e): Cs = 0.85, Ca=1.35, Cl= - 0.73, $CsCaBr_3$(e): Cs = 0.84, Ca=1.31, Br= - 0.71, $CsCaI_3$(e): Cs = 0.83, Ca=1.42, I= - 0.70. (1) and (2) signifies the layer number from the top.

To understand the effect of surfaces on the electronic structure we plotted the density of states of all the surfaces with different chemical composition. Fig 4.5 (a)-(h) represents the density of states for all the CsX and CaX_2 surfaces.

(a)

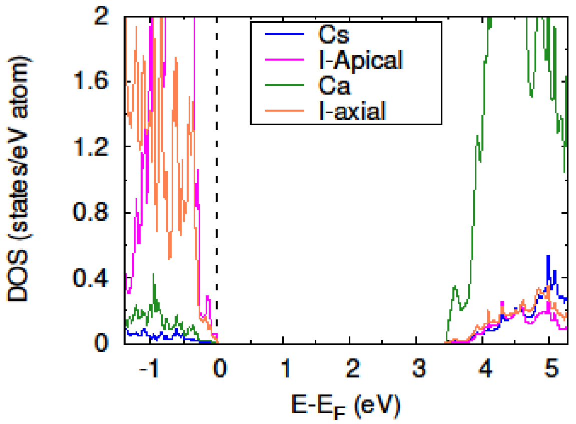
DOS (states/eV atom)
E-E$_F$ (eV)
Cs
I-Apical
Ca
I-axial
0
0.4
0.8
1.2
1.6
2
-1
0
1
2
3
4
5

(b)

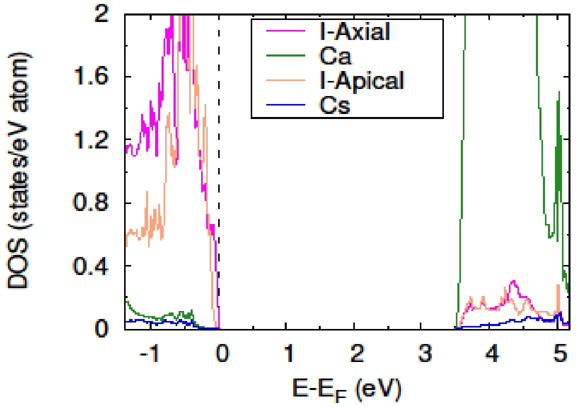
DOS (states/eV atom)
E-E$_F$ (eV)
I-Axial
Ca
I-Apical
Cs
0
0.4
0.8
1.2
1.6
2
-1
0
1
2
3
4
5

(c)

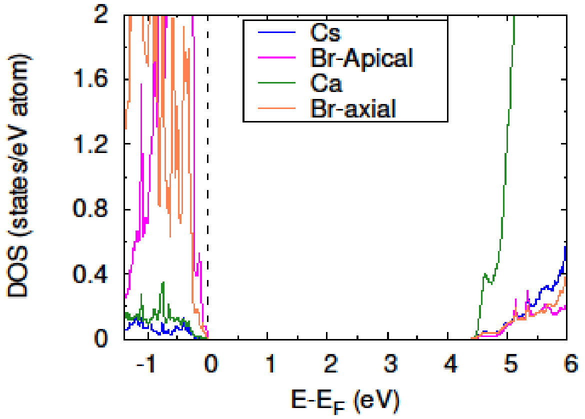
DOS (states/eV atom)
E-E$_F$ (eV)
Cs
Br-Apical
Ca
Br-axial
0
0.4
0.8
1.2
1.6
2
-1
0
1
2
3
4
5
6

(d)

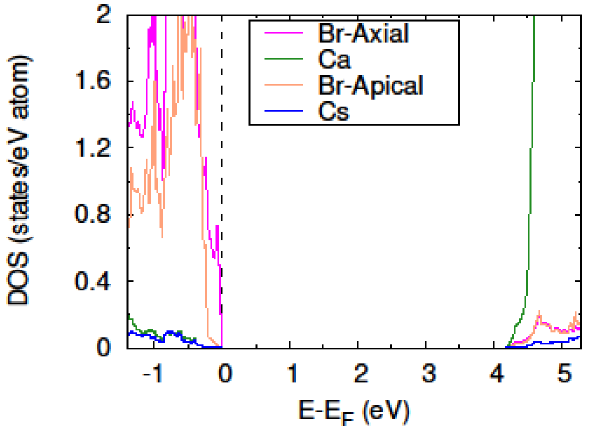
DOS (states/eV atom)
E-E$_F$ (eV)
Br-Axial
Ca
Br-Apical
Cs
0
0.4
0.8
1.2
1.6
2
-1
0
1
2
3
4
5

(e)

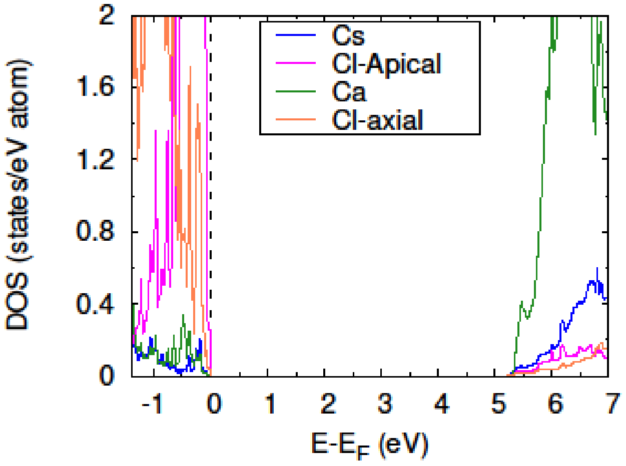
2
1.6
1.2
0.8
0.4
0
DOS (states/eV atom)
-1
0
1
2
3
4
5
6
7
E-E$_F$ (eV)
Cs
Cl-Apical
Ca
Cl-axial

(f)

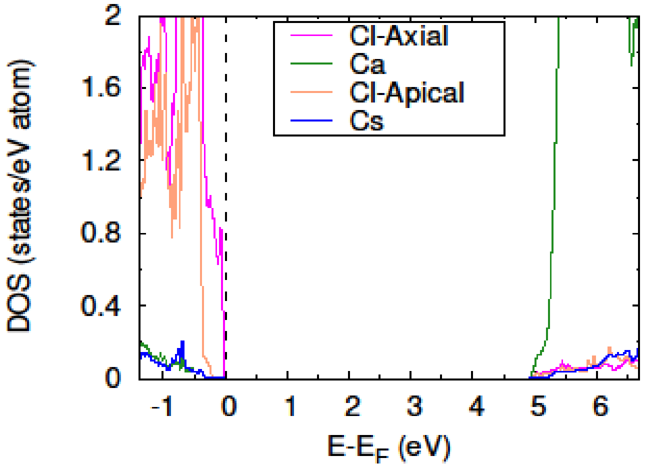
2
1.6
1.2
0.8
0.4
0
DOS (states/eV atom)
-1
0
1
2
3
4
5
6
E-E$_F$ (eV)
Cl-Axial
Ca
Cl-Apical
Cs

(g)

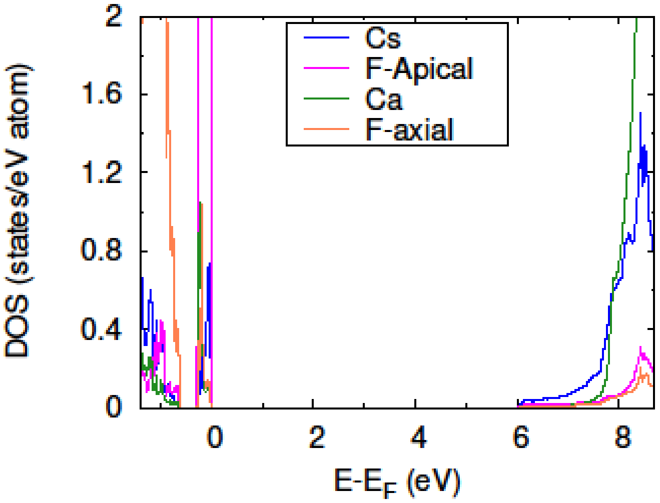
2
1.6
1.2
0.8
0.4
0
DOS (states/eV atom)
0
2
4
6
8
E-E$_F$ (eV)
Cs
F-Apical
Ca
F-axial

(h)

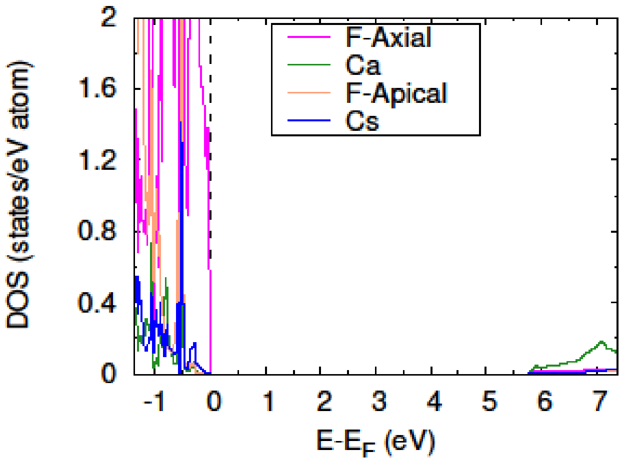

Figure 4.5 The density of states plot for (a) CsI, (b) CaI_2, (c) CsBr, (d) $CaBr_2$, (e) CsCl, (f) $CaCl_2$, (g) CsF and (h) CaF_2 surfaces of $CsCaX_3$

The bandgap is determined by the positions of the VBM and CBM. Thus, the atoms (or orbitals) contributing to the VBM and CBM have a significant impact in determining the bandgaps. The bandgaps or the positions of VBM and CBM for all the surfaces are different than the bulk. Although the atoms or orbitals contributing at the VBM and CBM remains same as bulk, the position of VBM and CBM and hence the bandgap changes due to different bonding nature of B-X bonds in the surfaces. For all the CsX and BX_2 terminated surface, the VBM is made up of the p-orbitals of the X atoms, and CBM mainly consists of nd orbitals of B with contribution from X and Cs as well. For example, in CsI and CaI_2 surfaces the VBM comes from the 5p orbitals of I and 3d orbital of Ca contributes majorly at the CBM (fig 4.5 (a) and (b)). Hence, the nature of VBM and CBM for the surfaces are like the bulk structure. The only difference is for the surfaces at the CBM we observed a relatively greater contribution from B-X hybrid orbital. In CsX and BX_2 terminated surfaces it is observed that at the VBM both the X atoms (apical as well as the axial) contributes equally for CsX termination, whereas in BX_2

termination the contribution comes majorly from the axial X atoms. So, considering the average B-X bond distance to explain the observations might not be appropriate. So, from here onwards, we will consider the axial B-X bond distance for explaining the observations. The nature of the CBM among two terminations are not significantly different. For the BX_2 termination at the CBM the major contribution comes from n*d* orbitals, but the due to increase in the covalency of B-X bonds from F to I, hybrid states of B and X atoms are found at the CBM. The contribution from the Cs 5*s* states is very negligible at the CBM for the BX_2 terminations whereas for the CsX termination the presence of Cs 5*s* states is visible. For the CsX terminations, at the CBM the hybrid states of Cs 5*s* and X n*s* and n*p* are observed with a major contribution from Cs 5*s* state (Figure 4.5 (g)). The contributions of Cs are only observed in CsF and CsCl termination, but the CBM of CsBr and CsI do not show any significant contribution from Cs. The smaller size and higher electronegativity of the Cl and F atoms facilities the stronger ionic interaction between Cs and F or Cl which causes the Cs states to appear on the CBM of CsF and CsCl surfaces. The bond dissociation energy (BDE) of Cs-F (517 kJ/mol) and Ca-F (527 kJ/mol) are very close, and due to this Cs states appear majorly over Ca on the CBM. Due to presence of Cs states along with Ca and F hybrid states (see figure 4.6 (a)) the energy level of CBM gets lowered and narrowed the bandgap by 0.845 eV in CsF compared to the bulk $CsCaF_3$. Another noticeable feature of CsF density of states plot is formation of the surface states at the 0.31 eV above the VBM (Figure. 4.5 (g)). The surface state originated from the antibonding interaction between Cs, Ca, and F (See figure 4.6 (b)).

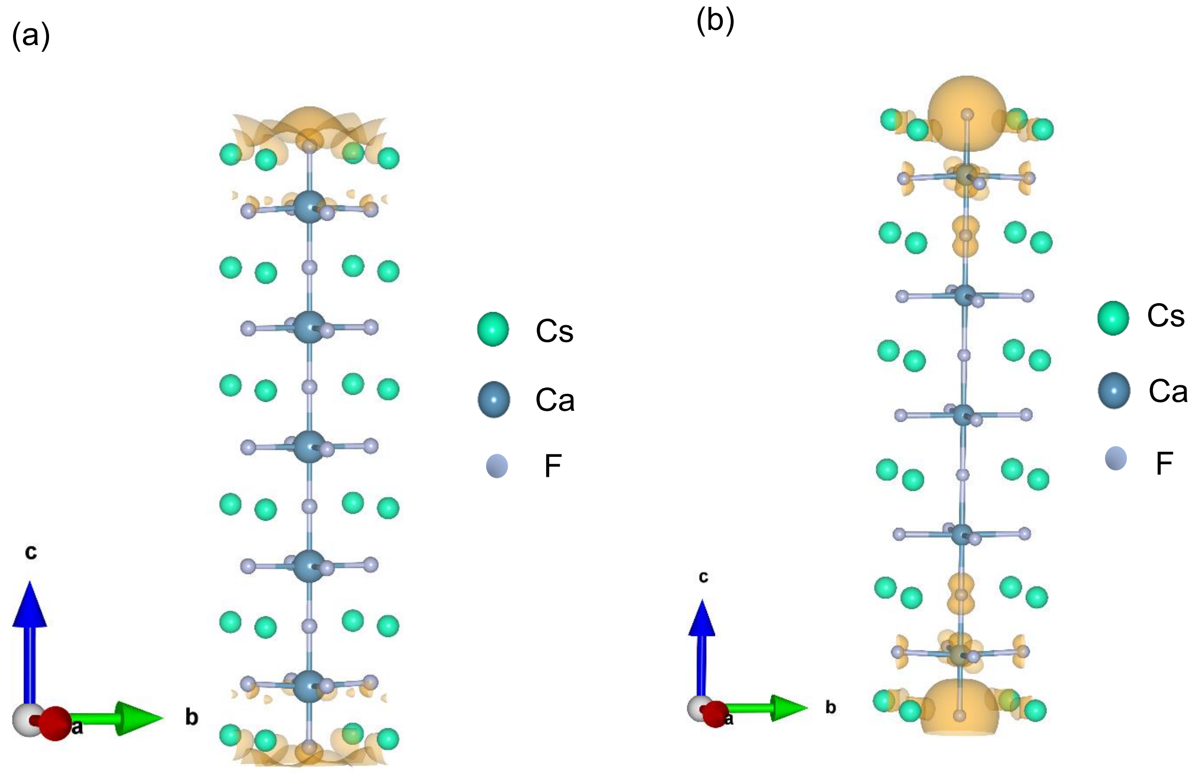

Figure 4.6 The isosurface plot of electron charge density of the CsF termination at (a) CBM (~0.05 eV inside the conduction band from CBM) and (b) at the energy range 0.3-0.35 eV on the bandgap. Both the isosurface plots correspond to the fig. 4.5 (g)

The antibonding interaction between Cs, Ca, and F atoms creates a state with much higher energy than the F 2*p* states (VBM) and hence formed a localized surface state in CsF (fig. 4.5 (g)). A similar nature of the band structure i.e. the formation of surface states and the major contribution of Cs atom at the CBM is also observed in CsF termination of $CsSrF_3$. Bandgaps of all the surfaces along different B and X composition depends on the intrinsic property of the surface atoms as well as on the structural changes on the surfaces from the bulk. Hence, we linked all the surface bandgaps with the E.N difference, ionic size of X and axial B-X bond length. like bulk. Figure 4.7 represents the dependencies of surface bandgaps on the factors we have mentioned before.

(a)

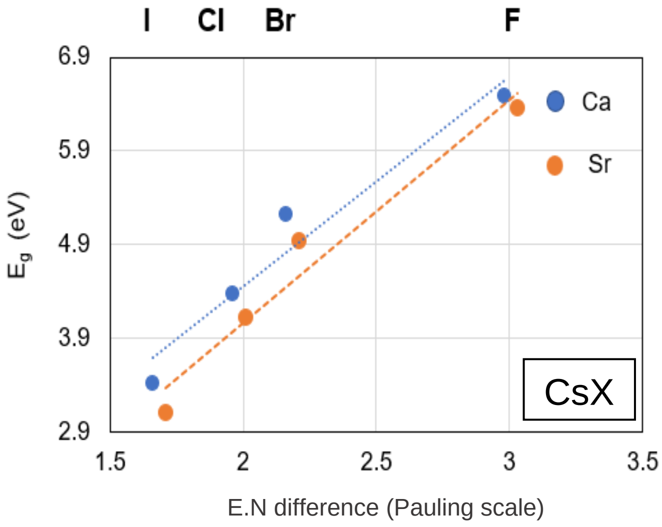

(b)

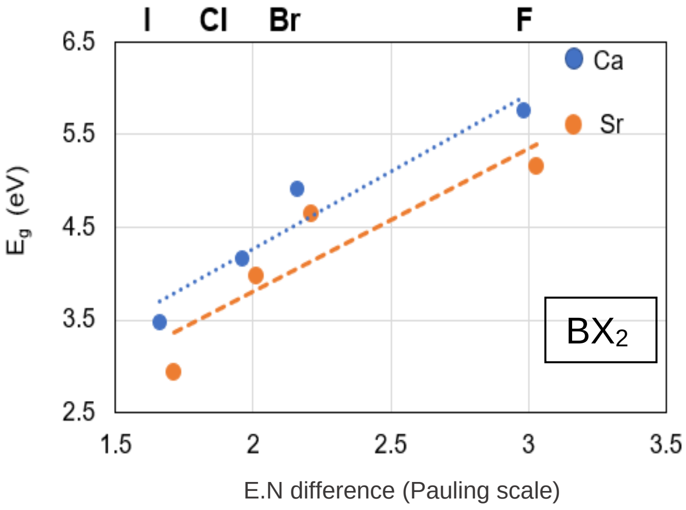

(c)

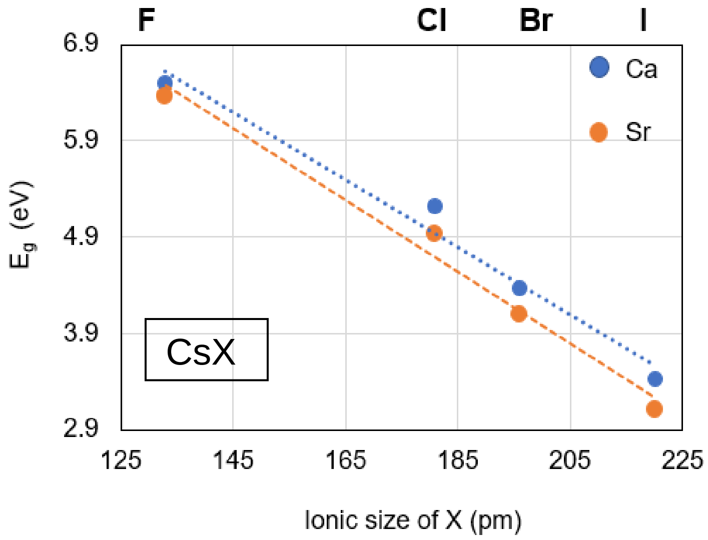

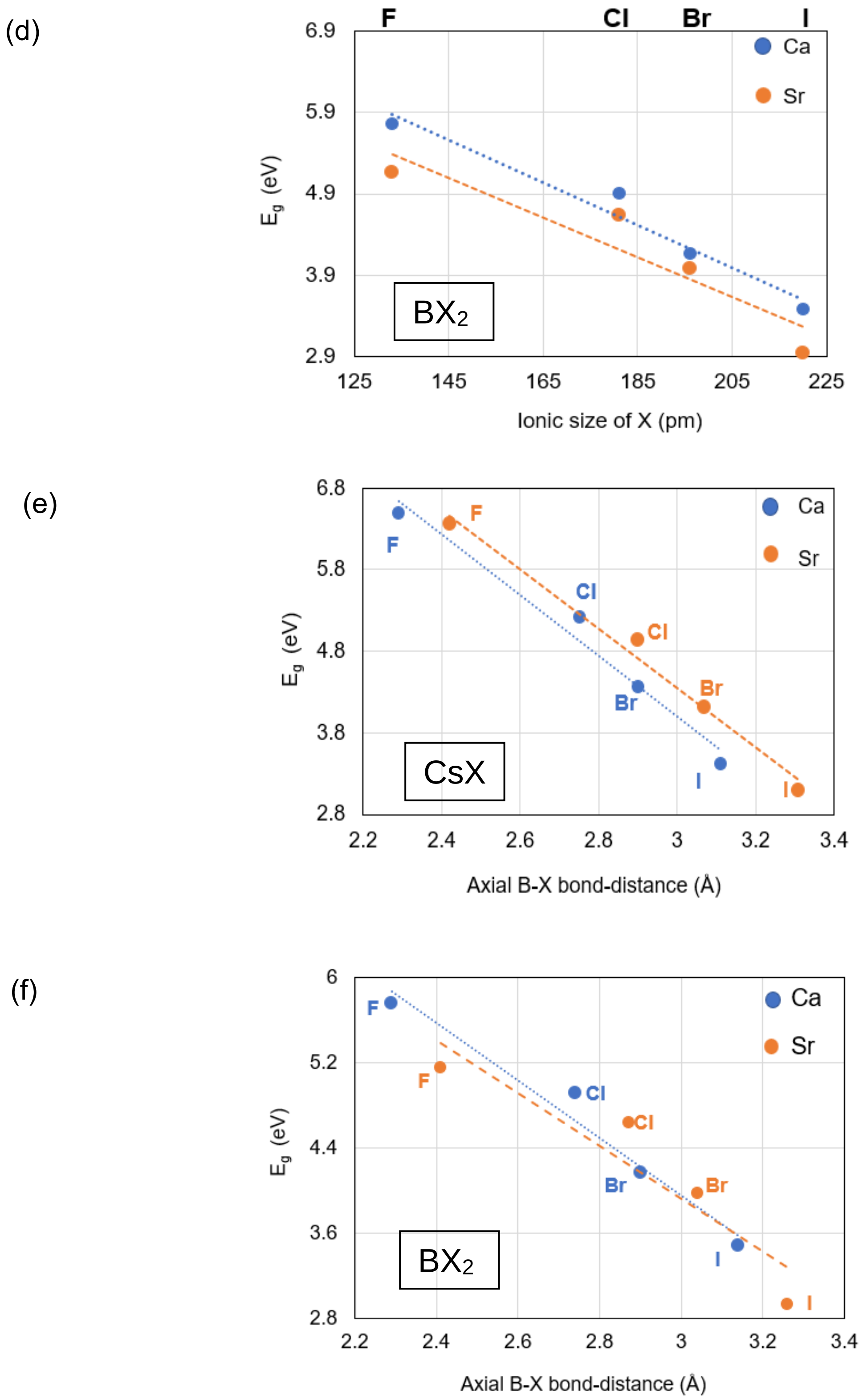

Figure 4.7 Bandgaps as a function of E.N difference, ionic size of X and axial B-X bond-distance for all (a), (c), (e) CsX and (b), (d), (f) BX_2 terminations respectively.

Although the bandgaps of all the surfaces shows a gradual change along the B and X intrinsic properties but we are unable to find a systematic change in the bandgaps (compared to the bulk bandgaps) with changing composition of B and X. The change in the bandgaps on the surfaces can be explained as the combined effect of both intrinsic properties of surface atoms and the structural reorientation on the surface. To understand the effect of structural changes on the bandgaps we further extended our analysis and considered the factors such as apical and axial bond length changes and distortion of B-X-B bond angle. The B-X-B bond angles can affect the bandgap by affecting the bonding interaction between them. The deviation of the B-X-B bond angle from 180^0 can significantly reduce the covalency of the B-X bond [66], and hence the bandgap increased. The amount of deviation of B-X-B angle among all CsX surfaces increased from F (~6.16^0), Cl (~11.26^0), Br (~14.28^0) to I (~17.76^0) with the increase in the size of X atoms (See table 4.1). Again in the CsX terminations (for all $CsCaX_3$) the axial B-X bond length changes are as follows- CsF (2.54%), CsCl (1.4%), CsBr (1.99%) and CsI (2.47%) and the corresponding bandgap changes are 0.12 eV in CsF, 0.05 eV in CsCl, 0.08 in CsBr and 0.525 eV in CsI, respectively. Although these changes are very small, but the changes can be useful to explain the bandgap changes in surfaces compared to bulk. The bandgap change is less for all $CsSrX_3$ surfaces than the $CsCaF_3$ surfaces due to the larger deviation of the B-X-B bond angles in Sr. One exception is- in the same CsCl terminated surface in Ca and Sr, the B-Cl bond-length change is more in Sr-Cl (1.4%) than the Ca-Cl (0.73 %), but the bandgap change from the bulk is less for Sr (0.08 eV) compared to Ca (0.118 eV). This observation is due to the decrease in covalency of Sr-Cl bonds due to the larger tilt in Sr-Cl-Sr bond angle (~16.45^0) than the Ca-Cl-Ca bond angle (~11.26^0). The bandgaps of all the BX_2 terminated surfaces are lower than the CsX which is already discussed before in terms of the Shannon radii. Also, all the BX_2

terminations have a less distorted bond angle (~1.02^0-4.5^0) compared to the CsX surfaces (~ 6.16^0-17.76^0) which further explains the higher covalency and lower bandgaps in BX_2 surfaces than the CsX. The only exception is that the CsI surface have a lower bandgap than CaI_2 which can be explained by considering the Ca-I axial bond length change from the bulk in both the terminations. For CaI_2 terminated surface the Ca-I distance change is around 0.36% compared to 0.96% in the CsI termination while the apical Ca-I bond distance remains the same in both the terminations. The greater change in the axial Ca-I bond-length decreased the bandgap in CsI more in comparison to CaI_2 surface. Bandgaps for all the BX_2 terminated surface shows a systematic change with the size, B-X bond length, and E.N difference but the change from the bulk bandgap is not systematic as observed in the CsX terminations.

Conclusion:

We have studied a series of (001) *s*-block perovskite surfaces and compare their structural and electronic property (bandgap) with the corresponding bulk structure. All the bulk bandgap shows an orderly change with respect to the intrinsic properties such as atomic size and electronegativity difference between the metal and the halogen. The bulk bandgaps increase from iodine to fluorine and all the Sr-based compound show a lower bandgap compared to the Ca systems. The surface bandgap depends both on the intrinsic properties of the surface atoms and the structural features of the surface. Between two terminations CsX is more ionic than BX_2 terminations and BX_2 bandgaps are usually lower than the CsX bandgaps. The bandgaps for all the surfaces show a systematic change along different composition of metal and halogen similar to the bulk. The formation of surface states is only observed in CsF surfaces for both Ca and Sr. The change in bandgaps compared to the bulk structures are explained considering the structural parameter such as bond angle and bond-distance between metal and halogen.

Chapter 5: Conclusion, Limitations and Future Work

Conclusion:

In this work, we systematically examined the electronic structure of bulk and (001) surfaces of the *s*-block halide perovskite ($CsBX_3$). We also studied the effect of antisite defect on the electronic structure of bulk perovskite. We found that-

(i) The bandgap for these compounds significantly depends upon the chemical composition of metals (Ca, Sr, Ba) and halogens (F, Cl, Br, I). For a fixed metal composition, bandgaps for the bulk decrease from F, Cl, Br to I. Again, from Ca, Sr to Ba the bandgap decreases gradually with a fixed halogen composition.

(ii) The systematic change in the bulk bandgaps along the compositions of B and X is closely related to the covalency of the bond between B metal and halogen X and hence, bulk bandgaps are successfully linked with the intrinsic properties of B and X such as- electronegativity of B and X, size (Atomic and Shannon radius) of B and X.

(iii) The bandgaps for bulk cubic structures are different than the bulk orthorohmbic structures for the same perovskites. This is due to the different B-X bond distances and B-X-B bond angles in both the structures.

(iv) We have also studied the effect of antisite defect on the electronic structures of these *s*-block perovskites. We have observed that the position of the defect state on the bandgap can be tuned by changing the compositions of metal and halogen. Also, the formation of defect states on the band gap in presence of antisite defect greatly reliant on the crystal structure of the perovskite. Further we have shown the intrinsic properties of metal and halogen plays a crucial role in tuning with the position of the defect state on the bandgap.

(v) The (001) surfaces of Ca and Sr systems shows the similar trend of bandgap change with the composition of metals and halogens. The bandgap changes in the bulk and the surfaces with respect to the composition was mainly due to the changing covalency of metal-halogen bonds on the surfaces. Based on that, we draw a connection between the intrinsic properties of the metal and halogen such as- atomic or ionic sizes, electronegativities of metal and halogen with the surface bandgaps.

(vi) The bandgaps for the surfaces are not only reliant on the chemical composition of metal and halogen but also the structural factors such as the bond angle and bond-distance changes from the bulk. Hence, based on the intrinsic properties of metal and halogen, one can tune the bandgap and can achieve the desired electronic properties.

Limitations and Future work

The structure and properties of a solid depend on the interactions between the electrons. The method we used the first principle electronic structure calculation is based on Density functional theory, which considers the electrons as a three-dimensional density function. The beauty of the theory is many-electrons systems are simplified into a single electron problem where each electron has an effective potential. For the past few decades, DFT has successfully predicted the structural (lattice structure) and electronic properties (bandgap, phonon spectra) of various solids. Walter Kohn, one of the authors of the DFT, has won a Nobel prize in Chemistry in 1998. Despite its successfully predicting the properties of solids, particularly the structure and thermodynamic property of solid there are few limitations in this theory, which sometimes results in the erroneous prediction of properties. The DFT calculations often underestimate the properties such as bandgap, the dissociation energies of molecules, etc. also, overestimates binding energies of some complexes. One of the main reasons behind the failure of the predictions is delocalization of the LDA or GGA exchange-correlation functions. The delocalization occurs when the Coulombic interaction term dominates the exchange-correlation function. Another drawback of the LDA and GGA approximation is it fails to explain the long-range van der Waals or dispersive interactions. Lastly, the DFT calculations are idealistic, i.e., they have formulated the zero-kelvin temperature and without any lattice vibration. This consideration significantly lacks realistic models of solid, and hence, there can be some difference in calculated and experimental values. Although the absolute band gap may change in real a perovskite, we expect the overall trend with change in chemistry will remain the same.

The future work will be to understand the defect properties of (001) perovskite surfaces which we are investigating currently. Furthermore, this study can be carried forward to the interface. It is very crucial to understand the electronic properties of these perovskites interfaced with different electron transporting layers for electronic device fabrication. The understanding of the interface properties of s-block perovskite can opens up a new possibility for these compounds to apply in various electronic applications with its excellent scintillation property.

Reference

1. "April 25, 1954: Bell Labs Demonstrates the First Practical Silicon Solar Cell". *APS News*. American Physical Society. **18** (4). April 2009.
2. Chapin, D. M., Fuller, C. S., & Pearson, G. L. (1954). A new silicon p-n junction photocell for converting solar radiation into electrical power. *Journal of Applied Physics*, *25*(5), 676-677.
3. Starr, C. (2005). Biology: Concepts and Applications. Thomson Brooks/Cole. ISBN 053446226X.
4. Shockley, W., & Queisser, H. J. (1961). Detailed balance limit of efficiency of p-n junction solar cells. *Journal of applied physics*, *32*(3), 510-519.
5. Reshi, H. A., & Zargar, R. A. (2018). Perovskite Solar Cells: The Challenging Issues for Stable Power Conversion Efficiency. In *Recent Development in Optoelectronic Devices*. IntechOpen.
6. Polman, A., Knight, M., Garnett, E. C., Ehrler, B., & Sinke, W. C. (2016). Photovoltaic materials: Present efficiencies and future challenges. *Science*, *352*(6283), aad4424.
7. Green, M. A. (2001). Third generation photovoltaics: Ultra-high conversion efficiency at low cost. *Progress in Photovoltaics: Research and Applications*, *9*(2), 123-135.
8. Goetzberger, A., Knobloch, J., & Voss, B. (1998). Crystalline silicon solar cells. *editorial John Wiley & Sons Ltd*, *1*.
9. Britt, J., & Ferekides, C. (1993). Thin-film CdS/CdTe solar cell with 15.8% efficiency. *Applied physics letters*, *62*(22), 2851-2852.

10. Xing, G., Mathews, N., Sun, S., Lim, S. S., Lam, Y. M., Grätzel, M., ... & Sum, T. C. (2013). Long-range balanced electron-and hole-transport lengths in organic-inorganic $CH_3NH_3PbI_3$. *Science*, *342*(6156), 344-347.

11. Stranks, S. D., Eperon, G. E., Grancini, G., Menelaou, C., Alcocer, M. J., Leijtens, T., ... & Snaith, H. J. (2013). Electron-hole diffusion lengths exceeding 1 micrometer in an organometal trihalide perovskite absorber. *Science*, *342*(6156), 341-344.

12. Liu, M., Johnston, M. B., & Snaith, H. J. (2013). Efficient planar heterojunction perovskite solar cells by vapour deposition. *Nature*, *501*(7467), 395.

13. De Wolf, S., Holovsky, J., Moon, S. J., Löper, P., Niesen, B., Ledinsky, M., ... & Ballif, C. (2014). Organometallic halide perovskites: sharp optical absorption edge and its relation to photovoltaic performance. *The journal of physical chemistry letters*, *5*(6), 1035-1039.

14. Brandt, R. E., Stevanović, V., Ginley, D. S., & Buonassisi, T. (2015). Identifying defect-tolerant semiconductors with high minority-carrier lifetimes: beyond hybrid lead halide perovskites. *Mrs Communications*, *5*(2), 265-275.

15. Kojima, A., Teshima, K., Shirai, Y., & Miyasaka, T. (2009). Organometal halide perovskites as visible-light sensitizers for photovoltaic cells. *Journal of the American Chemical Society*, *131*(17), 6050-6051.

16. Wilson, G., & Mooney, D. (2012). Research cell efficiency records. *National Center for Photovoltaics*.

17. Heremans, P., Cheyns, D., & Rand, B. P. (2009). Strategies for increasing the efficiency of heterojunction organic solar cells: material selection and device architecture. *Accounts of chemical research, 42*(11), 1740-1747.

18. Janssen, A. G. F., Riedl, T., Hamwi, S., Johannes, H. H., & Kowalsky, W. (2007). Highly efficient organic tandem solar cells using an improved connecting architecture. *Applied Physics Letters, 91*(7), 073519.

19. Li, S. S., Tu, K. H., Lin, C. C., Chen, C. W., & Chhowalla, M. (2010). Solution-processable graphene oxide as an efficient hole transport layer in polymer solar cells. *ACS nano*, *4*(6), 3169-3174.

20. Adachi, C., Baldo, M. A., Forrest, S. R., & Thompson, M. E. (2000). High-efficiency organic electrophosphorescent devices with tris (2-phenylpyridine) iridium doped into electron-transporting materials. *Applied Physics Letters*, *77*(6), 904-906.

21. Khan, A., Yamaguchi, M., Ohshita, Y., Dharmaraso, N., Araki, K., Khanh, V. T., ... & Matsuda, S. (2003). Strategies for improving radiation tolerance of Si space solar cells. *Solar energy materials and solar cells*, *75*(1-2), 271-276.

22. Willeke, G. P. (2002). Thin crystalline silicon solar cells. *Solar Energy Materials and Solar Cells*, *72*(1-4), 191-200.

23. Saliba, M., Matsui, T., Seo, J. Y., Domanski, K., Correa-Baena, J. P., Nazeeruddin, M. K., ... & Grätzel, M. (2016). Cesium-containing triple cation perovskite solar cells: improved stability, reproducibility and high efficiency. *Energy & environmental science*, *9*(6), 1989-1997.

24. McMeekin, D. P., Sadoughi, G., Rehman, W., Eperon, G. E., Saliba, M., Hörantner, M. T., ... & Johnston, M. B. (2016). A mixed-cation lead mixed-halide perovskite absorber for tandem solar cells. *Science*, *351*(6269), 151-155.

25. Veldhuis, S. A., Boix, P. P., Yantara, N., Li, M., Sum, T. C., Mathews, N., & Mhaisalkar, S. G. (2016). Perovskite materials for light-emitting diodes and lasers. Advanced materials, 28(32), 6804-6834

26. Travis, W., Glover, E. N. K., Bronstein, H., Scanlon, D. O., & Palgrave, R. G. (2016). On the application of the tolerance factor to inorganic and hybrid halide perovskites: a revised system. Chemical science, 7(7), 4548-4556

27. Amat, A., Mosconi, E., Ronca, E., Quarti, C., Umari, P., Nazeeruddin, M. K., ... & De Angelis, F. (2014). Cation-induced band-gap tuning in organohalide perovskites: interplay of spin–orbit coupling and octahedra tilting. *Nano letters*, *14*(6), 3608-3616.

28. Kieslich, G., Sun, S., & Cheetham, A. K. (2015). An extended tolerance factor approach for organic–inorganic perovskites. *Chemical science*, *6*(6), 3430-3433.

29. Kim, H. S., Im, S. H., & Park, N. G. (2014). Organolead halide perovskite: new horizons in solar cell research. *The Journal of Physical Chemistry C*, *118*(11), 5615-5625.

30. Manser, J. S., Christians, J. A., & Kamat, P. V. (2016). Intriguing optoelectronic properties of metal halide perovskites. *Chemical Reviews*, *116*(21), 12956-13008.

31. Fu, L., Zhang, Y., Chang, B., Li, B., Zhou, S., Zhang, L., & Yin, L. (2018). A fluorine-modulated bulk-phase heterojunction and tolerance factor for enhanced performance and structure stability of cesium lead halide perovskite solar cells. *Journal of Materials Chemistry A*, *6*(27), 13263-13270.

32. Lai, M., Kong, Q., Bischak, C. G., Yu, Y., Dou, L., Eaton, S. W., ... & Yang, P. (2017). Structural, optical, and electrical properties of phase-controlled cesium lead iodide nanowires. *Nano Research*, *10*(4), 1107-1114.

33. Mao, J., Sha, W. E., Zhang, H., Ren, X., Zhuang, J., Roy, V. A., ... & Choy, W. C. (2017). Novel direct nanopatterning approach to fabricate periodically nanostructured perovskite for optoelectronic applications. *Advanced Functional Materials*, *27*(10), 1606525.

34. Kim, Y. H., Cho, H., & Lee, T. W. (2016). Metal halide perovskite light emitters. *Proceedings of the National Academy of Sciences, 113*(42), 11694-11702.

35. Sutherland, B. R., & Sargent, E. H. (2016). Perovskite photonic sources. *Nature Photonics*, *10*(5), 295.

36. Stoeckel, M. A., Gobbi, M., Bonacchi, S., Liscio, F., Ferlauto, L., Orgiu, E., & Samorì, P. (2017). Reversible, fast, and wide-range oxygen sensor based on nanostructured organometal halide perovskite. *Advanced Materials*, *29*(38), 1702469.

37. Xia, H. R., Sun, W. T., & Peng, L. M. (2015). Hydrothermal synthesis of organometal halide perovskites for Li-ion batteries. *Chemical Communications, 51*(72), 13787-13790.

38. Endres, J., Egger, D. A., Kulbak, M., Kerner, R. A., Zhao, L., Silver, S. H., ... & Kahn, A. (2016). Valence and conduction band densities of states of metal halide perovskites: a combined experimental–theoretical study. *The journal of physical chemistry letters*, *7*(14), 2722-2729.

39. Ye, Y., Run, X., Hai-Tao, X., Feng, H., Fei, X., & Lin-Jun, W. (2015). Nature of the band gap of halide perovskites ABX_3 (A= CH_3NH_3, Cs; B= Sn, Pb; X= Cl, Br, I): First-principles calculations. *Chinese Physics B, 24*(11), 116302.

40. Brivio, F., Walker, A. B., & Walsh, A. (2013). Structural and electronic properties of hybrid perovskites for high-efficiency thin-film photovoltaics from first-principles. *Apl Materials*, *1*(4), 042111.

41. Lang, L., Yang, J. H., Liu, H. R., Xiang, H. J., & Gong, X. G. (2014). First-principles study on the electronic and optical properties of cubic ABX_3 halide perovskites. *Physics Letters A*, *378*(3), 290-293.

42. Murtaza, G., & Ahmad, I. (2011). First principle study of the structural and optoelectronic properties of cubic perovskites $CsPbM_3$ (M= Cl, Br, I). *Physica B: Condensed Matter*, *406*(17), 3222-3229.

43. Kang, B., Feng, Q., & Biswas, K. (2018). Comparative study of perovskite-type scintillator materials $CsCaI_3$ and $KCaI_3$ via first-principles calculations. *Journal of Physics D: Applied Physics*, *51*(6), 065303.

44. Mullay, J. (1987). Estimation of atomic and group electronegativities. In *Electronegativity* (pp. 1-25). Springer, Berlin, Heidelberg.

45. Taber, K. S., & Coll, R. K. (2002). Bonding. In *Chemical education: Towards research-based practice* (pp. 213-234). Springer, Dordrecht.

46. Wang, F., Grinberg, I., & Rappe, A. M. (2014). Band gap engineering strategy via polarization rotation in perovskite ferroelectrics. *Applied Physics Letters*, *104*(15), 152903.

47. Chen, Q. Y., Huang, Y., Huang, P. R., Ma, T., Cao, C., & He, Y. (2015). Electronegativity explanation on the efficiency-enhancing mechanism of the hybrid inorganic–organic perovskite ABX_3 from first-principles study. *Chinese Physics B*, *25*(2), 027104

48. Castelli, I. E., García-Lastra, J. M., Thygesen, K. S., & Jacobsen, K. W. (2014). Bandgap calculations and trends of organometal halide perovskites. *APL Materials*, *2*(8), 081514.

49. Busipalli, D. L., Nachimuthu, S., & Jiang, J. C. (2019). Theoretical study on halide and mixed halide Perovskite solar cells: Effects of halide atoms on the stability and electronic properties. *Journal of the Chinese Chemical Society*.

50. Noh, J. H., Im, S. H., Heo, J. H., Mandal, T. N., & Seok, S. I. (2013). Chemical management for colorful, efficient, and stable inorganic–organic hybrid nanostructured solar cells. *Nano letters*, *13*(4), 1764-1769.

51. Hwang, B., Gu, C., Lee, D., & Lee, J. S. (2017). Effect of halide-mixing on the switching behaviors of organic-inorganic hybrid perovskite memory. *Scientific reports*, *7*, 43794.

52. Ryu, S., Noh, J. H., Jeon, N. J., Kim, Y. C., Yang, W. S., Seo, J., & Seok, S. I. (2014). Voltage output of efficient perovskite solar cells with high open-circuit voltage and fill factor. *Energy & Environmental Science*, *7*(8), 2614-2618.

53. Pazoki, M., & Edvinsson, T. (2018). Metal replacement in perovskite solar cell materials: chemical bonding effects and optoelectronic properties. *Sustainable Energy & Fuels*, *2*(7), 1430-1445.

54. Colella, S., Mosconi, E., Fedeli, P., Listorti, A., Gazza, F., Orlandi, F., ... & Gigli, G. (2013). $MAPbI_{3-x}Cl_x$ mixed halide perovskite for hybrid solar cells: the role of chloride as dopant on the transport and structural properties. *Chemistry of Materials*, *25*(22), 4613-4618.

55. Kulkarni, S. A., Baikie, T., Boix, P. P., Yantara, N., Mathews, N., & Mhaisalkar, S. (2014). Band-gap tuning of lead halide perovskites using a sequential deposition process. *Journal of Materials Chemistry A*, *2*(24), 9221-9225.

56. Edri, E., Kirmayer, S., Kulbak, M., Hodes, G., & Cahen, D. (2014). Chloride inclusion and hole transport material doping to improve methyl ammonium lead bromide perovskite-based high open-circuit voltage solar cells. *The journal of physical chemistry letters*, *5*(3), 429-433.

57. Slimi, B., Mollar, M., Assaker, I. B., Kriaa, I., Chtourou, R., & Marí, B. (2016). Perovskite FA1-xMAxPbI3 for solar cells: films formation and properties. *Energy Procedia*, *102*, 87-95.

58. Xu, F., Zhang, T., Li, G., & Zhao, Y. (2017). Mixed cation hybrid lead halide perovskites with enhanced performance and stability. *Journal of Materials Chemistry A*, *5*(23), 11450-11461.

59. Correa-Baena, J. P., Abate, A., Saliba, M., Tress, W., Jacobsson, T. J., Grätzel, M., & Hagfeldt, A. (2017). The rapid evolution of highly efficient perovskite solar cells. *Energy & Environmental Science*, *10*(3), 710-727.

60. Ong, K. P., Goh, T. W., Xu, Q. & Huan, A. Structural Evolution in Methylammonium Lead Iodide CH 3 NH 3 PbI 3. J. Phys. Chem. A 119, 11033−11038 (2015).

61. Luo, P., Xia, W., Zhou, S., Sun, L., Cheng, J., Xu, C., & Lu, Y. (2016). Solvent engineering for ambient-air-processed, phase-stable $CsPbI_3$ in perovskite solar cells. *The journal of physical chemistry letters*, *7*(18), 3603-3608.

62. Stoumpos, C. C., Malliakas, C. D., & Kanatzidis, M. G. (2013). Semiconducting tin and lead iodide perovskites with organic cations: phase transitions, high mobilities,

and near-infrared photoluminescent properties. *Inorganic chemistry*, *52*(15), 9019-9038.

63. C. Quarti, E. Mosconi, J. M. Ball, V. D'Innocenzo, C. Tao, S. Pathak, H. J. Snaith, A. Petrozza, F. De Angelis, Energy Environ. Sci. 2016, 9, 155
64. T. Baikie, Y. Fang, J. M. Kadro, M. Schreyer, F. Wei, S. G. Mhaisalkar, M. Grätzel, T. J. White, J. Mater. Chem. A 2013, 1, 5628.
65. W. Geng, L. Zhang, Y.-N. Zhang, W.-M. Lau, L.-M. Liu, J. Phys. Chem. C 2014, 118, 19565.
66. Xiao, Z., Meng, W., Wang, J., Mitzi, D. B., & Yan, Y. (2017). Searching for promising new perovskite-based photovoltaic absorbers: the importance of electronic dimensionality. *Materials Horizons*, *4*(2), 206-216.
67. Adinolfi, V., Yuan, M., Comin, R., Thibau, E. S., Shi, D., Saidaminov, M. I., ... & Bakr, O. M. (2016). The In-Gap Electronic State Spectrum of Methylammonium Lead Iodide Single-Crystal Perovskites. *Advanced Materials, 28*(17), 3406-3410.
68. Chen, Y., Yi, H. T., Wu, X., Haroldson, R., Gartstein, Y. N., Rodionov, Y. I., ... & Podzorov, V. (2016). Extended carrier lifetimes and diffusion in hybrid perovskites revealed by Hall effect and photoconductivity measurements. *Nature Communications*, *7*, 12253.
69. de Quilettes, D. W., Vorpahl, S. M., Stranks, S. D., Nagaoka, H., Eperon, G. E., Ziffer, M. E., ... & Ginger, D. S. (2015). Impact of microstructure on local carrier lifetime in perovskite solar cells. *Science*, *348*(6235), 683-686.

70. Ran, C., Xu, J., Gao, W., Huang, C., & Dou, S. (2018). Defects in metal triiodide perovskite materials towards high-performance solar cells: origin, impact, characterization, and engineering. *Chemical Society Reviews*, *47*(12), 4581-4610.

71. Walsh, A., Scanlon, D. O., Chen, S., Gong, X. G., & Wei, S. H. (2015). Self-regulation mechanism for charged point defects in hybrid halide perovskites. *Angewandte Chemie International Edition*, *54*(6), 1791-1794.

72. Ball, J. M., & Petrozza, A. (2016). Defects in perovskite-halides and their effects in solar cells. *Nature Energy*, *1*(11), 16149.

73. Yin, W. J., Shi, T., & Yan, Y. (2014). Unusual defect physics in $CH_3NH_3PbI_3$ perovskite solar cell absorber. *Applied Physics Letters*, *104*(6), 063903.

74. Du, M. H. (2014). Efficient carrier transport in halide perovskites: theoretical perspectives. *Journal of Materials Chemistry A*, *2*(24), 9091-9098.

75. Yang, J. H., Yin, W. J., Park, J. S., & Wei, S. H. (2015). Self-regulation of charged defect compensation and formation energy pinning in semiconductors. *Scientific reports*, *5*, 16977.

76. Malinkiewicz, O., Yella, A., Lee, Y. H., Espallargas, G. M., Graetzel, M., Nazeeruddin, M. K., & Bolink, H. J. (2014). Perovskite solar cells employing organic charge-transport layers. *Nature Photonics*, *8*(2), 128.

77. Lee, M. M., Teuscher, J., Miyasaka, T., Murakami, T. N., & Snaith, H. J. (2012). Efficient hybrid solar cells based on meso-superstructured organometal halide perovskites. *Science*, *338*(6107), 643-647.

78. Wojciechowski, K., Saliba, M., Leijtens, T., Abate, A., & Snaith, H. J. (2014). Sub-150 C processed meso-superstructured perovskite solar cells with enhanced efficiency. *Energy & Environmental Science*, *7*(3), 1142-1147.

79. Schulz, P., Edri, E., Kirmayer, S., Hodes, G., Cahen, D., & Kahn, A. (2014). Interface energetics in organo-metal halide perovskite-based photovoltaic cells. *Energy & Environmental Science*, *7*(4), 1377-1381.

80. Shi, J., Dong, J., Lv, S., Xu, Y., Zhu, L., Xiao, J., ... & Meng, Q. (2014). Hole-conductor-free perovskite organic lead iodide heterojunction thin-film solar cells: High efficiency and junction property. *Applied Physics Letters*, *104*(6), 063901.

81. Roldán-Carmona, C., Malinkiewicz, O., Soriano, A., Espallargas, G. M., Garcia, A., Reinecke, P., ... & Bolink, H. J. (2014). Flexible high efficiency perovskite solar cells. *Energy & Environmental Science*, *7*(3), 994-997.

82. Fassl, P., Zakharko, Y., Falk, L. M., Goetz, K. P., Paulus, F., Taylor, A. D., ... & Vaynzof, Y. (2019). Effect of density of surface defects on photoluminescence properties in $MAPbI_3$ perovskite films. *Journal of Materials Chemistry C*.

83. Koocher, N. Z., Saldana-Greco, D., Wang, F., Liu, S., & Rappe, A. M. (2015). Polarization dependence of water adsorption to $CH_3NH_3PbI_3$ (001) surfaces. *The journal of physical chemistry letters*, *6*(21), 4371-4378.

84. Noguera, C. (2000). Polar oxide surfaces. *Journal of Physics: Condensed Matter*, *12*(31), R367.

85. Goniakowski, J., Finocchi, F., & Noguera, C. (2007). Polarity of oxide surfaces and nanostructures. *Reports on Progress in Physics*, *71*(1), 016501.

86. Ma, C. G., Krasnenko, V., & Brik, M. G. (2018). First-principles calculations of different (001) surface terminations of three cubic perovskites $CsCaBr_3$, $CsGeBr_3$, and $CsSnBr_3$. *Journal of Physics and Chemistry of Solids, 115*, 289-299.

87. Huang, Y., Wang, L., Ma, Z., & Wang, F. (2018). Pressure effects on band structure evolution of halide perovskites: a first-principles atomic and electronic structure study. *arXiv preprint arXiv:1811.06248*.

88. Haruyama, J., Sodeyama, K., Han, L., & Tateyama, Y. (2014). Termination dependence of tetragonal $CH_3NH_3PbI_3$ surfaces for perovskite solar cells. *The journal of physical chemistry letters*, *5*(16), 2903-2909.

89. Kohn, Walter. "Nobel Lecture: Electronic structure of matter—wave functions and density functionals." *Reviews of Modern Physics* 71.5 (1999): 1253.

90. Hohenberg, P., & Kohn, W. (1964). Density Functional Theory (DFT). *Phys. Rev*, *136*, B864.

91. Feit, M., J. Fleck, and A. Steiger, Solution of the Schrodinger equation by a spectral method. Journal of Computational Physics, 1982. 47(3): p. 412-433.

92. Shirley, J.H., Solution of the Schrodinger equation with a Hamiltonian periodic in time. Physical Review, 1965. 138(4B): p. B979.

93. Dahl, J.P. and J. Avery, Local density approximations in quantum chemistry and solid state physics. 1986, Plenum Press, New York, NY.

94. Perdew, J.P., Density-functional approximation for the correlation energy of the inhomogeneous electron gas. Physical Review B, 1986. 33(12): p. 8822.

95. A. Garc'ia, C. Elsässer, J. Zhu, S. G. Louie, and M. L. Cohen. Use of gradient-corrected functionals in total-energy calculations for solids. Phys. Rev. B, 46:9829– 9832, 1992.

96. B. G. Johnson, P. M. W. Gill, and J. A. Pople. The performance of a family of density functional methods. J. Chem. Phys., 98(7):5612–5626, 1993.

97. G. Kresse and J. Hafner. Ab initio molecular-dynamics simulation of the liquid-metal-amorphous-semiconductor transition in germanium. Phys. Rev. B, 49:14251– 14269, 1994.

98. G. Kresse and J. Hafner. Ab initio molecular dynamics for liquid metals. Phys. Rev. B, 47:558–561, 1993.

99. G. Kresse and J. Furthmüller. Efficiency of Ab initio total energy calculations for metals and semiconductors using a plane-wave basis set. Comput. Mater. Sci., 6:15 – 50, 1996.

100. John P. Perdew, Kieron Burke, and Matthias Ernzerhof. Generalized gradient approximation made simple. Phys. Rev. Lett., 77:3865–3868, 1996.

101. J. P. Perdew, K. Burke, and M. Ernzerhof. Generalized gradient approximation made simple. Phys. Rev. Lett., 78:1396–1396, 1997.

102. Payne, M.C., et al., Iterative minimization techniques for ab initio total-energy calculations: molecular dynamics and conjugate gradients. Reviews of Modern Physics, 1992. 64(4): p. 1045.

103. Momma, K., & Izumi, F. (2011). VESTA 3 for three-dimensional visualization of crystal, volumetric and morphology data. *Journal of applied crystallography*, *44*(6), 1272-1276.

104. Momma, K., & Izumi, F. (2008). VESTA: a three-dimensional visualization system for electronic and structural analysis. *Journal of Applied Crystallography*, *41*(3), 653-658.

105. Izumi, F., & Momma, K. (2007). Three-dimensional visualization in powder diffraction. In *Solid State Phenomena* (Vol. 130, pp. 15-20). Trans Tech Publications.

106. Chadi, D. J., & Cohen, M. L. (1973). Special points in the Brillouin zone. *Physical Review B*, *8*(12), 5747.

107. Methfessel, M. P. A. T., & Paxton, A. T. (1989). High-precision sampling for Brillouin-zone integration in metals. *Physical Review B*, *40*(6), 3616.

108. Blöchl, P. E., Jepsen, O., & Andersen, O. K. (1994). Improved tetrahedron method for Brillouin-zone integrations. *Physical Review B*, *49*(23), 16223.

109. Maintz, S., Deringer, V. L., Tchougréeff, A. L., & Dronskowski, R. (2016). LOBSTER: A tool to extract chemical bonding from plane-wave based DFT. *Journal of computational chemistry*, *37*(11), 1030-1035.

110. Klimeš, J., Bowler, D. R., & Michaelides, A. (2009). Chemical accuracy for the van der Waals density functional. *Journal of Physics: Condensed Matter*, *22*(2), 022201.

111. Paul, J. T., & Limmer, K. R. (2017). *Generating Atomistic Slab Surfaces with Adsorbates* (No. ARL-TR-8247). US Army Research Laboratory Aberdeen Proving Ground United States.

112. Espinosa, N., Serrano-Luján, L., Urbina, A., & Krebs, F. C. (2015). Solution and vapour deposited lead perovskite solar cells: Ecotoxicity from a life cycle assessment perspective. *Solar energy materials and solar cells*, *137*, 303-310.

113. Hailegnaw, B., Kirmayer, S., Edri, E., Hodes, G., & Cahen, D. (2015). Rain on methylammonium lead iodide based perovskites: possible environmental effects of perovskite solar cells. *The journal of physical chemistry letters*, *6*(9), 1543-1547.
114. Wang, K., Liang, Z., Wang, X., & Cui, X. (2015). Lead replacement in $CH_3NH_3PbI_3$ perovskites. *Advanced Electronic Materials*, *1*(10), 1500089.
115. Filip, M. R., & Giustino, F. (2015). Computational screening of homovalent lead substitution in organic–inorganic halide perovskites. *The Journal of Physical Chemistry C*, *120*(1), 166-173.
116. Tyagi, M., Zhuravleva, M., & Melcher, C. L. (2013). Theoretical and experimental characterization of promising new scintillators: Eu^{2+} doped $CsCaCl_3$ and $CsCaI_3$. *Journal of Applied Physics*, *113*(20), 203504.
117. Cherginets, V. L., Rebrova, N. V., Grippa, A. Y., Datsko, Y. N., Ponomarenko, T. V., Pedash, V. Y., ... & Lopin, A. V. (2014). Scintillation properties of $CsSrX_3$: Eu^{2+} ($CsSr_{1-y}Eu_yX_3$, Xá= áCl, Br; 0á≤ áyá≤ á0. 05) single crystals grown by the Bridgman method. *Materials Chemistry and Physics*, *143*(3), 1296-1299.
118. Suta, M., & Wickleder, C. (2017). Spin Crossover of Yb^{2+} in $CsCaX_3$ and $CsSrX_3$ (X= Cl, Br, I)–A Guideline to Novel Halide-Based Scintillators. *Advanced Functional Materials*, *27*(2), 1602783.
119. Loyd, M. S. (2017). The Development of Cesium Calcium Bromo-Iodide scintillator for X-ray and Gamma ray detection.
120. Jellicoe, T. C., Richter, J. M., Glass, H. F., Tabachnyk, M., Brady, R., Dutton, S. E., ... & Böhm, M. L. (2016). Synthesis and optical properties of lead-free cesium tin halide

perovskite nanocrystals. *Journal of the American Chemical Society*, *138*(9), 2941-2944.

121. Nie, W., Blancon, J. C., Neukirch, A. J., Appavoo, K., Tsai, H., Chhowalla, M., ... & Tretiak, S. (2016). Light-activated photocurrent degradation and self-healing in perovskite solar cells. *Nature communications*, *7*, 11574.

122. Snaith, H. J., Abate, A., Ball, J. M., Eperon, G. E., Leijtens, T., Noel, N. K., ... & Zhang, W. (2014). Anomalous hysteresis in perovskite solar cells. *J. Phys. Chem. Lett*, *5*(9), 1511-1515.

123. Huang, Y., Yin, W. J., & He, Y. (2018). Intrinsic point defects in inorganic cesium lead iodide perovskite $CsPbI_3$. *The Journal of Physical Chemistry C*, *122*(2), 1345-1350.

124. Huang, H., Bodnarchuk, M. I., Kershaw, S. V., Kovalenko, M. V., & Rogach, A. L. (2017). Lead halide perovskite nanocrystals in the research spotlight: stability and defect tolerance. *ACS energy letters*, *2*(9), 2071-2083.

125. Kang, J., & Wang, L. W. (2017). High defect tolerance in lead halide perovskite $CsPbBr_3$. *The journal of physical chemistry letters*, *8*(2), 489-493.

126. Xu, P., Chen, S., Xiang, H. J., Gong, X. G., & Wei, S. H. (2014). Influence of defects and synthesis conditions on the photovoltaic performance of perovskite semiconductor $CsSnI_3$. *Chemistry of Materials*, *26*(20), 6068-6072.

127. Shi, T., Zhang, H. S., Meng, W., Teng, Q., Liu, M., Yang, X., ... & Zhao, Y. J. (2017). Effects of organic cations on the defect physics of tin halide perovskites. *Journal of Materials Chemistry A*, *5*(29), 15124-15129

128. Ming, W., Shi, H., & Du, M. H. (2016). Large dielectric constant, high acceptor density, and deep electron traps in perovskite solar cell material $CsGeI_3$. *Journal of Materials Chemistry A*, *4*(36), 13852-13858.

129. Du, M. H. (2014). Efficient carrier transport in halide perovskites: theoretical perspectives. *Journal of Materials Chemistry A*, *2*(24), 9091-9098.

130. Ming, W., Chen, S., & Du, M. H. (2016). Chemical instability leads to unusual chemical-potential-independent defect formation and diffusion in perovskite solar cell material CH_3NH_3 PbI_3. *Journal of Materials Chemistry A*, *4*(43), 16975-16981.

131. Taufique, M. F. N., Khanal, R., Choudhury, S., & Banerjee, S. (2018). Impact of iodine antisite (I_{Pb}) defects on the electronic properties of the (110) $CH_3NH_3PbI_3$ surface. *The Journal of chemical physics*, *149*(16), 164704.

132. (2006) Influence of the Crystal Structure Defects on Scintillation Properties. In: Inorganic Scintillators for Detector Systems. Particle Acceleration and Detection. Springer, Berlin, Heidelberg.

133. Slifkin, M. A. (1963). Molecular Orbital Theory and Experimentally Determined Energy-levels. *Nature*, *200*(4909), 877.

134. L.E. Sutton, ed. (1965). "Supplement 1956–1959, Special publication No. 18". Table of interatomic distances and configuration in molecules and ions. London, UK: Chemical Society.

135. W.W. Porterfield (1984). Inorganic chemistry, a unified approach. Reading Massachusetts, USA: Addison Wesley Publishing Co. ISBN 0-201-05660-7.

136. Luo, Y. R. (2002). *Handbook of bond dissociation energies in organic compounds*. CRC press.

137. Wan, K., & Li, A. Materials Used.

138. Jain, A., Ong, S. P., Hautier, G., Chen, W., Richards, W. D., Dacek, S., ... & Persson, K. A. (2013). Commentary: The Materials Project: A materials genome approach to accelerating materials innovation. *Apl Materials*, *1*(1), 011002.

139. Schilling, G., & Meyer, G. (1996). Ternäre Bromide und Iodide zweiwertiger Lanthanide und ihre Erdalkali-Analoga vom Typ AMX_3 und AM_2X_5. *Zeitschrift für anorganische und allgemeine Chemie*, *622*(5), 759-765.

140. Tang, W., Sanville, E., & Henkelman, G. (2009). A grid-based Bader analysis algorithm without lattice bias. *Journal of Physics: Condensed Matter*, *21*(8), 084204.

141. Ye, Y., Run, X., Hai-Tao, X., Feng, H., Fei, X., & Lin-Jun, W. (2015). Nature of the band gap of halide perovskites ABX_3 (A= CH_3NH_3, Cs; B= Sn, Pb; X= Cl, Br, I): First-principles calculations. *Chinese Physics B*, *24*(11), 116302.

142. Rodnyi, P. A., Munro, I. H., Macdonald, M. A., Mel'chakov, E. N., Kotel'nikov, S. S., & Voloshinovsky, A. S. (1994). Impurity core-valence transitions in $Rb_{1-x}Cs_xCaCl_3$ crystals. *Nuclear Instruments and Methods in Physics Research Section B: Beam Interactions with Materials and Atoms*, *88*(4), 407-410.

143. Beurer, E., Grimm, J., Gerner, P., & Güdel, H. U. (2006). New type of near-infrared to visible photon upconversion in Tm^{2+}-doped $CsCaI_3$. *Journal of the American Chemical Society*, *128*(10), 3110-3111.

144. Yang, K., Zhuravleva, M., & Melcher, C. L. (2011). Crystal growth and characterization of $CsSr_{1-x}Eu_xI_3$ high light yield scintillators. *physica status solidi (RRL)–Rapid Research Letters*, *5*(1), 43-45.

145. Suta, M., Urland, W., Daul, C., & Wickleder, C. (2016). Photoluminescence properties of Yb^{2+} ions doped in the perovskites $CsCaX_3$ and $CsSrX_3$ (X= Cl, Br, and I)–a comparative study. *Physical Chemistry Chemical Physics, 18*(19), 13196-13208.

146. Grimm, J., Suyver, J. F., Beurer, E., Carver, G., & Güdel, H. U. (2006). Light-emission and excited-state dynamics in Tm^{2+} doped $CsCaCl_3$, $CsCaBr_3$, and $CsCaI_3$. *The Journal of Physical Chemistry B*, *110*(5), 2093-2101.

147. Kittel, C., McEuen, P., & McEuen, P. (1976). *Introduction to solid state physics* (Vol. 8, pp. 323-324). New York: Wiley.

148. Shannon, R. D. (1976). Revised effective ionic radii and systematic studies of interatomic distances in halides and chalcogenides. *Acta crystallographica section A: crystal physics, diffraction, theoretical and general crystallography*, *32*(5), 751-767.

149. Travis, W., Glover, E. N. K., Bronstein, H., Scanlon, D. O., & Palgrave, R. G. (2016). On the application of the tolerance factor to inorganic and hybrid halide perovskites: a revised system. *Chemical science*, *7*(7), 4548-4556.

150. Geng, W., Tong, C. J., Tang, Z. K., Yam, C., Zhang, Y. N., Lau, W. M., & Liu, L. M. (2015). Effect of surface composition on electronic properties of methylammonium lead iodide perovskite. *Journal of Materiomics*, *1*(3), 213-220.

Appendix A

A1: Computed lattice parameters of ABX_3 (A=Cs, M= Ca, Sr, Ba and X=F, Cl, Br, I)

Table A1: The optimized lattice parameter (Å) of cubic ABX_3 (A=Cs, M= Ca, Sr, Ba and X=F, Cl, Br, I)

Systems	a	b	c
$CsCaF_3$	4.58	4.58	4.58
$CsCaCl_3$	5.46	5.46	5.46
$CsCaBr_3$	5.77	5.77	5.77
$CsCaI_3$	6.21	6.21	6.21
$CsSrF_3$	4.82	4.82	4.82
$CsSrCl_3$	5.74	5.74	5.74
$CsSrBr_3$	6.05	6.05	6.05
$CsSrI_3$	6.47	6.47	6.47
$CsBaF_3$	5.15	5.15	5.15
$CsBaCl_3$	6.07	6.07	6.07
$CsBaBr_3$	6.34	6.34	6.34
$CsBaI_3$	6.82	6.82	6.82

Table A2: The optimized lattice parameter (Å) of orthorohmbic ABX_3 (A=Cs, M= Ca, Sr, Ba and X=F, Cl, Br, I)

Systems	a	b	c
$CsCaF_3$	3.67	12.50	8.68
$CsCaCl_3$	4.26	14.59	10.51
$CsCaBr_3$	4.50	15.14	11.14
$CsCaI_3$	4.85	16.07	12.01
$CsSrF_3$	3.84	12.79	9.09
$CsSrCl_3$	4.44	14.84	10.90
$CsSrBr_3$	4.66	15.39	11.52
$CsSrI_3$	5.01	16.29	12.39
$CsBaF_3$	4.05	13.28	9.49
$CsBaCl_3$	4.64	15.28	11.26
$CsBaBr_3$	4.85	15.88	11.87
$CsBaI_3$	5.18	16.53	12.84

A2: Electronic band structures of ABX_3 with and without antisite defect

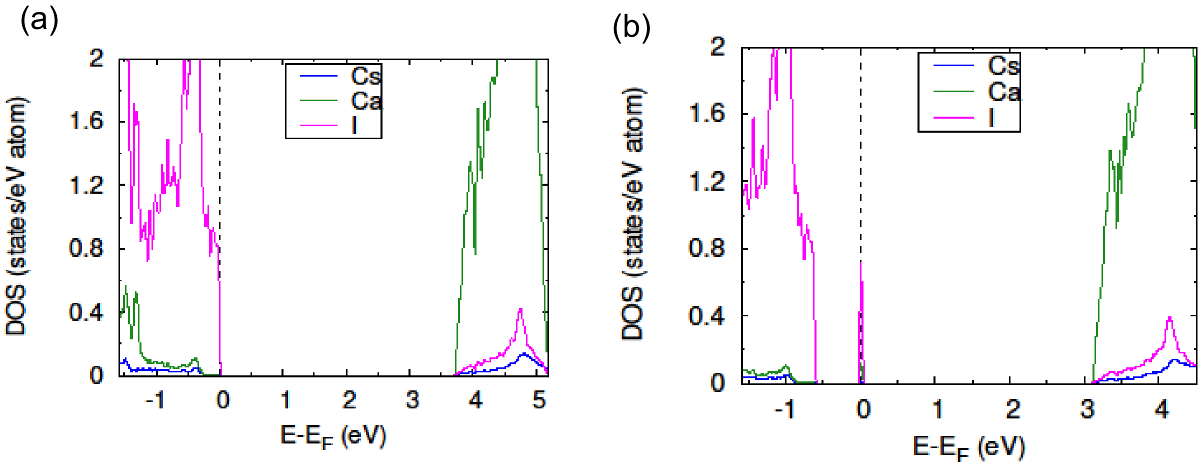

Figure A1. The partial DOS of bulk cubic $CsCaI_3$ (a) without defect and (b) with antisite defect.

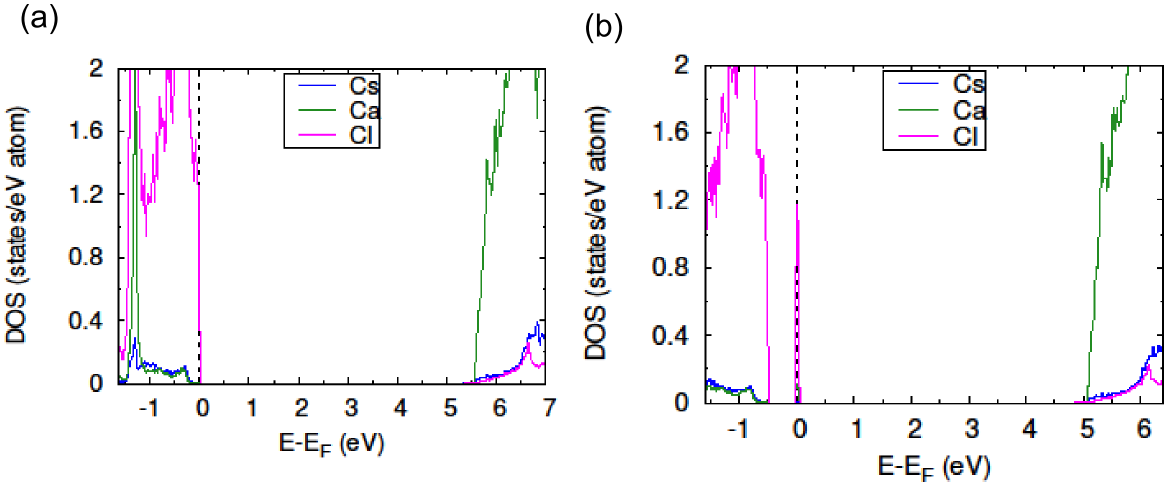

Figure A2. The partial DOS of bulk cubic $CsCaCl_3$ (a) without defect and (b) with antisite defect.

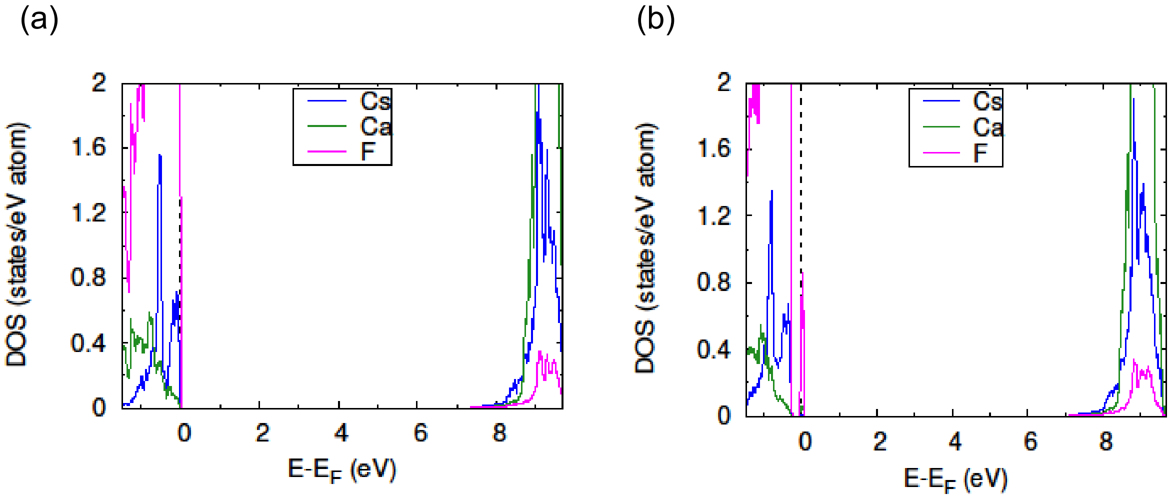

Figure A3. The partial DOS of bulk cubic $CsCaF_3$ (a) without defect and (b) with antisite defect.

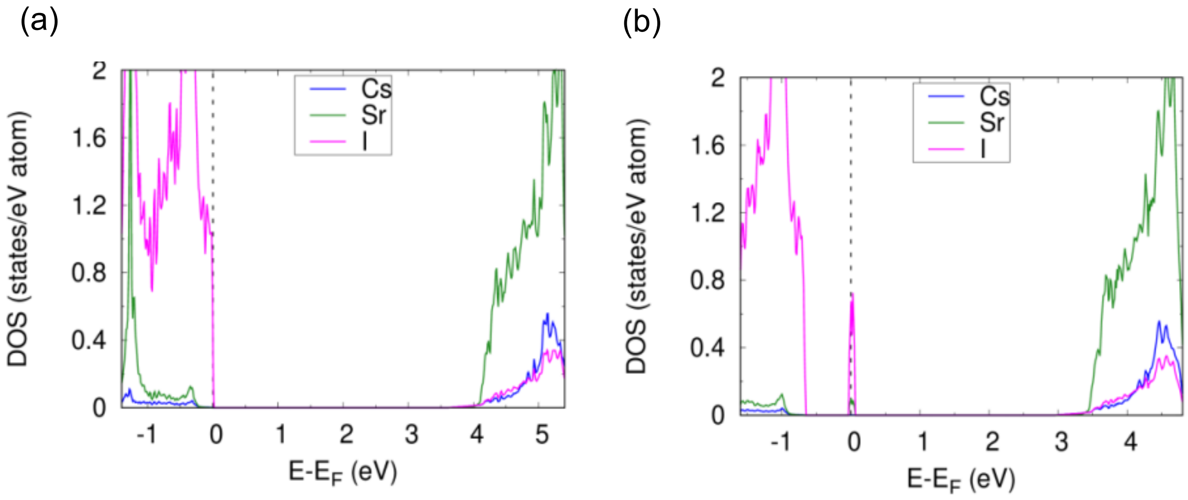

Figure A4. The partial DOS of bulk cubic $CsSrI_3$ (a) without defect and (b) with antisite defect.

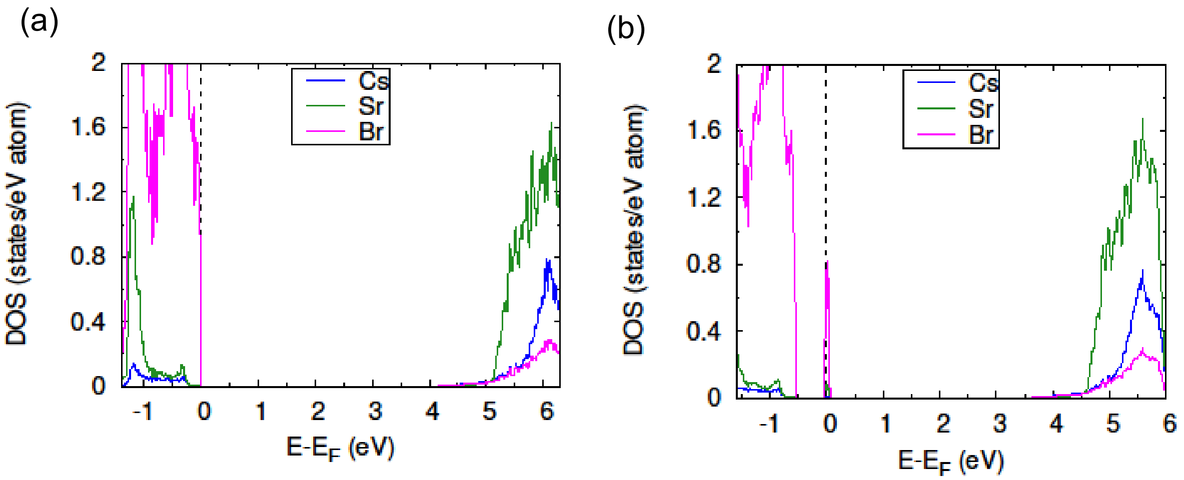

Figure A5. The partial DOS of bulk cubic $CsSrBr_3$ (a) without defect and (b) with antisite defect.

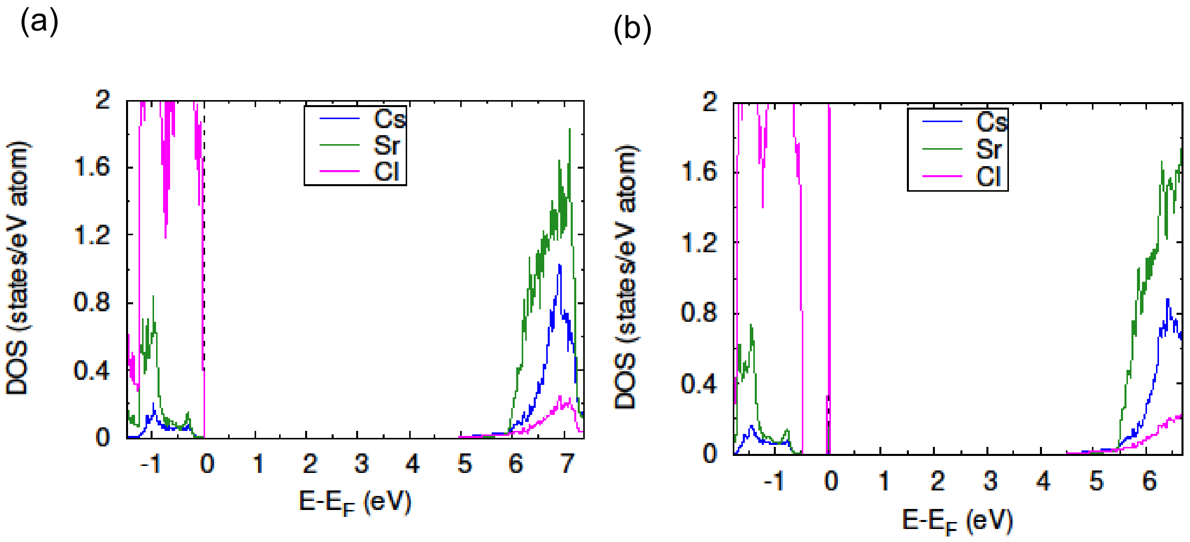

Figure A6. The partial DOS of bulk cubic $CsSrCl_3$ (a) without defect and (b) with antisite defect

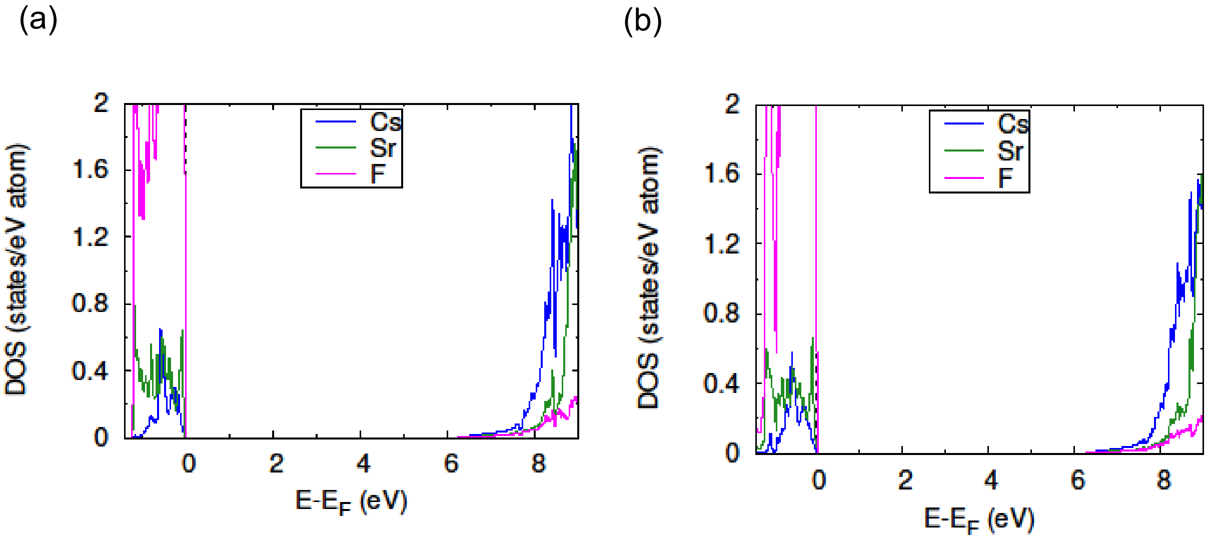

Figure A7. The partial DOS of bulk cubic CsSrF$_3$ (a) without defect and (b) with antisite defect.

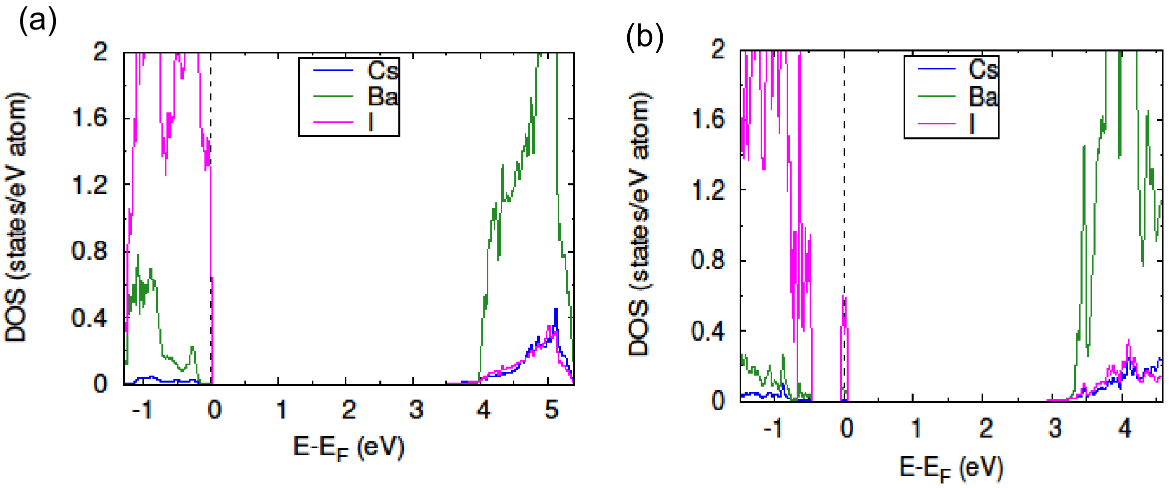

Figure A8. The partial DOS of bulk cubic CsBaI$_3$ (a) without defect and (b) with antisite defect.

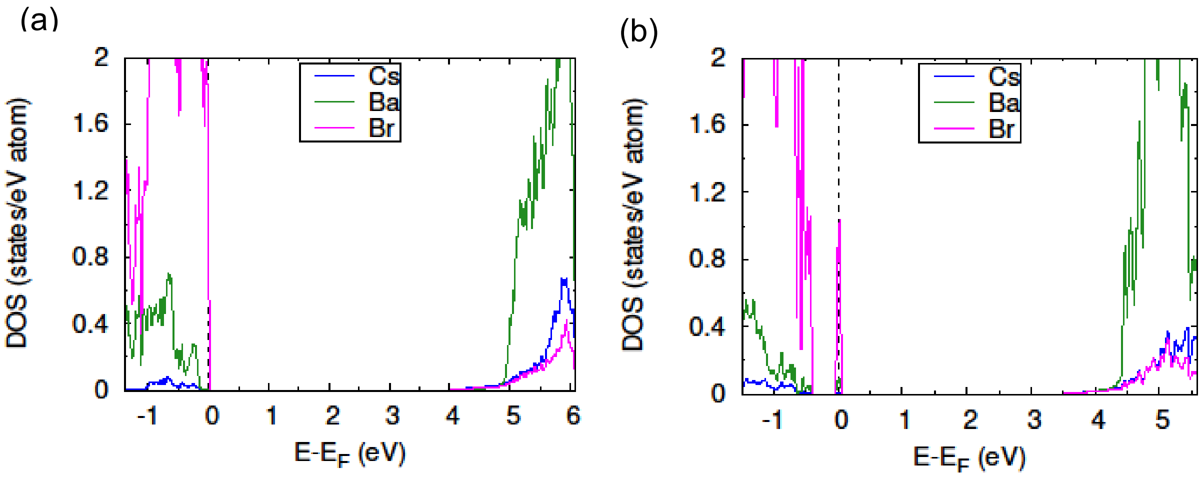

Figure A9. The partial DOS of bulk cubic $CsBaBr_3$ (a) without defect and (b) with antisite defect.

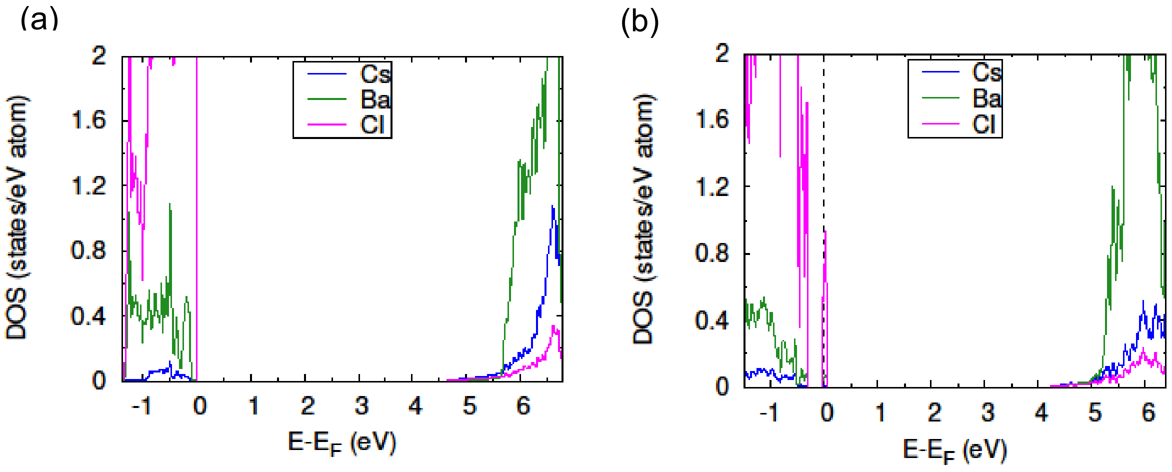

Figure A10. The partial DOS of bulk cubic $CsBaCl_3$ (a) without defect and (b) with antisite defect.

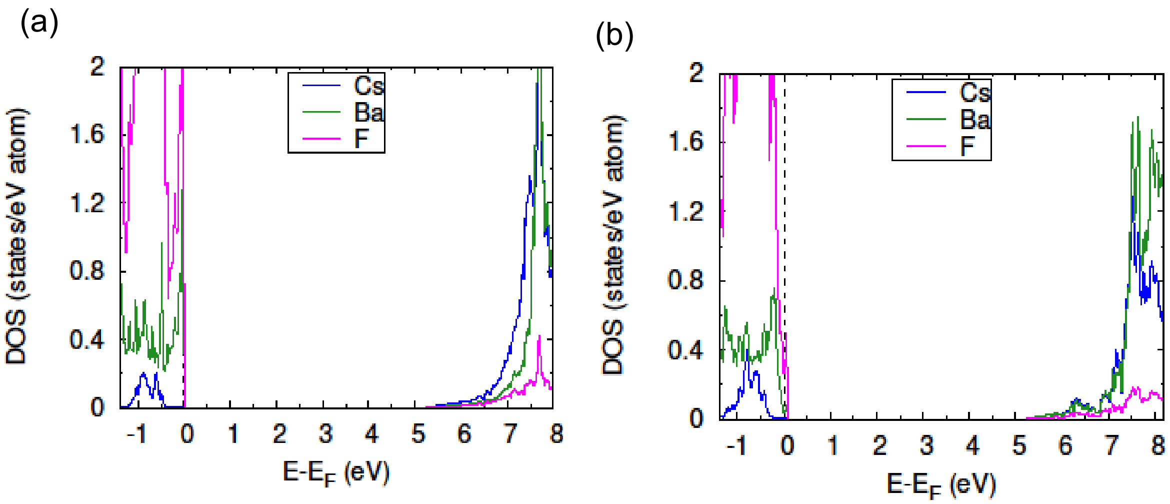

Figure A11. The partial DOS of bulk cubic $CsBaF_3$ (a) without defect and (b) with antisite defect.

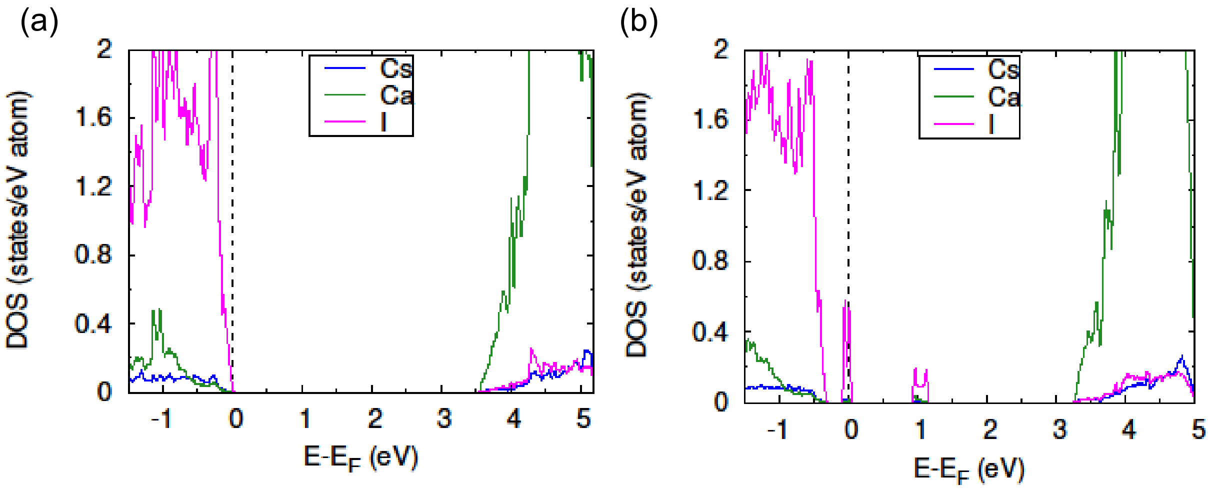

Figure A12. The partial DOS of bulk orthorohmbic $CsCaI_3$ (a) without defect and (b) with antisite defect.

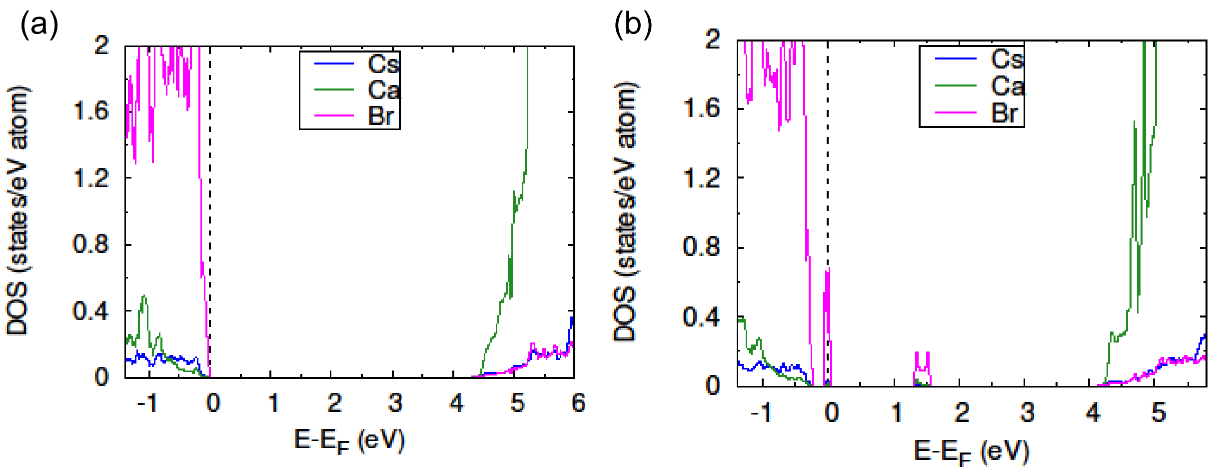

Figure A13. The partial DOS of bulk orthorohmbic $CsCaBr_3$ (a) without defect and (b) with antisite defect.

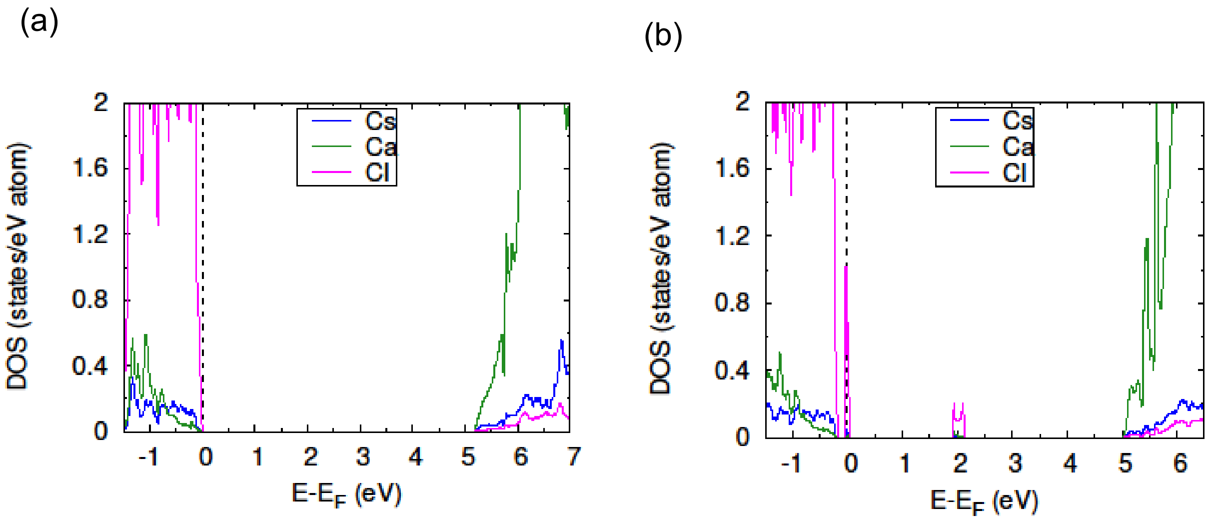

Figure A14. The partial DOS of bulk orthorohmbic $CsCaCl_3$ (a) without defect and (b) with antisite defect.

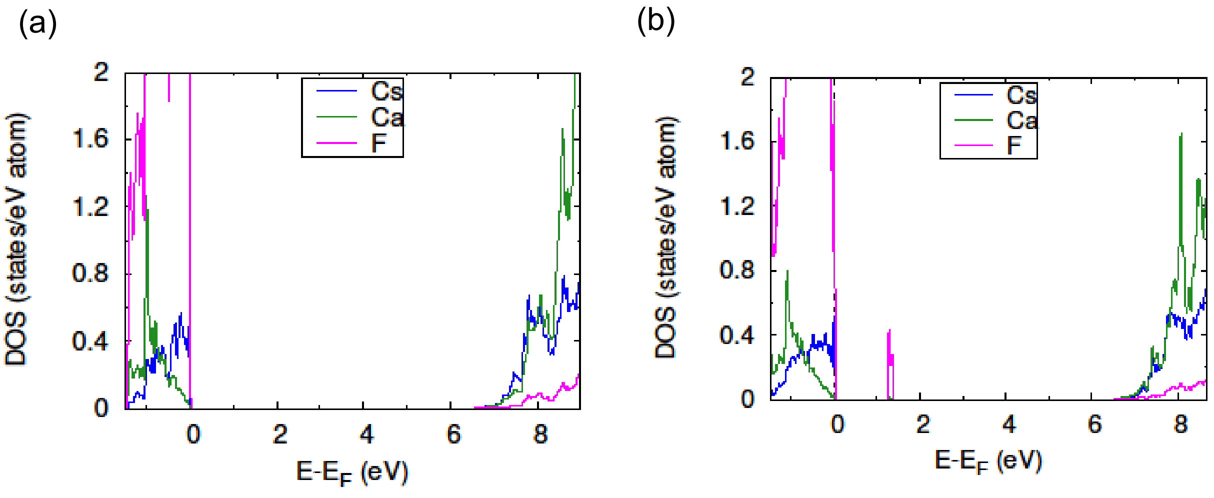

Figure 15. The partial DOS of bulk orthorohmbic $CsCaF_3$ (a) without defect and (b) with antisite defect.

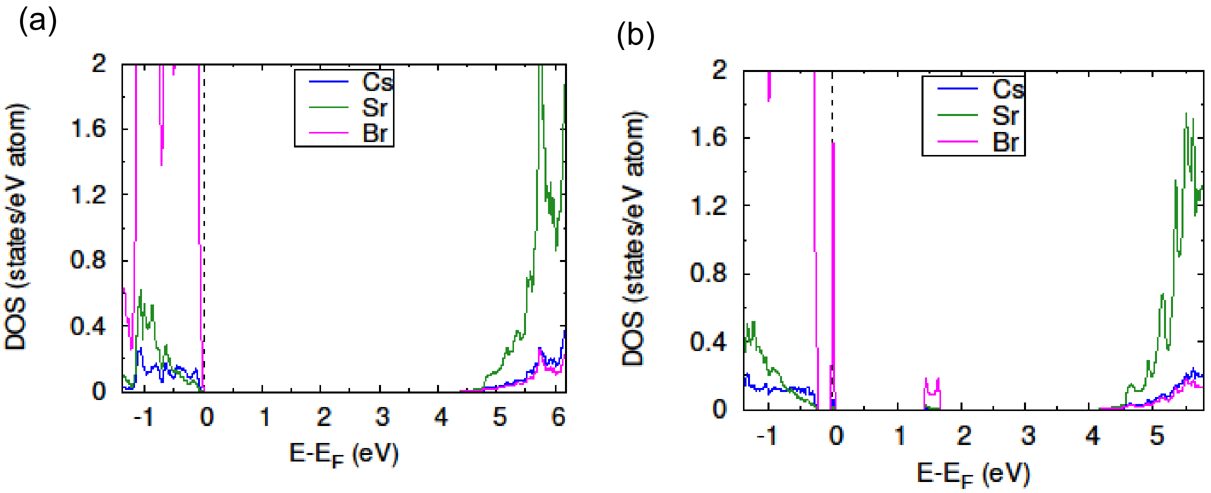

Figure A16. The partial DOS of bulk orthorohmbic $CsSrBr_3$ (a) without defect and (b) with antisite defect.

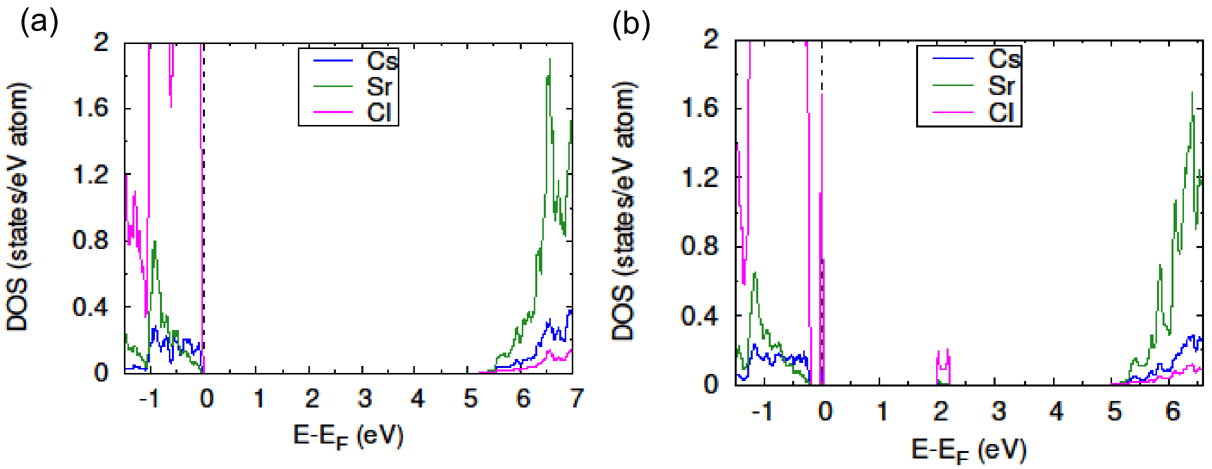

Figure A17. The partial DOS of bulk orthorohmbic $CsSrCl_3$ (a) without defect and (b) with antisite defect.

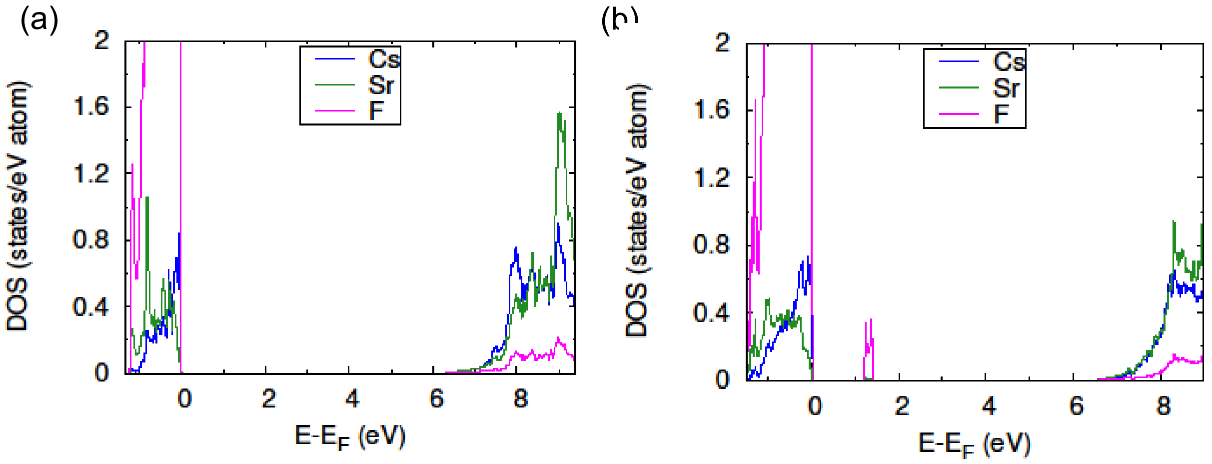

Figure 18. The partial DOS of bulk orthorohmbic $CsSrF_3$ (a) without defect and (b) with antisite defect.

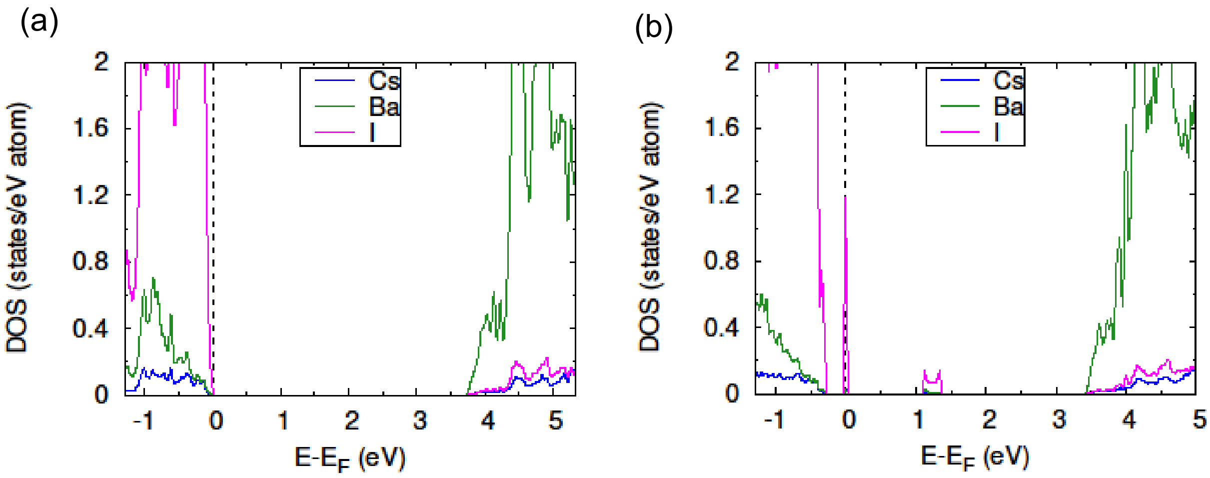

Figure 19. The partial DOS of bulk orthorohmbic CsBaI$_3$ (a) without defect and (b) with antisite defect.

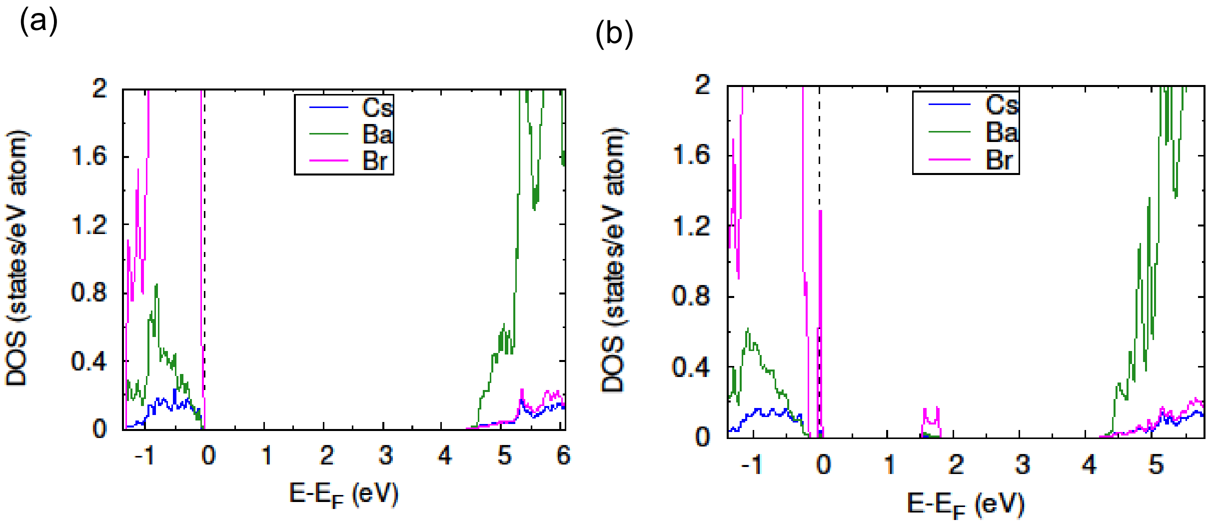

Figure A20. The partial DOS of bulk orthorohmbic CsBaBr$_3$ (a) without defect and (b) with antisite defect.

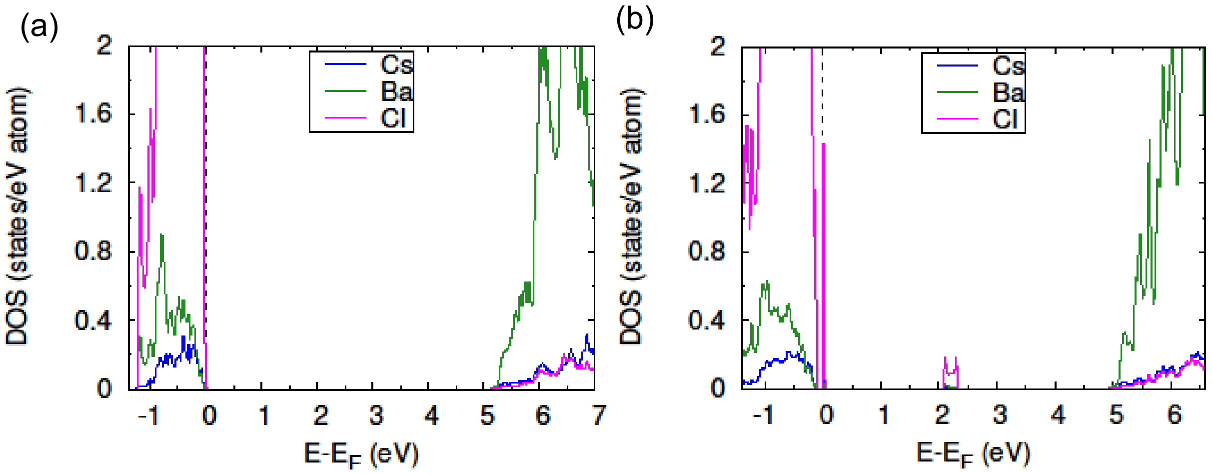

Figure A21. The partial DOS of bulk orthorohmbic $CsBaCl_3$ (a) without defect and (b) with antisite defect.

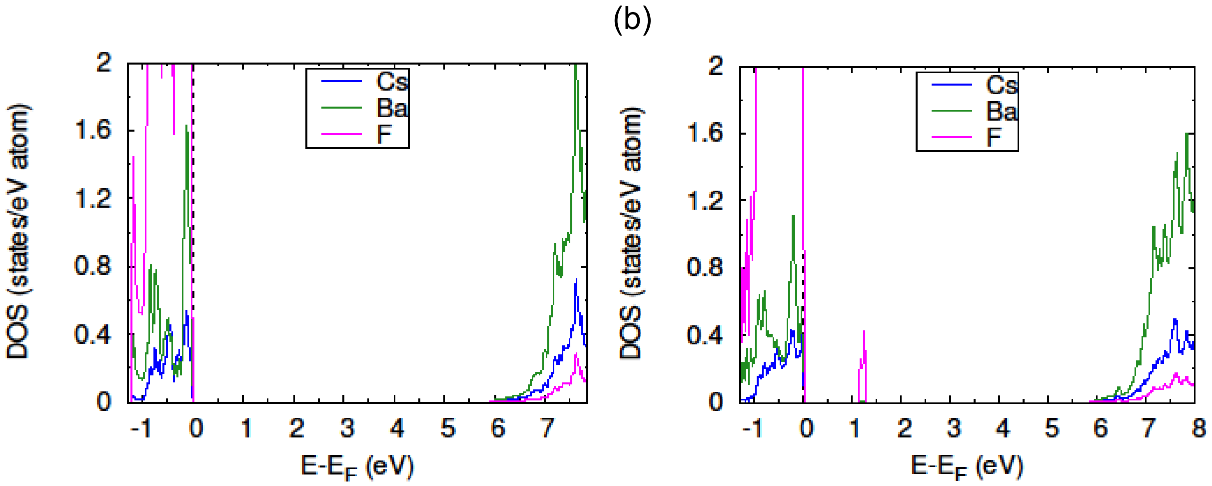

Figure A22. The partial DOS of bulk orthorohmbic $CsBaF_3$ (a) without defect and (b) with antisite defect.

A3. Cubic (*Pm3m*) and Orthorohmbic (*Pnma*) ABX_3 representation.

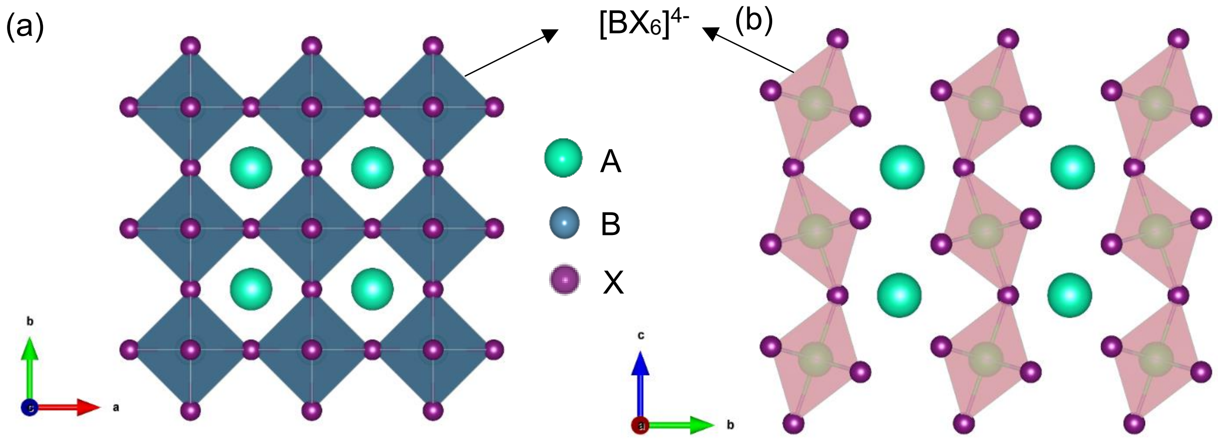

Figure A23. Representation of (a) Cubic (*Pm3m*) and (b) Orthorohmbic (*Pnma*) ABX_3.

A4. Table representation bond-length change for cubic $CsCaX_3$ (X= F, Cl, Br and I) systems.

Table A3. Change in the Bond-length of Ca-X (X= F, Cl, Br, I) before and after introducing the X_{Ca} antisite defect.

Systems	Ca-X bond-length in pure structure (Å)	X_{Ca} – X bond-length after introducing the defect (Å)	Percent change in bond-length (%)
$CsCaI_3$	3.11	3.22	3.5
$CsCaBr_3$	2.88	2.95	2.4
$CsCaCl_3$	2.73	2.78	1.8
$CsCaF_3$	2.24	2.27	1.3

A5. Effect of Cl_{Ca} antisite defect on the electronic structure of cubic $CsCaBr_3$.

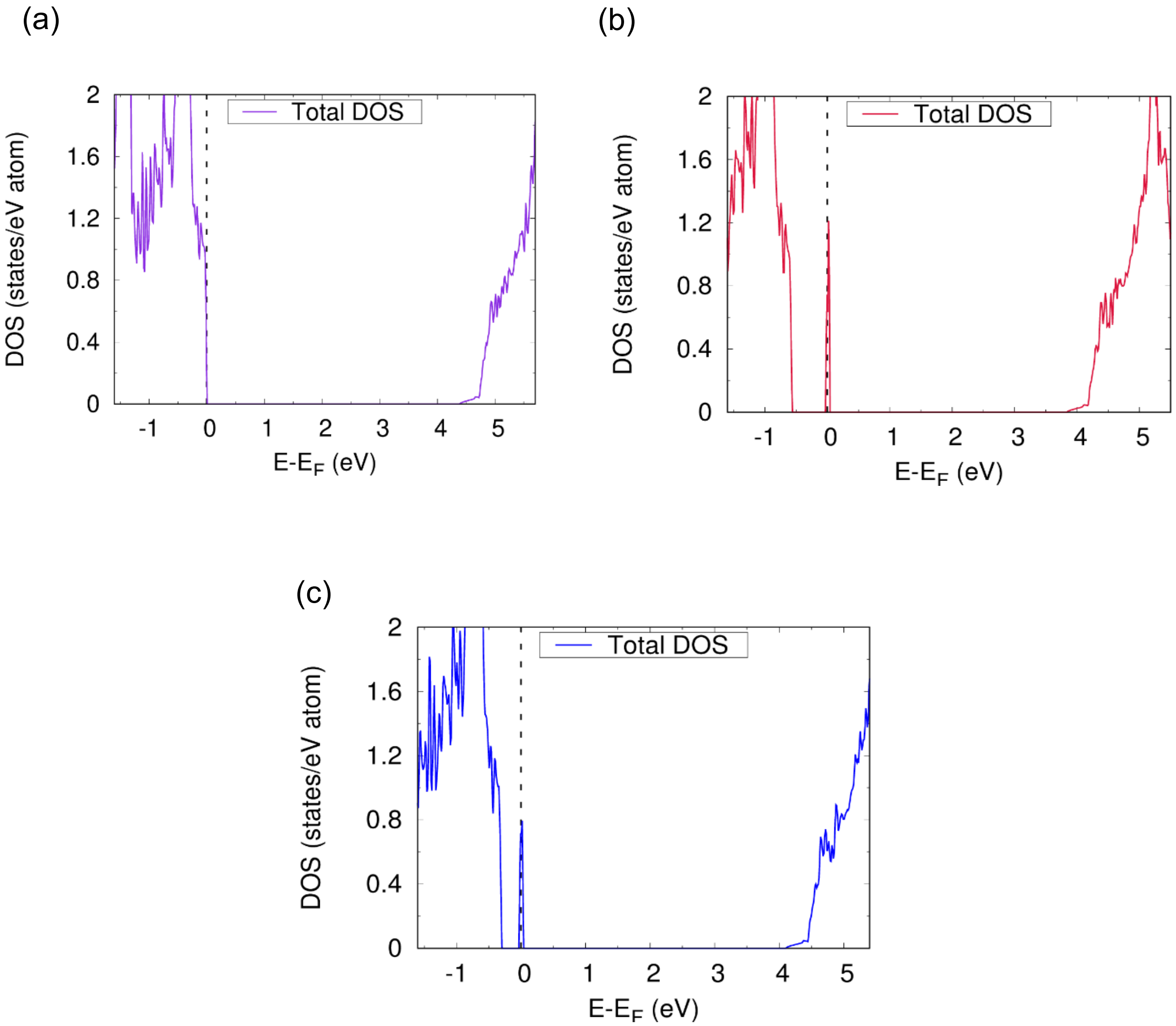

Figure A24. The total DOS of bulk cubic $CsCaBr_3$ (a) without defect, (b) with Br_{Ca} antisite defect and, (c) with Cl_{Ca} antisite defect

A6. LOBSTER COOP plot for cubic $CsCaBr_3$ and orthorhombic $CsSrI_3$ in presence of antisite defect.

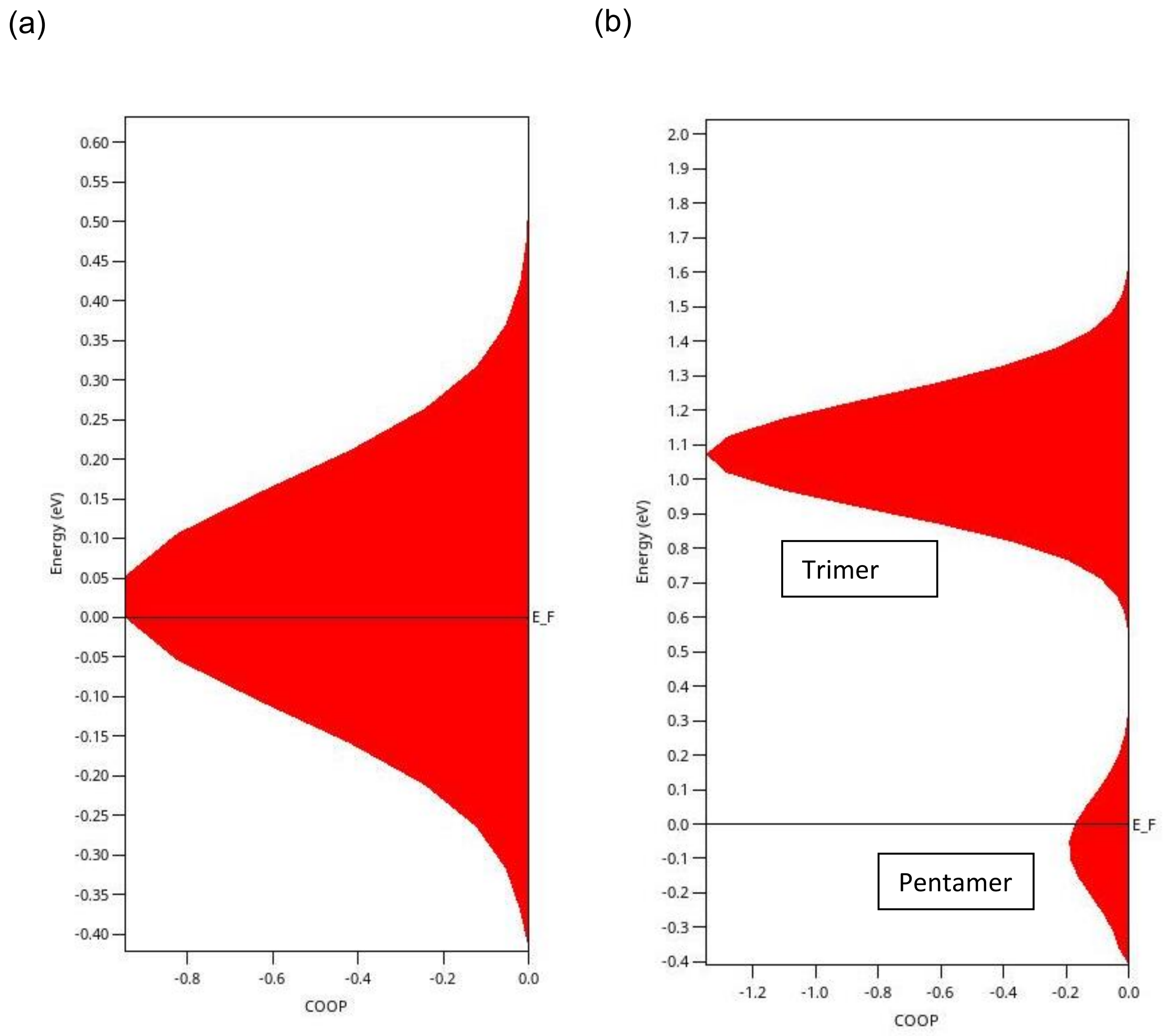

Figure A25. Crystal orbital overlap population (COOP) analysis for (a) Br_{Ca} antisite defect with surrounding Br atoms in cubic $CsCaBr_3$ and (b) I_{Sr} antisite defect with surrounding I atoms in the orthorohmbic $CsSrI_3$.